UTS UNIVERSITY OF TECHNOLOGY SYDNEY

System-level and Multi-disciplinary Design Optimization of a Permanent Magnet Synchronous Motor Drive System

by Lin Liu

Thesis submitted in fulfilment of the requirements for the degree of

Doctor of Philosophy

under the supervision of Prof. Youguang Guo, Prof. Jianguo Zhu, and Dr. Gang Lei

University of Technology Sydney

Faculty of Engineering and Information Technology

October, 2024

Certificate of Original Authorship

I, Lin Liu, declare that this thesis is submitted in fulfilment of the requirements for the award of Doctor of Philosophy, in the School of Electrical and Data Engineering, Faculty of Engineering and Information Technology at the University of Technology Sydney.

This thesis is wholly my own work unless otherwise referenced or acknowledged. In addition, I certify that all information sources and literature used are indicated in the thesis.

This document has not been submitted for qualifications at any other academic institution.

This research is supported by the Australian Government Research Training Program.

Acknowledgement

First and foremost, I would like to express my deepest gratitude to my principal supervisor Prof. Youguang Guo, whose support went beyond academic mentoring. He assisted me in all aspects of my life, enabling me to focus earnestly on my research by resolving numerous challenges I faced. His guidance was a cornerstone of my doctoral journey.

I am profoundly grateful to my co-supervisor Prof. Jianguo Zhu, for his invaluable guidance on my research direction. His insights were truly cutting-edge and instrumental to my progress. I am also deeply thankful to my co-supervisor, Dr. Gang Lei, for his relentless help and teaching in AI and optimization algorithms, which enriched my knowledge significantly.

I extend my sincere thanks to Mr. Brett Lowder and Dr. Mike Zhong from the Electrical Lab of the University of Technology Sydney (UTS), and Prof. Xiaodong Sun from Jiangsu University, China. Their support in experimental guidance, equipment training, and data acquisition was crucial during my Ph.D. studies.

I am also thankful to the China Scholarship Council and the UTS for their financial support, which alleviated my economic concerns during this period.

My heartfelt gratitude goes to my parents and grandparents for their unwavering support and encouragement towards my further studies. I deeply regret not being able to accompany them for four years, but their continued support despite missing me has been a great source of motivation.

Lastly, I owe my deepest thanks to my husband, Dr. Wenliang Yin. His assistance in proofreading my dissertation, providing feedback, and offering every possible support has been invaluable. Under Prof. Jianguo Zhu's support, he had the opportunity to pursue two years of postdoctoral research at The University of Sydney. My husband's presence in Australia during those two years alleviated my loneliness and provided immense comfort. His dedication and love mean the world to me, and I hope we can continue to walk hand in hand, striving for a better life together in the uncertain future.

List of Publications

Refereed international scientific journal articles (*in chronological order*)

[1] L. Liu, Y. Guo, G. Lei, and J. G. Zhu, "Iron loss calculation for high-speed permanent magnet machines considering rotating magnetic field and thermal effects," *IEEE Transactions on Applied Superconductivity*, vol. 25, no. 8, pp. 1-5, Nov. 2021.

[2] L. Liu, Y. Guo, W. Yin, G. Lei, and J. Zhu, "Design and optimization technologies of permanent magnet machines and drive systems based on digital twin model," *Energies*, vol. 15, no. 17, article 6186, Aug. 2022.

[3] L. Liu, X. Ba, Y. Guo, G. Lei, X. Sun, and J. Zhu, "Improved Iron Loss Prediction Models for Interior PMSMs Considering Coupling Effects of Multiphysics Factors," *IEEE Transactions on Transportation Electrification*, vol. 9, no. 1, pp. 416-427, Mar. 2023.

[4] Y. Guo, L. Liu, X. Ba, H. Lu, G. Lei, W. Yin, and J. Zhu, "Designing High-Power-Density Electric Motors for Electric Vehicles with Advanced Magnetic Materials," *World Electric Vehicle Journal*, vol. 14, no. 4, article 114, Apr. 2023. (Corresponding author)

[5] Y. Guo, L. Liu, W. Yin, H. Lu, G. Lei, and J. Zhu, "Developing high-power-density electromagnetic devices with nanocrystalline and amorphous magnetic materials," *Nanomaterials*, vol. 13, no. 13, article 1963, Jun. 2023. (Corresponding author)

[6] L. Liu, Y. Guo, W. Yin, G. Lei, X. Sun, and J. Zhu, "Efficient design optimization of PMSM drive systems using improved equivalent-circuit-based loss minimization control," *IEEE Transactions on Industrial Electronics*, doi: 10.1109/TIE.2024.3447748.

[7] L. Liu, Y. Guo, G. Lei, and J. Zhu, "Efficient iron loss estimation of interior PMSMs in electric vehicles: analytical modelling and experimental validation," *IEEE Transactions on Applied Superconductivity*, vol. 34, no. 8, pp. 1-5, Nov. 2024.

[8] L. Liu, W. Yin, and Y. Guo, "Hybrid mechanism-data-driven iron loss modelling for permanent magnet synchronous motors considering multiphysics coupling effects," *IET Electric Power Applications*, vol. 18, pp. 1833-1843, Dec. 2024.

Refereed international scientific conference papers (*in chronological order*)

[1] L. Liu, Y. Guo, G. Lei, J. Zhu, and J. Jin, "Power loss analysis of high speed permanent magnet machine," *2020 IEEE International Conference on Applied Superconductivity and Electromagnetic Devices (ASEMD)*, Tianjin, China, 16-18 Oct. 2020, pp. 1-2.

[2] L. Liu, Y. Guo, G. Lei, and J. G. Zhu, "Design and analysis technologies of high speed permanent magnet machines," *2021 31st Australasian Universities Power Engineering Conference (AUPEC)*, Perth, Australia, 26-30 Sep. 2021, pp. 1-6.

[3] L. Liu, Y. Guo, G. Lei, and J. Zhu, "Multi-level design optimization of an IPMSM drive system considering an improved loss model," *2022 32nd Australasian Universities Power Engineering Conference (AUPEC)*, Adelaide, Australia, 26-28 Sep. 2022, pp. 1-6.

[4] L. Liu, Y. Guo, G. Lei, W. Yin, X. Ba, and J. Zhu, "Construction method and application prospect of electrical machine digital twin," *2022 25th International Conference on Electrical Machines and Systems (ICEMS)*, Chiang Mai, Thailand, 29 Nov.-02 Dec. 2022, pp. 1-6.

[5] Y. Guo, X. Ba, L. Liu, L. Hou, G. Lei, and J. Zhu, "Performance enhancement of permanent magnet synchronous motors based on improved circuit models," *2022 25th International Conference on Electrical Machines and Systems (ICEMS)*, Chiang Mai, Thailand, 29 Nov.-02 Dec. 2022, pp. 1-6.

[6] L. Liu, Y. Guo, G. Lei, and J. Zhu, "Comparative iron loss analysis of the interior PMSMs for electric vehicles considering the effects of temperature variation," *2023 IEEE International Conference on Applied Superconductivity and Electromagnetic Devices (ASEMD)*, Tianjin, China, 27-29 Oct. 2023, pp. 1-2.

[7] L. Liu, Y. Guo, G. Lei, and J. Zhu, "Review of data-driven artificial intelligence applications in electric machines and drive systems," *2023 IEEE International Future Energy Electronics Conference (IFEEC)*, Sydney, Australia, 20-23 Nov. 2023, pp. 93-97.

List of Acronyms

AC	Alternating Current
AFL	Air Friction Loss
AI	Artificial Intelligence
ARC	Adaptive Robust Controller
CFD	Computational Fluid Dynamic
DACE	Design and Analysis of Computer Experiments
DC	Direct Current
DEA	Differential Evolution Algorithm
DTC	Direct Torque Controller
ECM	Equivalent Circuit Model
ESO	Extended State Observer
EV	Electric Vehicle
FEA	Finite Element Analysis
FEM	Finite Element Model
FOC	Field-Oriented Controller
GA	Genetic Algorithm
IOM	Indirect Optimization Model
IPM	Interior Permanent Magnet
IPMSM	Interior Permanent Magnet Synchronous Motor

LPTN	Lumped Parameter Thermal Network
MEC	Magnetic Equivalent Circuit
MOGA	Multi-Objective Genetic Algorithm
MPC	Model Predictive Controller
MPSO	Multi-Objective Particle Swarm Optimization
MTPA	Maximum Torque Per Ampere
NSGA	Nondominated Sorting Genetic Algorithm
PI	Proportional-Integral
PM	Permanent Magnet
PMSM	Permanent Magnet Synchronous Motor
PWM	Pulse Width Modulation
SCL	Stator Copper Loss
SIL	Stator Iron Loss
SLC	Sensor-Less Controller
SMC	Soft Magnetic Composite
SPM	Surface-mounted Permanent Magnet
SPWM	Sinusoidal Pulse Width Modulation
V-F	Voltage–Frequency

List of Tables

List of Figures

Abstract

Aiming at the integrated demands of electric equipment and oriented towards enhancing the high performance and high efficiency of electric drive systems, this study seeks to accomplish an overall design optimization strategy for electric motors and their drive systems. Furthermore, it will deeply investigate key issues such as precise modelling of iron losses, system-level minimum loss controls, and holistic optimization methods.

Permanent magnet synchronous motor (PMSM) drive systems have experienced increased applications in many aspects such as centrifugal compressors, machine tools, flywheels, distributed power generation systems, as well as road, rail, marine and aerospace transportation. Considering the multidisciplinary coupling and varying operational conditions faced by the PMSM and its drive system in electric vehicles (EVs), the main research focuses include:

(1) Considering the effects of multiphysics factors on iron loss prediction accuracy for PMSMs, this thesis aims to propose an advanced analytical iron loss prediction model for interior PMSMs (IPMSMs), in which both the spatial harmonic from slotting and the carrier harmonics from the pulse width modulation (PWM) inverter, as well as the thermal and mechanical factors are all considered; (2) A system-level total loss model considering various loads and speeds is proposed, and based on this model, a minimum loss control strategy is derived; (3) Combining this loss controller, a multi-objective optimization system-level model is proposed to primarily enhance the efficiency and static/dynamic performance of the entire drive system; (4) Due to the time-consuming nature of directly applying multi-objective algorithms for the solution, a novel multi-level optimization algorithm combined with surrogate models is applied to decouple nonlinear and high-dimensional issues; and (5) Using simulation models and the prototype test platform, the proposed approaches and methodologies are all validated.

The study can provide new theories and methods for the design and optimization of both electric motors and their drive systems, driving the development and innovation of related technologies, promoting industrial upgrading, and advancing technological progress.

Contents

Chapter 1

Introduction

1.1 Background and Significance

Reducing the dependence on fossil fuels and improving energy utilisation efficiency are the two core measures to implement a clean, low carbon, high reliability and efficient energy power system [1]-[2]. Targeting these two requirements, industrial and transport electrification is receiving widespread attention. Meanwhile, electric drive systems have experienced increased applications in many aspects such as centrifugal compressors, machine tools, flywheels, distributed power generation systems, as well as road, rail, marine and aerospace transportation [3]-[5]. Compared with conventional fossil-fuel-based drive systems, electric drive systems possess irreplaceable advantages. Specifically, although the efficiency of electricity generation is quite low, electrical machines, as the core energy production part in electric drive systems, have high energy conversion efficiency, e.g., more than 90% [5]-[7]. Meanwhile, the power source is electricity, which may promote the development of integration of renewable energy into the power grid, and therefore it is also beneficial to emission reduction [8]. The additional transmission systems can be avoided on some occasions, by which the corresponding noises and costs can be reduced and the control system response speed can also be improved. Moreover, electric drive systems may have more robust stability to the external environment and are more convenient to be applied in equipment for space and ocean investigations [3], [5], [9]. More importantly, nearly half of annual electricity is used in applications powered by electric drive systems. If designers can improve the drive system's efficiency by even a few percent, the environmental protection and energy savings will be considerable. Therefore, it is of great significance to solve some problems existing in the electric drive system in line with future development needs.

Generally, an electric drive system mainly comprises a power source, a frequency converter/inverter with control devices and an electric motor, as shown in Figure 1-1. Among them, the motor, as the main energy-consuming component, is directly related to the drive system's efficiency, reliability, and safe operation. Recently, the topology of the

permanent magnet synchronous motor (PMSM) has been considered suitable for electric drive systems under complex operating conditions, thanks to its advantages in the aspects of weight and space-saving, efficiency improvement, speed range expansion as well as control performance promotion [3]-[4], [10]. PMSM drive systems, regarded as crucial components in many modern appliances and industrial equipment and systems, play a vital role in global energy conservation, environmental protection, and sustainable development. Traditional optimization focuses on the component level, such as optimizing motor design or control algorithm parameters. However, in the context of integrated renewable energy devices, modern appliances or systems require that drive systems be specifically designed and optimized to provide comprehensive support for their system-level optimal functionality through multiple performance metrics.

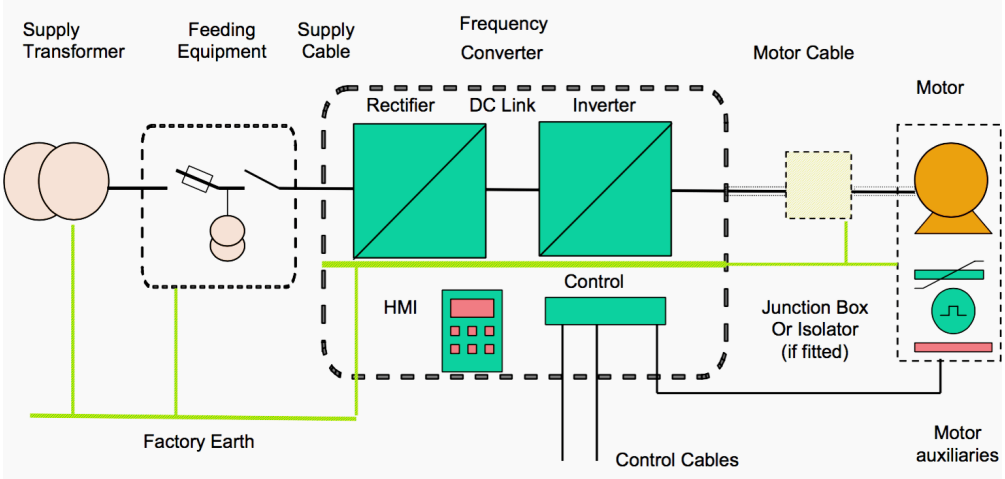

Figure 1-1 Example of a component-level motor drive system.

Although the importance of system-level design optimization for electric drive systems is well recognized, there is a scarcity of research on this topic in the literatures [11]-[12]. Traditional design and optimization methods are mostly conducted at the component level for different types of motors. Through extensive research and practice, it has been realized that in designing electric drive systems, the goal should be to achieve optimal system performance rather than optimal performance of individual components such as the motor. This is because assembling separately optimized components into a system does not necessarily ensure the best system performance. Optimal system performance can only be achieved through a holistic approach that simultaneously optimizes all components at the system level. On the other hand, the design optimization of a PMSM drive system is a highly coupled multidisciplinary process, as it involves various fields such as

electromagnetics, mechanics, thermal management, control, and materials science [10]. The interactions and interdependencies among these fields necessitate a comprehensive consideration at the intersection of multiple disciplines for system optimization to achieve the best overall performance and efficiency.

In summary, by incorporating multidisciplinary considerations into the system-level design optimization of PMSM drive systems, significant improvements in efficiency and performance can be achieved. Furthermore, this integrated optimization approach can yield substantial environmental, economic, and social benefits. It not only helps businesses reduce operational costs and enhance competitiveness but also contributes positively to global sustainable development efforts.

1.2 Objectives

To enhance the efficiency and driving performance of PMSM drive systems while reducing size, weight, and cost to meet the challenging demands of electric vehicles (EVs), recent efforts have focused extensively on designing and optimizing high-performance drive systems for next-generation vehicles [13]. This study primarily focuses on effective multidisciplinary design approaches and advanced system-level optimization methods for high-efficiency and high-performance PMSM drive systems. The multidisciplinary analysis includes materials, electromagnetics, thermal management, mechanics, and controllers. The outcomes of this study will benefit researchers and engineers involved in the design and optimization of electric motors and drive systems, helping them address challenging applications such as green energy systems and EVs. The main objectives are given as follows:

(1) To review popular design optimization methods for motors and drive systems, including design analysis models and methods, such as electromagnetic design and controller models, as well as optimization models and algorithms, including single-objective models, multi-objective models, and intelligent algorithms.
(2) To establish total power loss models directly related to efficiency. Considering the complex magnetic characteristics of the core material in PMSMs, a precise multidisciplinary model for iron losses should be developed by integrating

electromagnetics, materials science, thermodynamics, and computer simulation technologies.

(3) To derive a system-level minimum loss control approach, integrating it with motor components to form a comprehensive motor drive system model that combines motor design with control parameters.

(4) To develop a multi-objective optimization model for the entire system, and explore effective and efficient multi-objective optimization algorithms that maintain accuracy while saving time. This approach aims to obtain an optimal solution set that enhances the performance of the entire system.

1.3 Organization of Thesis

The following chapters are organized as follows:

Chapter 2 provides an overview of the fundamentals of motor and drive system design. It explores design analysis models from various disciplines and also reviews different optimization algorithms. Subsequently, this chapter discusses the challenges and offers recommendations based on advancements in state-of-the-art technologies.

Chapter 3 proposes an advanced analytical iron loss prediction model for interior PMSMs (IPMSMs) used in EVs, considering the effects of multiphysics factors, in which both the spatial harmonic from slotting and the carrier harmonics from pulse width modulation (PWM) inverter, as well as the thermal and mechanical factors are all evaluated. Compared with the existing various iron loss models, the calculation accuracy can be improved while the computation time can be reduced.

Chapter 4 derives a system-level loss model and uses it to develop a minimum loss controller based on the relationship between *d-q* axis currents and electromagnetic torque. Experimental and comparative simulation results show the superior performance of this controller in terms of loss control.

Chapter 5 introduces the basic steps of system-level optimization strategy, establishes a multi-objective optimization model encompassing both the motor side and the control side based on application requirements, and finally proposes an effective multi-level

optimization strategy. Significant improvements in system efficiency and static/dynamic performance are achieved with the optimized design approaches through case studies.

Chapter 6 concludes the entire thesis work, highlights its significance, and paves the way for future research endeavors in the field of electric drive systems optimization and design.

Chapter 2

Literature Survey on the Design Optimization of PMSMs and Drive Systems

2.1 Introduction

Compared to induction motors and switched reluctance motors, PMSMs have several advantages [14]-[15]: (a) *High Efficiency*: PMSMs achieve higher efficiency because their excitation comes from permanent magnets, eliminating excitation current losses. This is particularly noticeable under partial load conditions; (b) *High Power Density*: Due to the high magnetic energy product of permanent magnets, PMSMs can deliver higher power with relatively smaller size and weight; (c) *High Power Factor*: PMSMs typically exhibit a high power factor since there is no excitation current, and the current is primarily used to provide active power; (d) *Good Dynamic Performance*: PMSMs have fast dynamic response and a wide speed range, making them suitable for applications requiring rapid dynamic response; (e) *High Control Precision*: PMSMs maintain strict synchronization between their rotational speed and the power supply frequency, resulting in high precision in speed and position control. PMSMs and their drive systems are widely used in various fields of modern society, including industrial automation (such as computer numerical control machines and industrial robots), EVs (such as drive motors and electric power steering), household appliances (such as air conditioners and washing machines), renewable energy (such as wind and solar power generation), aerospace (such as electric aircraft and drones), medical equipment (such as magnetic resonance imaging-machines and electric wheelchairs), and marine propulsion.

By designing and optimizing dedicated PMSM drive systems tailored to different application scenarios and stakeholders' requirements, these motors can be maximally leveraged to enhance overall performance. This approach meets the modern societal demands for efficient, precise, and reliable motor drive systems.

The design optimization of PMSMs and their drive systems is a multidisciplinary, multi-objective, high-dimensional, highly nonlinear, and strongly coupled problem, posing challenges for both academia and industry. This thesis work encompasses two main parts: design analysis and performance optimization.

2.2 Design Analysis

This section provides a brief overview of the fundamentals of design, including analysis models and methods used for motors and drive systems, particularly focusing on PMSMs based on our design experience. Due to the multidisciplinary nature, these design models and methods will be explored at the disciplinary level, including materials, electromagnetics, thermal, mechanical, and control algorithm design. The design analysis is directly related to optimization objectives and constraints, typically encompassing electromagnetic performance such as efficiency, cogging torque, torque ripple, power factor, and voltage, as well as other general considerations regarding cost, mass, and volume, which ensures that the motor can operate stably under various operating conditions and meet the design requirements.

2.2.1 Topology and Material

The stator of PMSMs plays a significant role in cooling the whole machine. In addition, most of the losses including the core losses generated by the PMSM rotor are all directly related to the structure and material of the stator [16]-[17].

It is worth mentioning that there is a type of PMSMs that operates at high or ultra high speeds. In consideration of the machine's maximum speed and inverter capability, at present, the number of poles is usually fixed at 2 or 4 to realize high-speed operation [18]. The 2-pole motors have strong integrity of magnetic poles, which can effectively reduce the winding current frequency as well as the magnetic field alternating frequency. The 4-pole machines have a small winding length which can effectively save space and cut down the copper loss. However, due to the increase in motor main frequency, iron loss increases. Meanwhile, a higher number of poles can also be selected when the motor works with high power and low speed [19]. Three schemes, namely, multi-slot, less-slot and non-slot types, can be employed for the structural design of the stator core. Among

these options, the non-slot-based motors have low eddy-current loss behavior, but have large air gap length. The related air gap flux density is reduced [20]. The less-slot-based machines have better performance in terms of air gap flux density and permanent magnetic material utilisation. However, the increased tooth harmonics and eddy-current loss lead to the depreciation of this kind of structure. In this case, PMSMs applied in high speed situations are mostly equipped with multi-slot-based stator cores to achieve balanced and satisfactory overall performance [21].

Novel stator core materials are continuously investigated to effectively improve the machine's electromagnetic performance and reduce iron loss [22]. Non-oriented silicon steel sheets are usually used for PMSMs' stators. Recently, amorphous alloy and soft magnetic composite (SMC) materials have been utilized in PMSMs successfully [23]. Compared to silicon steel sheets, stators based on amorphous alloys can achieve a much lower iron loss. However, the restrictions of batch manufacturing technology for amorphous alloy stamping with complex shapes result in such materials being used only for simple non-slot situations. SMC may be suitable for the PMSMs' stator cores due to the advantages including magnetic isotropy, low eddy-current loss and cost. When the motor working frequency is higher than 2000 Hz, SMC can be better than electrical steels for reducing the core loss. However, once the working frequency is smaller than 1000 Hz, the SMC core loss value may not be as good as the electrical steel [24]. Figure 2-1 illustrates the varying curves of iron loss of different types of PMSMs' stator core materials with respect to the working frequency.

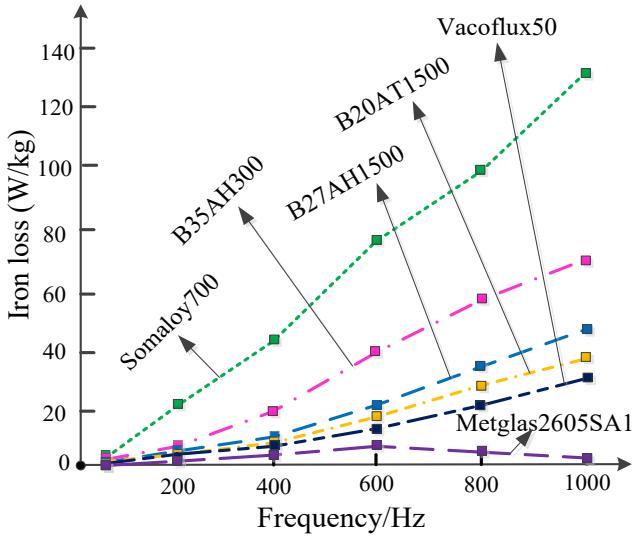

Figure 2-1 Iron loss of different core materials with respect to frequency.

Based on our group's experience, here, we provided a detailed review of the application of SMC materials in PMSM motors. The most attractive advantage of the SMC material may be its environmental friendliness. Material waste in production is minimized, e.g., less than 3%, and the minimal scrapped material can be recycled back into components or raw material. Furthermore, used SMC motors can be easily crushed for separating and reusing high-value materials like copper, offering much better recyclability than lamination steel machines. In addition, this powder metallurgical process has a lower energy consumption than the punching and stacking processes of laminated cores. SMC materials have unique properties, such as insulation coating on each particle resulting in very low eddy current loss, relatively low total core loss at medium and higher frequencies, magnetic and thermal isotropy due to their powdered nature, and the prospect of low-cost mass production by using powder metallurgical techniques. Over the past three decades, the development of SMC materials and their applications in electromagnetic devices have been significant [25]-[35]. Various types of electric motors with SMC cores have been designed, analyzed, and prototyped, and some have been applied in practical drives, such as the permanent magnet motor designed by Jack *et al*. [26] in 1999 for driving an electric bicycle. Axial-field motors [27]-[29], claw pole motors [30]-[32], and transverse flux motors [33]-[35] are other examples of machines that have utilized SMC as the core material, as these machines typically have a three-dimensional magnetic field, making SMC an ideal candidate as a core material. In 2014, Maloberti *et al*. [36] presented the magnetic modelling of an axial field permanent magnet (PM) motor with an SMC core for EVs. In 2015, Kobler *et al*. in [37] developed an axial motor with SMC core and ferrite magnets, showing a promising design of low cost, high power density and no rare-earth PM. In 2021, Du *et al*. [38] presented a claw pole motor with SMC cores. The study on the SMC preparation process showed that the best magnetic and mechanical properties were achieved with a pressing pressure of 700 MPa and an annealing temperature of 500 ℃. In 2022, Chu *et al*. [39] analyzed a PM claw pole motor with SMC core considering the material characteristics over a wide temperature range. Also, in 2022, Li *et al*. [40] studied a flux reversal claw pole SMC motor for cogging torque minimization.

Despite the unique benefits of SMC materials, there are also some drawbacks. For instance, the magnetic permeability of SMC is quite low, and its mechanical strength is not as high as that of conventional silicon steel. While molding techniques have been

expected to make the fabrication of SMC cores easier, there are still challenging issues, such as the core size and shape against manufacturing productivity and cost, as well as the mass density and uniformity of the molded parts.

In addition to stator configuration, the rotor structure and material can also affect the PMSM performance. There are two different kinds of rotor structures including the interior permanent magnet (IPM) and surface-mounted permanent magnet (SPM) for PMSMs. IPM performs well in terms of speed regulation range as well as overload capacity, and has low risk of demagnetization. Figure 2-2 shows three different IPM rotor structures used in high speed PMSMs. The rotor in Figure 2-2 (a), verified to have a small magnetic flux leakage coefficient, was utilized in [41]. A novel tangential rotor structure, illustrated as Figure 2-2 (b) was proposed for not only effectively reducing the stress and magnetic flux leakage, but also providing the magnetic reluctance torque and reducing the permanent magnet usage [42]-[43]. Moreover, a kind of ring permanent magnet segmented structure, shown as Figure 2-2 (c), was also proposed, which can efficiently reduce the sleeve thickness and equivalent air gap, and thus improve the PM utilization [44]. However, the problems of air gap harmonics gradually hinder the extensive applications of IPM.

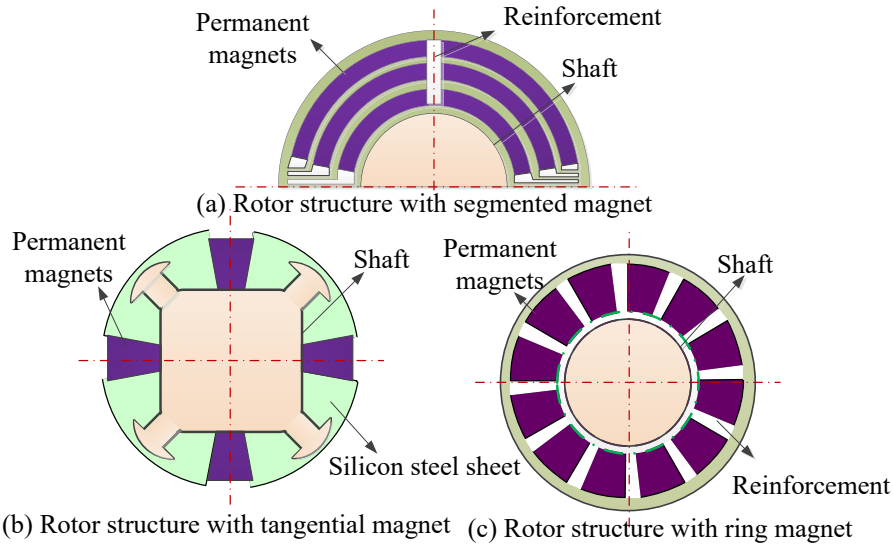

Figure 2-2 Different IPM rotor structures used in PMSMs.

The advantages like small space requirements, convenient machining and desired power density promote the applications of SPM in PMSMs, especially in high speed/power PMSMs [45]. As shown in Figure 2-3 (a), for SPM, the permanent magnet is mounted on

the surface of the rotor and protected by sleeves made of composite materials or alloys in ultra high speed cases. This kind of rotors is usually utilized in motor manufacturing companies like ABB [46] and GE [47]. At the same time, a bread-loaf permanent magnet structure, shown as Figure 2-3 (b), was proposed in [48], by which the motor performance in air gap magnetic flux density can be improved. To relieve rotor eddy-current loss, various design optimization methods were also studied for the SPM machines [49]-[50]. In [49], a kind of Halbach SPM was proposed and utilized in a high speed PMSM with a rated power of 30 kW and rate speed of 20000 r/min. Additionally, the eddy current shields made of aluminum or copper, coupled with the permanent magnet segmentation technology, were introduced in [50].

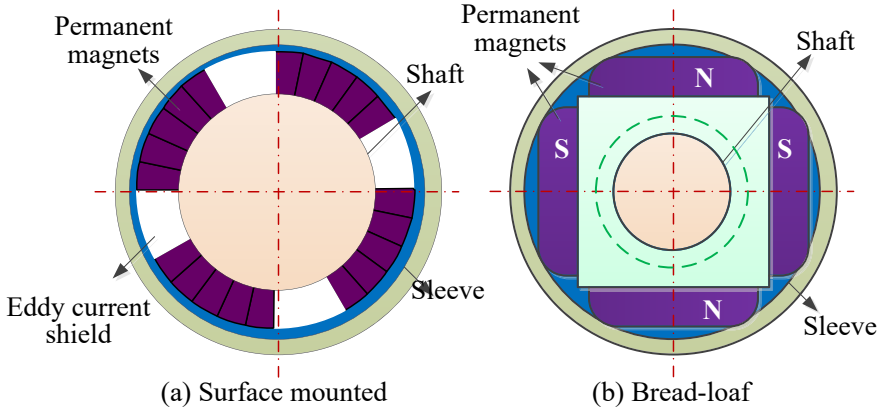

Figure 2-3 Two types of rotor structure used in high speed PMSMs.

There are two suitable materials (NdFeB and SmCo) for the PMSM rotor thanks to their high coercivity, compressive strength and flexural strength. NdFeB has a greater tensile strength than SmCo but it is susceptible to temperature. SmCo has a small temperature coefficient and performs better in high operating temperatures, which means that this material is more suitable for high speed PMSMs considering the requirements of high temperature working stability. However, the PMSM needs to operate at a high speed range, which means that the SPM would suffer from a huge centrifugal force. Thus, sleeve equipment installed on the surface of a permanent magnet, is usually used to protect the rotor. Considering the satisfactory strength characteristics, alloy materials including Inconel718 and Ti6Al4V as well as fibrous composites such as carbon fiber and glass fiber can be used in the sleeve [10]. Among these materials, fibrous composites are preferable in density and strength, but they have a low thermal conductivity. Alloy

materials are proven to have better behavior in terms of heat dissipation, temperature stability and stiffness.

2.2.2 Power Losses

Power losses and efficiency are two major issues in the design and analysis of motors and drive systems. The losses are relatively big in PMSMs and the motor efficiency would be reduced, which can directly affect the temperature rise and distribution inside the motor as well as the machine operating safety and stability. In this case, researchers have carried out a lot of substantive work to improve the calculation accuracy of power losses including stator iron loss, PM eddy current loss, winding copper loss and air friction loss.

Normally, the direct current (DC) resistance is used for calculating stator copper loss (SCL) [51]. However, this method cannot be applied to PMSMs in relatively high speed cases directly since the high temperature rise and frequency stimulate the increase of skin and proximity effects that can reduce the current flow area and therefore enhance SCL. Analytical models like Dowell and Ferreira were verified to be effective for the calculation of winding losses. But the accuracy is not satisfactory due to the structural assumptions and the ignorance of nonlinear factors [52]. As a result, the finite element model (FEM) is developed to not only accurately calculate SCL but also analyze the magnetic field and current density distributions of PMSMs. Researchers also gave suggestions for relieving skin and proximity effects including: a) using the windings with some thin wires in parallel, b) making the wire radius smaller than the skin depth at the highest operation frequency, c) determining the optimal parallel wire numbers for a certain frequency, d) smoothening the current waveform to reduce the harmonics, and e) designing the appropriate slot-openings [51]-[53].

Stator iron loss (SIL) is the power dissipated in a magnetic core due to the variation of the magnetic field. When PMSMs work at the conditions of the high frequency of varying magnetic fields, high temperature rise and internal stress, their iron loss can be significantly higher than that in ordinary conditions. However, the induction principles of SIL are pretty complicated. Generally, the process of SIL calculation development can be illustrated in Figure 2-4. As seen, several significant achievements of the SIL estimation models can be summarized. These are the magnetic circuit model, Bertotti Giorgio model [54], Zhu's model [55] and orthogonal decomposition model [56]. These models take into

account both the alternating and rotating magnetic fields, but the skin effect is not fully considered, which may increase the SIL calculation errors in PMSMs. In [57], the authors studied the influence mechanism of skin effect on the SIL of high speed PMSMs, but the different magnetization modes were ignored.

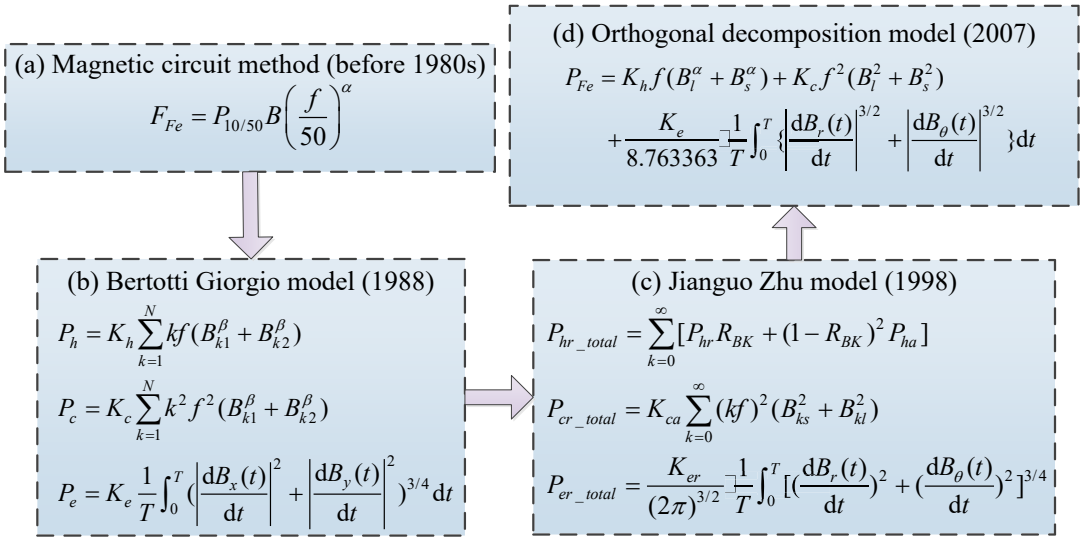

Figure 2-4 Development process of iron loss calculation models.

PM eddy current loss is mainly caused by the space harmonics and time harmonics of the armature winding magnetic field as well as slot opening. Different from common motors, in high speed PMSMs, the PM eddy current loss would have a substantial increase because it is proportional to the square of the magnetic field frequency. On the other hand, the high operating speed contributes to the extensive use of noncontact bearings, which may induce the rise of rotor temperature due to the poor rotor heat dissipation capability. Thus, the permanent magnet material performance may be deteriorated. And the PM eddy current loss can increase to a large extent [58]-[59]. Analytical models and FEM can usually be employed to calculate PM eddy current loss. Analytical models can not only greatly shorten the calculation processing time with good accuracy, but also build a bridge for the size and electromagnetic parameters for motors. However, the conductivity and permeability of rotor materials could change under different working conditions, which breaks the assumptions in analytical models. With the ignorance of core saturation, magnetic leakage as well as hysteresis effects, the calculation accuracy is sometimes reduced. Thus, FEM was proposed and used for further enhancing the modelling accuracy of the PM eddy current loss. In [58], 2D FEM was used to calculate the PM eddy current

loss of a PMSM with SPM and concentrated winding. The calculation speed of 2D FEM modelling is fast, but the influences of end effect and axial segmentation are ignored. In this case, researchers considered to use 3D FEM for the analysis of the PM eddy current loss. Zhao [59] *et al*. estimated the PM eddy current loss of high-speed axial flux permanent magnet motor by constructing a 3D FEM. Although experimental results verified the accuracy of the proposed methods, the huge time consumption is a problem to be solved. For suppressing PM eddy current loss, the motor structure and permanent magnet sleeve material can be optimized. Shrinking the width of the stator slot, adding the length of the air gap and choosing suitable protective sleeve material are all effective for reducing PM eddy current loss. Recently, scholars have also considered adding a thin non-magnetic metal shielding ring between the permanent magnet and the sheath of the rotor. Using the shielding effect of eddy current, the PM eddy current loss with the sheath and shielding ring can be limited [58].

Due to the violent friction between the rotor surface and the air gap, the air friction loss (AFL) in high speed PMSMs would be much larger than that of the common motors. Normally, AFL on the rotor radial surface and axial end surface can be calculated as (2-1) and (2-2) respectively [60].

$$P_{Af\_rad} = k_f C_f \pi \rho_{air} \omega^3 r^4 l \tag{2-1}$$

$$P_{Af\_end} = \frac{1}{2} C_f \rho_{air} \omega^3 (r_2^5 - r_1^5) \tag{2-2}$$

where k_f is the roughness coefficient of the rotor surface, C_f the radial surface air friction coefficient, l the rotor axial length, ρ_{air} the air density, and r_1 and r_2 are respectively the inside and outside radius of the rotor end surface, f the working frequency.

However, the air in high speed PMSMs air gap is in a turbulent state such that the friction coefficient is difficult to calculate accurately. Therefore, it is necessary to modify the empirical formula in conjunction with the computational fluid dynamic (CFD) simulation method. Through lots of studies, it is well known that the rotor size, rotation speed and surface roughness are key issues to induce the AFL. An effective measure that can reduce AFL is to add nonmagnetic conductive filler material into the stator slot. Therefore, the initial airflow can be smoothed and the fluid resistance can be reduced [60].

2.2.3 Electromagnetic Design

Electromagnetic design is a fundamental stage in the design of motors and drive systems, typically based on the following three models: analytical model, magnetic circuit model, and FEM. Compared to the analytical and FEMs, the magnetic circuit model offers advantages such as simplified computation, intuitive understanding, rapid iteration, and cost efficiency. Simplifying complex electromagnetic systems into equivalent magnetic circuits reduces computation time and complexity, facilitating quick evaluation and optimization of designs. Additionally, the magnetic circuit model can be combined with other models to maintain a certain level of accuracy while significantly lowering computational costs, making it widely used in motor performance analysis.

A traditional existing circuit model was introduced by Colby and Novotny [61]. As seen from Figure 2-5, an equivalent resistor was added in parallel with the internal voltage to predict iron losses. As the electromotive force is proportional to magnetic flux or flux density, the iron losses of the motor can be approximated as proportional to the square of the internal voltage. Moreover, the armature current is nearly zero under no-load conditions. That is, the voltage across the resistance equals the back electromotive force or terminal voltage. Thus, the equivalent iron loss resistance can be obtained from the no-load iron loss.

$$R_c \approx m\frac{E^2}{P_c} \tag{2-3}$$

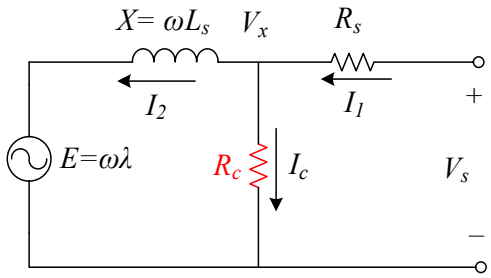

Figure 2-5 Equivalent circuit for PMSMs introduced by Colby and Novotny [61].

In Figure 2-5, E is the back EMF, R_c the equivalent core loss resistance, $X = \omega L_s$ the synchronous reactance, L_s the synchronous inductance, ω the rotor speed in electrical angular frequency, R_s the stator winding resistance, V_s the terminal voltage, I_1 the phase

current, I_2 the armature current. In (2-3), m is the number of phases, P_c the measured no-load iron loss.

Despite the advantages of this kind of equivalent circuit model (ECM), several issues still exist. For example, due to the rotor saliency, especially in IPMSMs, the d-axis inductance is not equal to the q-axis inductance [62]. Therefore, it is necessary to employ two equivalent circuits to account for the influence of the difference in d- and q-axis inductances. Secondly, most ECMs can only analyze the iron losses of PMSMs operating normally at synchronous speed. However, in variable speed conditions, a single-valued equivalent resistance model would always fail to accurately reflect and compute iron losses [63]. During the steady-state operation of a PMSM with a fixed terminal voltage, the iron losses computed from traditional ECMs typically remain almost constant across various loads, as the stator resistance is generally much smaller compared to the synchronous reactance. However, this contradicts the fact that the armature currents may lead to extra iron losses [64].

Additionally, in [63], the load iron loss of a three-phase PM claw-pole motor was calculated by the ECM of Figure 2-5. Assuming that the equivalent resistance R_c is linearly related to speed, (2-4) is used to compute the load iron loss. As seen, with the load or armature current increases, the iron loss increases. However, this formula may significantly overestimate additional iron losses due to the armature current. In fact, due to magnetic saturation, the total flux does not increase significantly, and the additional iron losses are mainly caused by flux waveform distortion.

$$P_c = 3\frac{V_x^{\,2}}{R_c} = 3\frac{E^2 + \left(XI_2\right)^2}{R_c} \tag{2-4}$$

2.2.4 Thermal Design

The maximum operating temperature of PMSMs is limited by the following factors: a) once the insulation working temperature is higher than the allowed value, the PMSM life expectancy would have a significant decrease, b) unbearable heat would also cause irreversible demagnetization of the permanent magnet, and c) high winding temperature can lead to an increase of thermal stress in relevant components as well as the decrease of rotor sleeve strength, especially composite sleeve [65]-[66]. All these problems show

that thermal field analysis is required and the corresponding heat dissipation of PMSMs should be designed to reduce the temperature rise. In general, there are three kinds of models for thermal analysis in PMSMs such as the lumped parameter thermal network (LPTN) model, FEM and the computational fluid dynamic model [65]-[68].

The LPTN method has obvious advantages in calculation speed such that it is suitable for temperature rise estimation in the motor design stage. However, LPTN takes too much time to calculate equivalent thermal resistance and heat dissipation coefficient. Moreover, a large number of assumptions and estimations may increase the error [65]. Currently, FEM is often used, in conjunction with LPTN, for 2D and 3D thermal analysis of electrical machines. With FEM, the motor can be modeled into 2D or 3D loaded with various loss densities and heat transfer conditions, which can obtain a more detailed temperature rise distribution than LPTN. But FEM suffers from the same problems as LPTN, namely, the heat transfer conditions at each boundary still need to be obtained with the help of fluid networks and empirical formulas. In addition, in terms of rapid parametric analysis, FEM performance is inferior to LPTN [65]-[66]. For this problem, FEM can be employed to correct and refine the equivalent thermal resistance that can then be used in the network or to investigate the detailed distribution of heat rise at the local part of the motor such as the conductor in the slot. On the other hand, considering that the majority of FEM electromagnetic packages include finite-element and thermal-analysis facilities, FEM can be regarded as a convenient solution in a very complex geometry which is not approachable with lumped parameters.

Meanwhile, based on the finite-volume technique, modern CFD codes can solve the Navier–Stokes equations complimented by a selection of validated and proven physical models, and then solve 3D laminar, turbulent flow and heat transfer with a high degree of accuracy. CFD can jointly model and solve the heat transfer entity of the motor, the internal and external cooling fluids as well as the internal temperature distribution [67]. In this case, LPTN or FEM temperature rise modelling methods can be completely replaced. Moreover, since it is no longer necessary to determine the convective heat transfer coefficient of each part with the help of the empirical method, the results can be more accurate and detailed. In spite of the advantages, CFD has the shortcomings of long modelling time and slow calculation speed. In recent years, there has been an application trend that combines all three calculation methods and uses their respective advantages to

analyze the motor temperature rise. In [68], combining CFD and FEM, the temperature rise of a 30 kW, 60000 r/min PMSM was calculated. The air gap heat transfer coefficient and the motor surface heat dissipation coefficient calculated by CFD are assigned to FEM as conditions. As a result, a large amount of calculation can be avoided while the accurate calculation of motor temperature rise distribution can also be realized. In conclusion, with the continuous improvement of computer software and hardware technologies as well as the increase of the pursuit of PMSM efficiency and power density, the application of CFD technology in heat transfer will become more and more extensive. The losses and permanent magnet working state are both directly related to the temperature. In order to accurately determine the working point and temperature rise, synthetic solutions should be performed through the coupling of power losses and thermal field analysis.

It should be pointed out that, in order to ensure the motor runs within the temperature limit, the design of a good cooling system is required by high speed or ultra high speed PMSMs. Air cooling, water cooling, oil cooling and hybrid cooling methods can usually be employed. In [69], various cooling equipment of high-speed motors was studied. It is found that compared with air cooling, oil cooling can reduce the loss of rotor surface ventilation, and can also effectively reduce the temperature rise of the rotor. However, oil cooling equipment has a complicated design task and takes up big space. Due to the drawbacks of oil cooling, air and water cooling methods are widely used in rotating electromechanical systems. The air cooling system is simple in structure, low in cost and convenient for management and maintenance, but it consumes a lot of electricity. Compared with water cooling, its cooling effect and efficiency are poor. The specific heat capacity of water is large. Compared with air cooling, the water cooling method is better in effectiveness, efficiency and power consumption, but features a complex structure and high cost. Usually, a specific cooling method needs to be selected in conjunction with the actual temperature distribution of the motor. There is no doubt that hybrid cooling may be more suitable for occasions with high power density requirements.

2.2.5 Mechanical Characteristics

Mechanical characteristic analysis is another important issue in the design and optimization of PMSMs, especially high speed PMSMs. Generally, the following three aspects including rotor material strength, bearing support and dynamic analysis should be

investigated. The first and the second aspects are often noncritical and can be readily satisfied through empirical design, whereas the third one requires special attention for most situations, especially those operated at high speeds. Dynamic analysis is generally used to calculate the natural frequency and dynamic response of the motor in operation.

The materials used in PMSM permanent magnet have poor tensile strength, which means that the rotor can easily be damaged by the centrifugal force caused by high speed and the thermal stress caused by temperature rise. Thus, it is necessary to ensure that the permanent magnet and matching protective sleeve can withstand the allowable stress by analyzing the rotor strength in static and high speed dynamic operating conditions. So far, various calculated methods, by using the analytical model as well as FEM, for the internal stress of permanent magnet and sleeve have been proposed [70]-[71]. Through the accurate rotor material strength analysis, the designer can optimize the rotor to meet the following conditions including (a) the internal stress of all components in the rotor is within the safe range, (b) there is always positive pressure between the parts in fit, (c) the permanent magnets always bear compressive stress under various working conditions, and (d) the internal stress of protective sleeve should not change significantly in the presence of varying speed and temperature.

Bearing support quality determines the operating stability and dynamic characteristics of the high speed PMSM rotor to a large extent. At present, four kinds of bearings such as ball bearings, oil-filled bearings, air bearings and magnetic bearings can be applied [72]. According to the collected data, it is seen that ball bearings are mainly used in PMSMs with low rated power while air bearings and magnetic bearings can usually be employed for high power, high speed electrical machines. Recently, a kind of bearingless electrical machine was proposed, in which the rotor can be suspended through electromagnetic force. Universities including Swiss Federal Institute of Technology Zurich [73], Darmstadt University of Technology [74], Jiangsu University [75] and Nanjing University of Aeronautics and Astronautics [76] have obtained the preliminary outcomes about the bearing-less motor. In summary, ball bearings possess the advantages of space saving and lost cost, but it has a relatively high failure rate. Additionally, the operational stability of the air bearing needs to improve while the force balance is a critical issue for the application of magnetic bearing.

Dynamics analysis is important for a rotating machinery. As for a PMSM, the key issues in terms of stability analysis, critical speed calculation and unbalance response are expected to be solved during the dynamic studies. The stability requires the rotor to return to its original operating status in the presence of external disturbances. Critical speed calculation can be utilized to the relief of vibration and noise coming from rotor unbalance as well as the avoidance of resonance. The unbalanced response is to analyze the sensitivity of vibration and noise to imbalance degree and to provide solutions for rotor unbalance [77].

Rotor dynamic analysis is generally conducted by the transfer matrix method and FEM. The former has been gradually abandoned due to the large errors. FEM is widely utilized for dynamic analysis with higher accuracy. Through the analysis by scholars, it is found that the bearing stiffness, shaft length, shaft diameter and the position of the bearing have significant influence on the rotor's natural frequency. Although a series of achievements in rotor dynamics have been published, nonlinear factors influence, parameter sensitivity analysis, bearing stiffness determination and dynamic experiments are still very difficult and more attention is needed in the process of design and optimization for PMSMs.

2.2.6 Control Methods Design

Converters and inverters are key components in power electronics design. Converters include AC-DC converters (which convert alternating current (AC) to direct current), DC-DC converters (which adjust direct current voltage), and AC-AC converters (which change the frequency and/or amplitude of alternating current). Inverters, on the other hand, convert direct current to alternating current and are widely used in motor drives and renewable energy systems. Switching schemes are also crucial for system efficiency, performance, and reliability. Hard switching can lead to higher losses and electromagnetic interference, while soft switching techniques, such as zero-voltage switching and zero-current switching, can mitigate these issues. Pulse-width modulation (PWM) controls output voltage and current by adjusting the duty cycle of the switches, and they are extensively used in motor drives. In order to reduce the current ripple, researchers have investigated various modulation methods, such as sinusoidal pulse width modulation (SPWM) [78], discontinuous PWM [79]-[80], bus-clamping PWM [81]-[82],

random PWM [83]-[84] and hybrid PWM [85]-[86]. The different modulation methods may produce different current/voltage waveforms and magnetic flux harmonics.

Control strategies play an essential function in the determination of dynamic- and static-state performances of electrical drive systems. Substantial efforts have been put forward for the development and application of various control algorithms in commercial drive systems, including traditional methods such as the field-oriented controller (FOC), direct torque controller (DTC) and constant voltage–frequency (V-F) ratio controller [87]-[92], as well as modern control strategies such as sensor-less controller (SLC), sliding mode controller, adaptive robust controller (ARC) and model predictive controller (MPC) [93]-[102].

Among the traditional control methods, the FOC decouples the stator current into an excitation component and torque component in the *d-q* coordinate system, so that the control of the AC motor can be equivalent to that of a separately excited DC motor [87]-[89]. FOC, proven to have superiorities concerning good control precision, wide speed regulating range and fast response speed, has been commonly applied in sorts of electric drive systems. Figure 2-6 (a) shows the schematic diagram of a FOC control scheme used in a PMSM drive system. The DTC abandons the decoupling idea of FOC, which calculates and directly controls the flux and torque of the motor in the stator coordinate system, as shown in Figure 2-6 (b). It is distinguished by the merits of fast dynamic response, simple structure (thus low cost) and strong robustness against motor parameter variation. However, the torque and flux ripples reduce the performance in low-speed conditions, and the excessive acoustic noises restrict DTC application [90]-[91]. The V-F control is a kind of open-loop control, such that it can hardly complete the real-time control of machines [92].

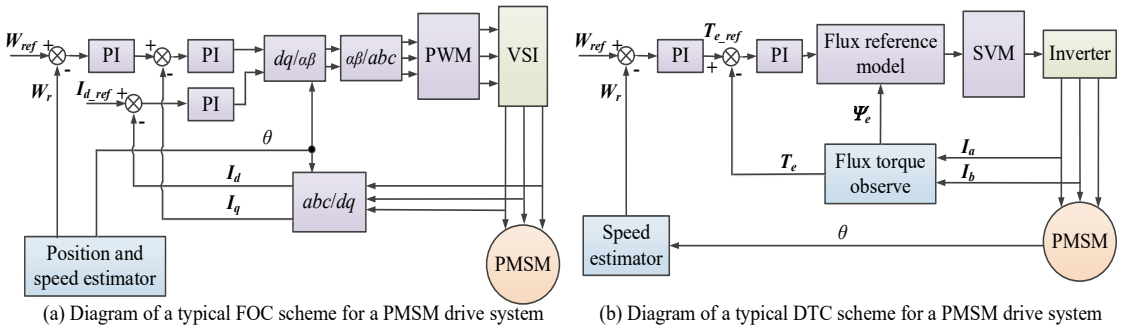

(a) Diagram of a typical FOC scheme for a PMSM drive system

(b) Diagram of a typical DTC scheme for a PMSM drive system

Note: I_d and I_q stand for the *d*- and *q*-axis currents, respectively. Ψ_e is the flux, T_e the torque. For FOC, the *d*-axis current is set to zero for achieving the maximum torque per ampere. The current/torque loop and speed loop are set as feedback loops to keep the reference speed W_{ref} as well as to make a smaller *d*-axis reference current I_{d_ref}.

Figure 2-6 Control diagrams of typical FOC and DTC for PMSM drive systems.

The ever-developing modern industry has contributed to the widespread investigations of modern control strategies, among which the SLC, SMC, ARC and MPC are the most studied and widely used methods. To save costs and reduce the impacts of external disturbances on sensors, SLC was proposed to obtain the rotor position through calculation instead of sensors. So far, estimation methods using an open loop, fuzzy adaptive algorithm and an observer can be used for rotor position when the machines work at relatively high speeds, while high frequency signals are often employed to predict the rotor position in low-speed conditions [93]-[94]. Sliding mode controller, originally proposed by Utkin [95], possesses excellent features including simple algorithm derivation, a fast response speed and strong robustness for handling parameter uncertainties and external disturbances, which has been widely used in many plants. To guarantee convergence properties and to relieve the chattering phenomenon, fractional calculus can be integrated into sliding mode controller for PMSM control [96]-[97]. Results in [96]-[97] showed the improved control performance of sliding mode controller, especially for dealing with uncertain and nonlinear systems, e.g., electric drive systems. In combination with the functions of adaptive control in handling unstructured uncertainties and robust control in attenuating disturbances, Yao and Tomizuka presented ARC [98]-[99] and proved that it could handle both structured and unstructured uncertainties. In [100], Yin *et al*. presented an adaptive robust backstepping controller with an extended state observer (ESO), as shown in Figure 2-7, for the speed regulating drive system of a new-type hybrid drive wind turbine. Experimental results illustrated excellent control performances under disturbances from both wind wheel and power grid ends. Taking advantage of the development of artificial intelligence (AI), MPC with an advanced predictive algorithm was investigated and applied to electrical machines. This kind of control strategy does not need the fixed control model but has three basic parts. These are model prediction, iterative optimization and feedback correction. MPC has the merits of good robustness and dynamic performance used in complex industrial processes, but requires improvements in terms of stability, anti-interference ability and model adaptability [101]-[102].

In industrial applications, engineers should choose the control strategy and the matching processors according to the machine characteristics and operating scenarios to guarantee

the best control performance and price/performance ratio. Meanwhile, more and more innovative control methods for PMSM drive systems will be presented based on the development of modern control theory, which will break through the limitations of traditional controllers and achieve parameter identification & control more easily by using artificial intelligence algorithms.

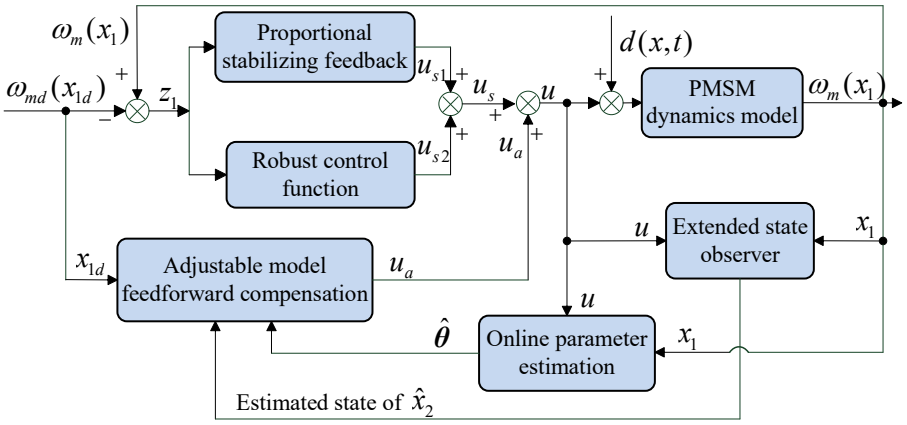

Note: $x_1 = \omega_m$, $x_{1d} = \omega_{md}$, $\boldsymbol{\theta} = [\theta_1 \ \ \theta_2]^{\mathrm{T}} = [k_t/J \ \ B/J]^{\mathrm{T}}$. $d(x, t) = T_L / J$ and represents the lumped disturbances. ω_m is the PMSM rotor angular velocity, T_L the load torque or lumped disturbances, B the viscous friction coefficient, J the rotational inertia. $k_t = 1.5\, p\psi_f$, and p is the number of poles, ψ_f the flux linkage of permanent magnet.

Figure 2-7 Control diagrams of adaptive robust backstepping controller with ESO for PMSM drive systems.

2.3 Performance Optimization

The design optimization of PMSMs and their drive systems is a high-dimensional and high-nonlinear problem, coupled with the characteristics of being multi-objective and multi-disciplinary. Through the significant efforts of researchers, the design optimization of electric drive systems has been developing very fast. The most important parts of the design optimization process include (a) design methods with analysis models, and (b) optimization methods with algorithms. The first stage aims to provide enough information including motor/controller parameters and performance evaluations for the development of optimization models, while the second stage can be utilized to improve motor performance via optimization algorithms or strategies.

2.3.1 Optimization Models

In the design optimization process of PMSMs, due to high rotation speed and sometimes special operating requirements, severe uncertainties appear in different physical fields including the electromagnetic, thermal and mechanical fields. Coupled with intense interaction and conflict among these physics, it is necessary to establish optimization models with multi-physics analysis [103].

Figure 2-8 shows the design framework of modern PMSMs regarding the multi-physics analysis, which can also be used by other types of electrical machines. As shown, the first step is to define the motor specifications, mainly including the cost, output power, working efficiency, temperature rise and resonance frequency. Then, the key designs/selection process, related to the motor topology, dimension, material and manufacturing method, needs to be investigated based on the defined constraints. After that, multi-physics analysis models, composed of electromagnetic models, thermal models and mechanical models with vibration and noise analysis, can be developed. Finally, the performance of the designed motor needs to be evaluated and then utilized for the next optimization [104].

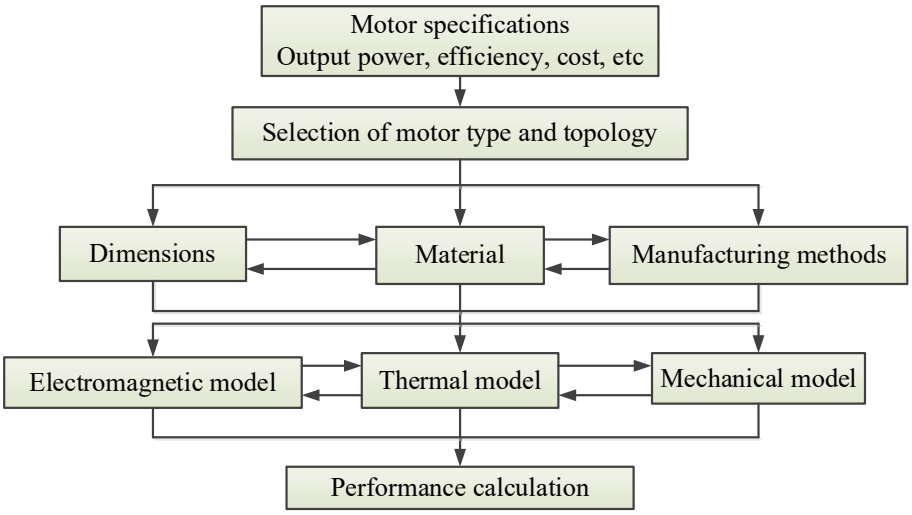

Figure 2-8 Design framework of PMSMs and other electrical machines with multi-physics analysis.

In view of a single-objective minimization optimization problem with N constraints, the multiphysics design optimization model of PMSMs can be shown as follows [104]:

$$\begin{aligned} &\min: f(\boldsymbol{X}) \\ &\text{s.t.} \quad g_i(\boldsymbol{X}) \le 0, \quad i = 1,2,\cdots N \\ &\qquad \boldsymbol{X}_l \le \boldsymbol{X} \le \boldsymbol{X}_u \end{aligned} \tag{2-5}$$

where $\boldsymbol{X}$ is the design parameter vector, $\boldsymbol{X}_u$ and $\boldsymbol{X}_l$ are respectively the upper and lower boundaries of $\boldsymbol{X}$, and f(*) and g(*) are respectively the objective function and constraints.

In (2-5), different multi-physics constraints should be defined via (2-6).

$$\text{Constraints:} \begin{cases} g_1(B_{ry}) \le 0, \quad g_1'(B_{st}) \le 0, \quad g_2(P_c) \le 0 \\ g_3(\Delta T_w) \le 0, \quad g_3'(\Delta T_{st}) \le 0, \quad g_3''(\Delta T_{sy}) \le 0 \\ g_4(\rho_p) \le 0, \quad g_5(\eta) \le 0, \quad g_6(P_{out}) \le 0 \\ g_7(T_{lm}) \le 0, \quad g_8(\delta_t^d) \le 0, \quad g_8'(\delta_{VM}^d) \le 0 \end{cases} \tag{2-6}$$

As shown, eight key constraints are commonly used in multi-physics optimization. These are respectively related to (a) the flux density at the rotor yoke (B_{ry}) and stator tooth (B_{st}), (b) the residual contact pressure between magnets and rotor iron (P_c), (c) the maximum temperature rise of the winding (ΔT_w), stator tooth (ΔT_{st}) and yoke (ΔT_{sy}), (d) the power density (ρ_p), (e) the efficiency (η), output power (P_{out}), (f) the maximum torque per loss per mass (T_{lm}), (g) the total rotating tangential stress (δ^d_t), and (h) the equivalent Von Mises stress (δ_{VM}^d).

Considering the design optimization process of PMSMs, there are many design parameters, objectives and constraints. For example, maximizing the average torque or torque density and motor efficiency as well as minimizing the cost, loss and volume, weight and torque ripple can all be selected as direct optimization objectives. At the same time, some other parameters are also closely related to the performance of motors, such as magnetic flux density, air gap, back-*emf*. These parameters are often selected as indirect optimization objectives for motors [103]. Therefore, the design optimization is normally a multi-objective optimization problem. The multi-objective optimization model with p objectives and N_d constraints can be established as (2-7).

$$\begin{aligned} &\min: \left\{ f_{d1}(\boldsymbol{X}_d), f_{d2}(\boldsymbol{X}_d), \cdots f_{dp}(\boldsymbol{X}_d) \right\} \\ &\text{s.t.} \quad g_{di}(\boldsymbol{X}_d) \le 0, \quad i = 1,2,\cdots N_d \\ &\qquad \boldsymbol{X}_{dl} \le \boldsymbol{X}_d \le \boldsymbol{X}_{du} \end{aligned} \tag{2-7}$$

where $\boldsymbol{X}_d$ is the design parameter vector, $\boldsymbol{X}_{du}$ and $\boldsymbol{X}_{dl}$ are the upper and lower boundaries of $\boldsymbol{X}_d$, f_d and g_d are the objective functions and constraints, respectively.

Theoretically, the multi-objective optimization solutions are always a compromise among different objectives. That is, to obtain the optimum for each of these objectives is always impossible. In this case, one can only acquire the non-inferior solutions that can be called as Pareto optimal solutions by the way of getting the objectives as close as possible to their optimums. However, different from the solutions of single-objective optimization, the Pareto solutions may have a very large or even infinite number, which should be passed around as evenly as possible at the front of Pareto solutions. The Pareto front in multi-objective optimization is the set of all non-dominated solutions [103]. A specific case of Pareto optimal front with two objective functions is shown in Figure 2-9. It can be seen that points 'B' and 'C' are located at the Pareto frontier. Then, the results solved from 'B' and 'C' are the Pareto optimal solutions. Moreover, based on the definitions, it can be considered that the solutions of points 'B' and 'C' dominate the solutions of point 'A'. So far, plenty of algorithms such as multi-objective genetic algorithm (MOGA), nondominated sorting genetic algorithm (NSGA) and the improved NSGA II and multi-objective particle swarm optimization (MPSO) methods can all be utilized for completing the design and optimization of various multi-objective problems [105].

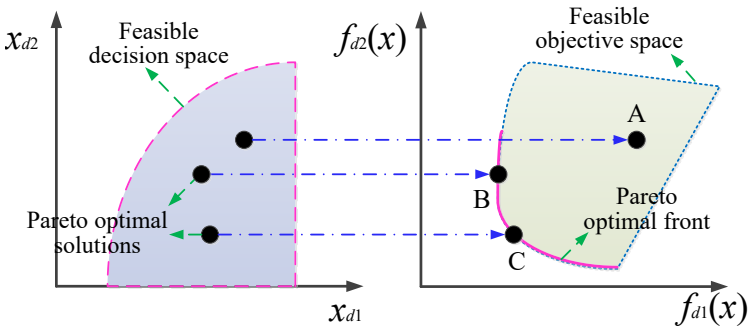

Figure 2-9 A specific case of the Pareto optimal solution.

Among them, the NSGA II is an improved version of the NSGA and can also be called as public toolboxes in some software. It is one of the most efficient and famous multi-objective evolutionary algorithms and has been widely applied in many kinds of engineering multi-objective optimization problems [106]-[107]. Figure 2-10 shows a flow chart of the NSGA II algorithm. As seen, the method includes two important components: the non-dominated sorting approach and the crowd comparison operator.

2.3.2 System Level Optimization

With the purpose of further improving the operating performance of PMSM, the steady-state performance such as torque, average output power, and efficiency, as well as the dynamic responses including settling time, speed overshoot and torque ripple should be considered comprehensively. Generally, during the design optimization, multi-physics analysis of the motor is always required to estimate these steady-state performances, while simulation analysis for the control systems of the machines needs to be conducted to evaluate the dynamic responses. Moreover, electric drive systems have become a popular part of future applications, which aim to integrate electrical machines and control systems together. Therefore, the system-level design optimization of the whole electric drive system is very meaningful in the future to ensure the best optimal system performance, instead of assembling the motor, inverter and other individual optimized components into a drive system [108].

Figure 2-11 illustrates a succinct system-level design optimization framework of electric drive systems with a particular PMSM and its control system. As shown, there are five key steps: (a) determine system requirements and specifications for input, (b) select the motor type, drive and controller units according to the system specifications, (c) jointly design the motor and controller, (d) construct design optimization models for the whole system including both the motor and controller, and (e) evaluate the system performance [109].

To guarantee system-level performances of the drive systems, a system-level multi-objective model can be derived by combining the motor and controller design optimization models.

$$\begin{aligned} &\min: f_s(\boldsymbol{x}_s) = F(f_{mi}, f_{cj}), \quad i = 1,...,P_m; j = 1,...,P_c \\ &s.t. \quad g_{mi}(\boldsymbol{x}_s) \le 0, \quad i = 1,...,N_m \\ &s.t. \quad g_{ci}(\boldsymbol{x}_s) \le 0, \quad i = 1,...,N_c \\ &\boldsymbol{x}_{sl} \le \boldsymbol{x}_s \le \boldsymbol{x}_{su} \end{aligned} \tag{2-8}$$

where $\boldsymbol{x}_s = [\boldsymbol{x}_m, \boldsymbol{x}_c]$ is the decision variable set; $\boldsymbol{x}_m$ and $\boldsymbol{x}_c$ are the parameter vectors of motor level and control level, respectively; $\boldsymbol{x}_{sl}$ and $\boldsymbol{x}_{su}$ are the lower and upper boundaries of $\boldsymbol{x}_s$. f_s is the system-level objective, which is generally a function of motor level objectives f_{mi} and control level objectives f_{ci}; P_m and P_c are the numbers of objectives,

while N_m and N_c are the numbers of constraints in motor and control levels, respectively. All the objectives and constraints should be defined in advance according to the requirements/specifications of applications.

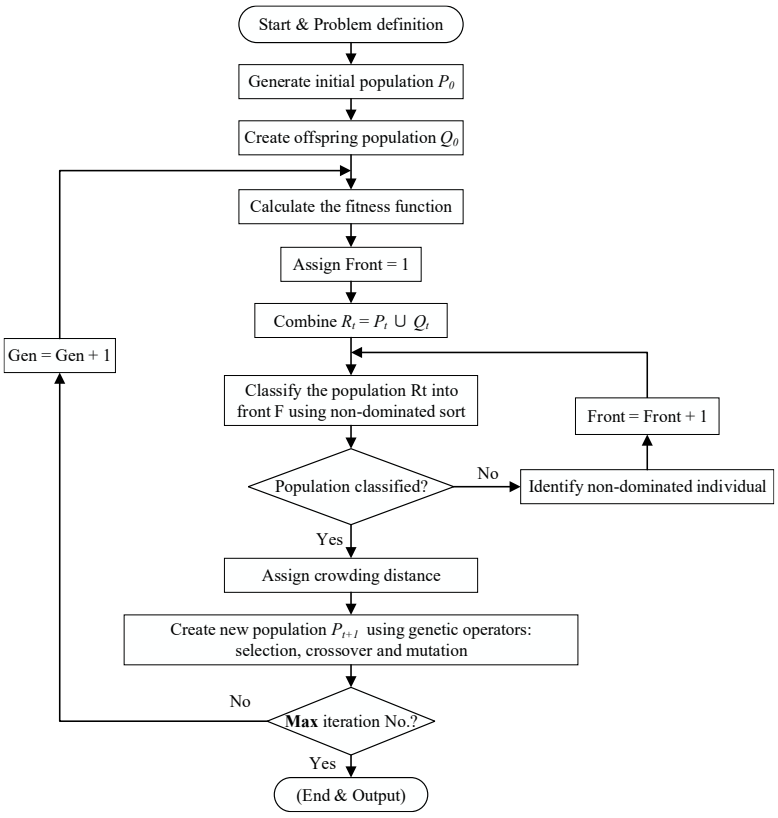

Figure 2-10 Flowchart of the NSGA II algorithm.

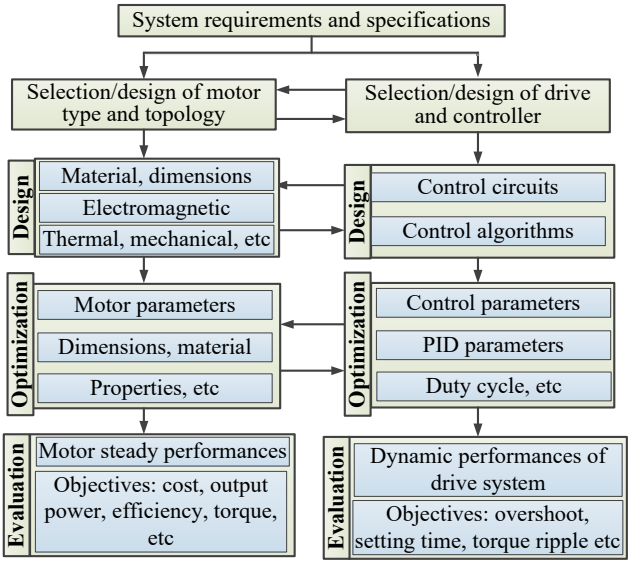

Figure 2-11 System-level design optimization framework for an electric drive system with specific PMSM and control system.

2.3.3 Single-level Optimization Method

The conventional one is simple in implementation that can be used to evaluate objectives and constraints by optimizing the physical models (such as analytical, magnetic circuit, FEM and thermal network models). For example, taking advantage of electromagnetic analysis's analytical models, the conjugate gradient and sequential quadratic programming algorithms have been successfully used to realize the design optimization of several kinds of motors. Additionally, intelligent algorithms and FEM can also be coupled (genetic algorithm (GA) &FEM, differential evolution algorithm (DEA) &FEM and MOGA&FEM) in conventional optimization methods [110]. Generally, the conventional direct optimization method can present good optimal design schemes for electrical machines by using an optimization algorithm such as GA. Although the classical optimization methods are relatively simple to implement, the optimization accuracy cannot always be guaranteed, especially for the high-dimensional design and optimization of PMSMs. The main reason lies in that the number of limited samples is insufficient for approximate models to replace FEM with satisfactory accuracy for high-dimensional problems. These challenges by using classical or traditional direct optimization methods based on both FEMs and the approximation models have contributed to the investigation of new optimization strategies.

2.3.4 Multi-level Optimization Method

The design optimization of PMSMs is generally a non-linear multi-physics and multi-objective problem. In this process, a number of design parameters should be considered and may have different sensitivities related to different design objectives. Additionally, more attention should also be paid to reducing the huge computation cost required by conventional methods when high dimensional optimization problems exist. To address these challenges and better optimize the sensitive parameters, a kind of new multi-level optimization strategy is recently investigated, by which the initial big and high-dimensional design parameter space can be refined into two or three low dimensional subspaces by using sensitivity analysis methods for all the covered parameters [111]. The key flowchart for the multi-level optimization method with three subspaces is given in Figure 2-12.

As shown, compared to conventional methods, with the multi-level optimization method, the initial high and big dimensional design space is divided into three subspaces ($\mathbf{X}_1$, $\mathbf{X}_2$ and $\mathbf{X}_3$). The first subspace ($\mathbf{X}_1$) includes all the highly significant factors, and all the significant factors are in the second subspace ($\mathbf{X}_2$), while all the non-significant factors fill the third subspace ($\mathbf{X}_3$). The design optimization of subspaces $\mathbf{X}_1$, $\mathbf{X}_2$ and $\mathbf{X}_3$ can be realized one by one, and the optimization results in the up-level can be used in the next level. It is seen that for each subspace, the dimensions are much smaller than that in the initial space. As a result, the general optimization approximate models can be utilized in all sublevels and the calculation complexity can be reduced.

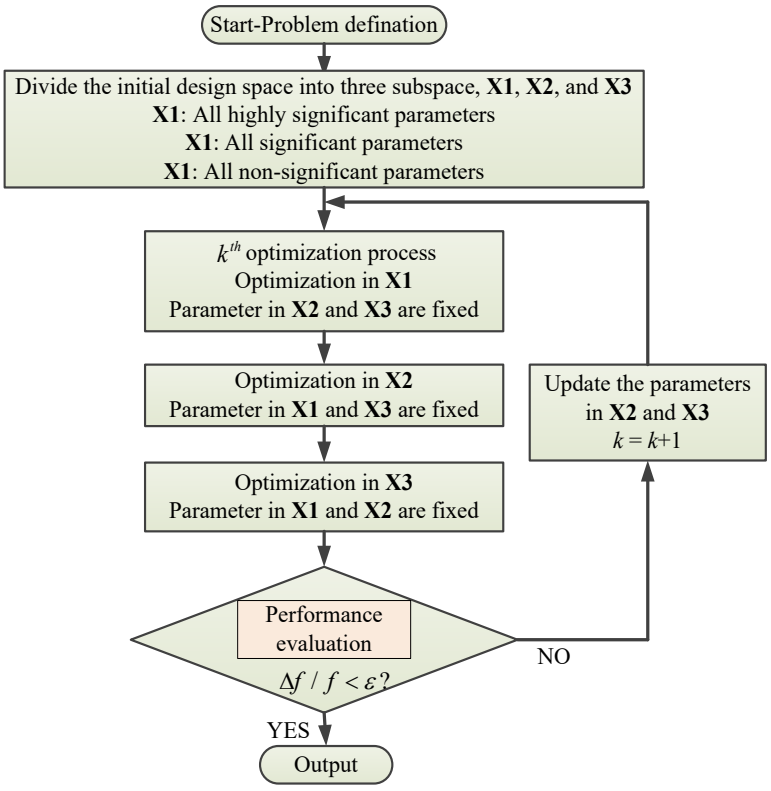

Figure 2-12 Flowchart for the multi-level optimization method.

The first step involves categorizing all optimization variables based on their correlations with the optimization objectives, grouping them into highly important, important, and less important categories. Common correlation measures, such as the Pearson correlation coefficient, mutual information, and Design of Experiments, can be utilized for this purpose. Among these, the Pearson correlation coefficient is widely preferred for assessing the relationships between objectives and decision variables efficiently, even

when dealing with a large number of parameters. It also stands out for its intuitive interpretation, robustness with normally distributed data and computational simplicity.

The Pearson correlation coefficient $\rho(\mathbf{X}, \mathbf{Y})$ between two variables **X** and **Y** is defined as the covariance of the two variables cov(**X**, **Y**) divided by the product of their standard deviations $\sigma_{\mathbf{X}}$ and $\sigma_{\mathbf{Y}}$, as given in (2-9).

$$\rho(\mathbf{X},\mathbf{Y}) = \frac{\mathrm{cov}(\mathbf{X},\mathbf{Y})}{\sigma_{\mathbf{X}}\sigma_{\mathbf{Y}}} = \frac{\mathrm{E}(\mathbf{X}-\mu_{\mathbf{X}})(\mathbf{Y}-\mu_{\mathbf{Y}})}{\sigma_{\mathbf{X}}\sigma_{\mathbf{Y}}} \tag{2-9}$$

As $\mu_{\mathbf{X}} = \mathrm{E}(\mathbf{X})$, $\sigma_{\mathbf{X}}^2 = \mathrm{E}[(\mathbf{X}-\mathrm{E}(\mathbf{X}))^2] = \mathrm{E}(\mathbf{X}^2) - \mathrm{E}^2(\mathbf{X})$, the same transformation also works for **Y**, in this case, (2-9) can be updated as:

$$\rho(\mathbf{X},\mathbf{Y}) = \frac{\mathrm{E}(\mathbf{XY}) - \mathrm{E}(\mathbf{X})\mathrm{E}(\mathbf{Y})}{\sqrt{\mathrm{E}(\mathbf{X}^2) - \mathrm{E}^2(\mathbf{X})}\sqrt{\mathrm{E}(\mathbf{Y}^2) - \mathrm{E}^2(\mathbf{Y})}} \tag{2-10}$$

The above equation defines the population correlation coefficient. However, in practical calculation, the sample standard deviations s_x and s_y need to be estimated to obtain the sample Pearson correlation coefficient with:

$$\rho(\mathbf{x},\mathbf{y}) = \frac{\sum x_i y_i - n\overline{\mathbf{xy}}}{(N_s-1)s_{\mathbf{x}}s_{\mathbf{y}}} = \frac{N_s\sum x_i y_i - \sum x_i \sum y_i}{\sqrt{N_s\sum x_i^2 - (\sum x_i)^2}\sqrt{N_s\sum y_i^2 - (\sum y_i)^2}} \tag{2-11}$$

For practical computation, statistical software such as NumPy or SciPy in Python, R language, MATLAB and SPSS can all be employed to calculate sample Pearson correlation coefficient.

In our previous publications [112], we have extensively discussed the Kriging model and NSGA II algorithm used in the design optimization of electric drive systems. Specifically, the conventional direct optimization method employs design analysis models such as FEM and thermal network model to evaluate the objectives and constraints in the optimization models (2-8), and optimizes all parameters at once by using an optimization algorithm like genetic algorithms. This method is simple in implementation. For example, it can be realized by integrating Matlab and Ansys. While FEM is widely used nowadays in the design analysis of electrical machines due to its high accuracy, the computation costs are very high [113] and usually more than 10,000 evaluations of the optimization model are required. For a motor with 3D FEM, it may require half a minute or more for

one simulation, and then at least 10,000 minutes (around 166 hours or 7 days) will be required to obtain an optimal solution. This is a huge computation burden for most designers. To address this issue, some approximate models (or surrogate models) like response surface model, radial basis function model, and the Kriging model have been developed and applied to the optimization of electrical machines [10]. Among them, considering that the Kriging model has better modelling capability of local nonlinearities, and has no significant differences in the computation speeds, it was selected to evaluate the objectives and constraints in our optimization. The principles of the Kriging model method are given as follows.

Given n sample points $\{\mathbf{x}_1; \mathbf{x}_2; \ldots; \mathbf{x}_n\}$ and their responses $\{y(\mathbf{x}_1); y(\mathbf{x}_2); \ldots; y(\mathbf{x}_n)\}$, for an input $\mathbf{x}$, the response value $y(\mathbf{x})$ of the Kriging model can be expressed as:

$$y(\mathbf{x}) = f(\mathbf{x})^T \boldsymbol{\beta} + z(\mathbf{x}) \tag{2-12}$$

where $f(\mathbf{x})^T\boldsymbol{\beta}$ is a deterministic term for global modelling, $f(\mathbf{x})$ is a known approximation model, which is generally assumed as a polynomial and has the form of $f(\mathbf{x}) = [f_1(\mathbf{x}), f_2(\mathbf{x}), ..., f_q(\mathbf{x})]^T$, where q is the dimension of polynomial, $\boldsymbol{\beta}$ is the model parameter vector to be estimated, and $z(\mathbf{x})$ is a random error term used for the modelling of local deviation, which is usually assumed to be a vector with the mean of zero, variance of σ^2 and covariance matrix of:

$$c_{ij} = \sigma^2 \mathbf{R}[R(\mathrm{x}_i, \mathrm{x}_j)] \tag{2-13}$$

where $\mathbf{R}$ is the correlation matrix, and R the user-specified correlation function.

Adopting the commonly used Gaussian correlation functions, one can express the correlation matrix as:

$$\mathbf{R} = \begin{bmatrix} r(\mathbf{x}_1,\mathbf{x}_1) & r(\mathbf{x}_1,\mathbf{x}_2) & \cdots & r(\mathbf{x}_1,\mathbf{x}_n) \\ r(\mathbf{x}_2,\mathbf{x}_1) & r(\mathbf{x}_2,\mathbf{x}_2) & \cdots & r(\mathbf{x}_2,\mathbf{x}_n) \\ \vdots & \vdots & \ddots & \vdots \\ r(\mathbf{x}_n,\mathbf{x}_1) & r(\mathbf{x}_n,\mathbf{x}_2) & \cdots & r(\mathbf{x}_n,\mathbf{x}_n) \end{bmatrix} \tag{2-14}$$

where

$$r(\mathbf{x}_i,\mathbf{x}_j)=\exp\left\{-\sum_{k=1}^{D}\alpha_k\left|\mathbf{x}_{ik}-\mathbf{x}_{jk}\right|^2\right\} \tag{2-15}$$

By using the best linear unbiased estimation in statistics, the predictor of $y(\mathbf{x})$ and parameter $\boldsymbol{\beta}$ can be expressed as follows.

$$\hat{y}(\mathbf{x})=f(\mathbf{x})^T\hat{\boldsymbol{\beta}}+r(\mathbf{x})^T\mathbf{R}^{-1}\left(\mathbf{y}-\mathbf{F}\hat{\boldsymbol{\beta}}\right) \tag{2-16}$$

$$\hat{\boldsymbol{\beta}}=\left(\mathbf{F}^T\mathbf{R}^{-1}\mathbf{F}\right)^{-1}\mathbf{F}^T\mathbf{R}^{-1}\mathbf{y} \tag{2-17}$$

where $\mathbf{F}$, $r(\mathbf{x})$ and $\mathbf{y}$ are defined as:

$$\mathbf{F}=\begin{bmatrix} f_1(\mathbf{x}_1) & f_2(\mathbf{x}_1) & \cdots & f_q(\mathbf{x}_1)\\ \vdots & \vdots & \vdots & \vdots \\ f_1(\mathbf{x}_n) & f_2(\mathbf{x}_n) & \cdots & f_q(\mathbf{x}_n)\end{bmatrix} \tag{2-18}$$

$$r(\mathbf{x})=\begin{bmatrix} R(\mathbf{x},\mathbf{x}_1)\\ \vdots \\ R(\mathbf{x},\mathbf{x}_n)\end{bmatrix} \tag{2-19}$$

and

$$\mathbf{y}=\left[y(\mathbf{x}_1),y(\mathbf{x}_2),\ldots,y(\mathbf{x}_n)\right]^{\mathrm{T}} \tag{2-20}$$

Using the maximum-likelihood estimation method, the estimation of σ^2 is:

$$\hat{\sigma}^2=\frac{1}{n}\left(\mathbf{y}-\mathbf{F}\hat{\boldsymbol{\beta}}\right)^T\mathrm{R}^{-1}\left(\mathbf{y}-\mathbf{F}\hat{\boldsymbol{\beta}}\right) \tag{2-21}$$

The estimation of α_k in correlation function can be obtained from maximum-likelihood estimation. As $z(\mathbf{x})$ follows a n-dimensional normal distribution with zero and covariance $\sigma^2\mathbf{R}$, the probability density function of error is:

$$p(\mathbf{Y};\boldsymbol{\beta})=\frac{1}{\sqrt{(2\pi)^n\left[\det(\sigma^2\mathbf{R})\right]}}\exp\left\{\frac{(\mathbf{Y}-\mathbf{H}\boldsymbol{\beta})^T\mathbf{R}^{-1}(\mathbf{Y}-\mathbf{H}\boldsymbol{\beta})}{-2\sigma^2}\right\} \tag{2-22}$$

Substituting the predicted $\boldsymbol{\beta}$ and σ^2, i.e. (2-17) and (2-21), into the above equation, the only unknown parameter α_k can be estimated.

In summary, implementing the Kriging method consists of estimating the parameters **β** in (2-12), σ^2 in (2-13), and the parameters α_k in Gaussian correlation functions (2-15). All the parameters can be estimated by the software package DACE (Design and Analysis of Computer Experiments).

Taking advantage of the multi-level optimization method, in [114], Putek *et al*. synthesized a multi-level set method with the incorporation of a topological gradient to optimize the topology of a permanent magnet machine. In [115], the optimization of all sensitive parameters of permanent magnet synchronous generators was realized through both dual-level response surface methodology and Booth's algorithm by Asef *et al*. Then, a multi-level design optimization method for a double-stator permanent magnet synchronous motor was also proposed, by which the rotor weight and mechanical stress distribution in the rotor core are effectively reduced [116]. In [117], a multi-level optimization design method for the flux-concentrating permanent-magnet brushless machine was proposed with considerations of permanent-magnet demagnetization limitation. Results showed that the optimized motor's output torque was increased while the torque ripple was greatly decreased. In our previous works [118]-[119], the multi-level optimization method with sensitivity analysis was employed for various types of electrical machines.

The above-mentioned achievements published on the same topic have shown the significant advantages of multi-level methods in improving optimization performance and calculation efficiency, which have contributed a lot to the research and development of design optimization for electric machines. However, the following critical issues still need to be solved: (a) The sensitivities of the design parameters are usually calculated separately, which means that the correlations or mutual sensitivities among different design parameters are neglected. Thus, the accuracy of optimization results may be affected. (b) In previous works, researchers fully considered the correlations between optimization parameters and objectives, without giving concerns about the correlations among different optimization objectives fully. So far, cross-factor variance analysis and Pearson correlation coefficient methods can be utilized to classify the optimization objectives. (c) It is difficult to set multiple objectives for each optimization level since only Pareto solutions can be obtained without specific parameters, and traditional methods cannot be used. Future works about multi-level optimization should be carried

out to solve problems in terms of analyzing correlations of design parameters and objectives, as well as selecting the key points from Pareto solutions of each level. Consequently, multi-objective optimization can be employed at each level and the final optimization accuracy can thus be guaranteed.

2.3.5 Space Reduction Sequential Optimization Method

Apart from the multi-level optimization method, the sequential optimization method is another kind of space reduction strategy for completing the design optimization of electrical machines, especially with the considerations of inevitable uncertainties in manufacturing processes [120]. In contrast to the multi-level method, the idea of the sequential optimization method is to reduce the unnecessary waste in computation costs that come from the samples outside the interested subspaces [121]. Figure 2-13 illustrates the flowchart of a multi-objective sequential optimization method for electric machines.

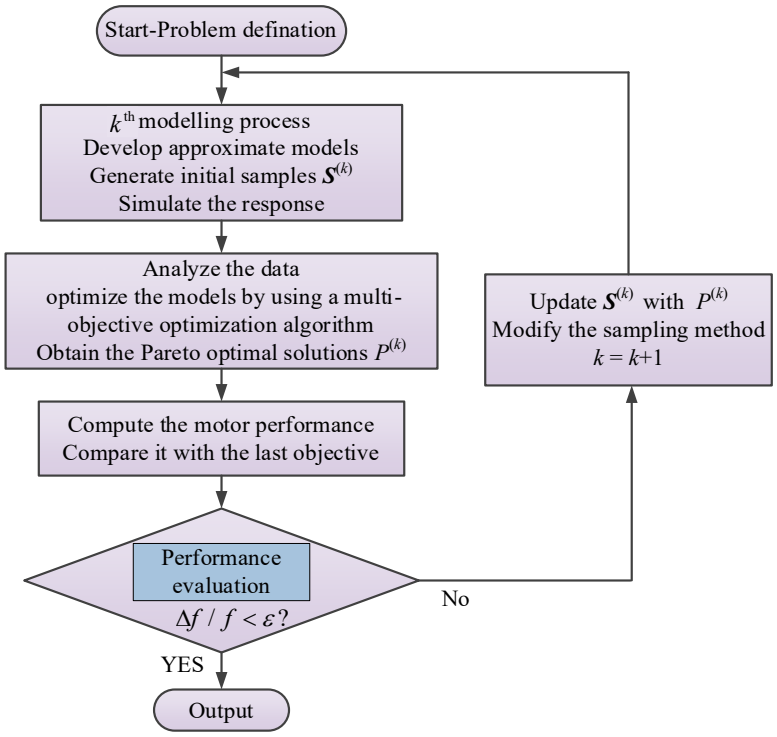

Figure 2-13 Flowchart for space reduction sequential optimization method.

Generally, the shape of interesting spaces is a critical issue in this method, which requires an advanced space reduction method to guarantee optimization accuracy. Based on the modified central composite design technique, a multi-objective sequential optimization

method was presented [121]. In [120], by using a convergence measure consisting of an orthogonal design method and a hyper-volume indicator, the authors proposed a multi-objective sequential optimization method for electrical machines' deterministic and robust design optimization. Case studies verified that, once the proposed method is employed, the motor performance can be enhanced and the computational cost can also be reduced by about 10–40% compared with that of the direct optimization method (like DEA plus FEM).

Although the sequential optimization methods are efficient for the optimization of PMSMs, these strategies are difficult to use for extremely high-dimensional optimization problems due to the high computation cost of FEM. Moreover, since the sequential optimization method is a kind of iterative optimization, the efficiency of the sequential optimization method is not highly dependent on the type of surrogate models.

2.4 Multi-disciplinary Design Optimization Method

Explanations concerning the multi-physics nature of PMSMs indicate that the design optimization processes of electrical machines and their drive systems are complex and challenging since multiple disciplines such as structural mechanics, electromagnetics, heat transfer and control, as well as multi-constraints and multi-objectives should be involved. Moreover, the related disciplines are not isolated but normally strongly coupled. In this case, the systematic multi-disciplinary analysis and optimization method can be utilized to achieve the multi-objective optimization of electric drive systems in modern applications such as wind power generation and electric vehicles, which need challenging specifications.

Figure 2-14 shows the basic framework of the systematic multi-disciplinary optimization method. At the disciplinary level, the indirect optimization models (IOMs) for optimization variables, constraints, objectives and models can be obtained by the analysis and modelling of electrical machines in different disciplines based on the methods (such as the LPTN model, FEM and CFD methods) introduced in the electromagnetic design part. Then, system level optimization variables, constraints, objectives and models can be derived by using collaborative algorithms to finally complete the systematic multi-disciplinary optimization of a specific electrical drive system. In [122], the multi-disciplinary design optimization method was utilized for the drive systems based on

permanent magnet machines with soft magnetic composite cores. The results showed the satisfactory optimization performance of the multi-disciplinary optimization method in terms of increasing motor reliability, reducing computation costs and improving the performance quality for drive systems.

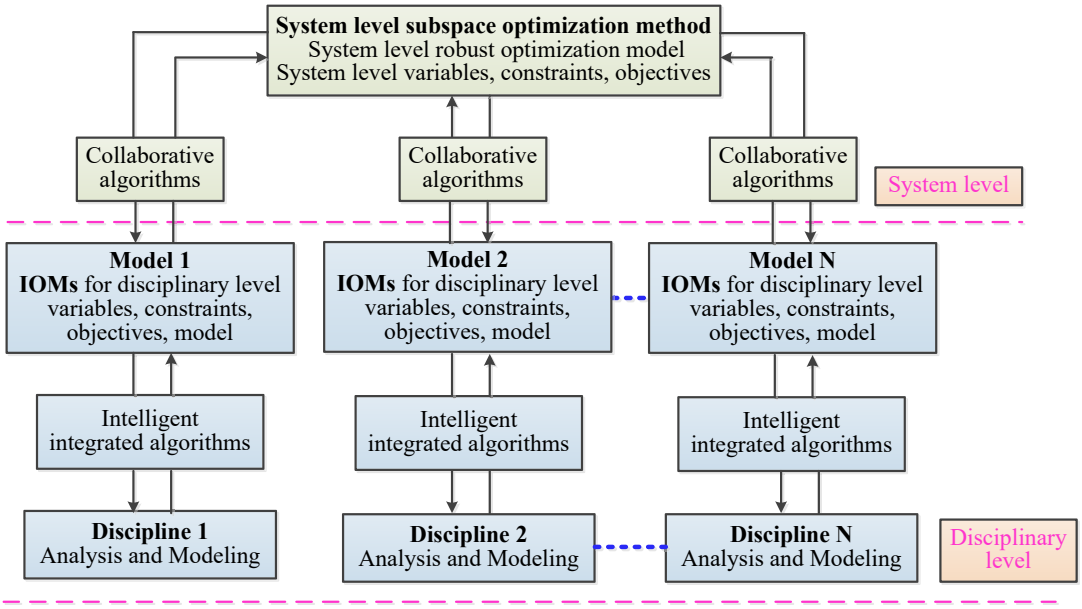

Figure 2-14 Flowchart for systematic multi-disciplinary optimization method.

2.5 Conclusion and Comments

2.5.1 Conclusion

The literature review covers methods for motor design optimization, primarily introducing multidisciplinary design analysis models for motors and drive systems. These models encompass various fields, including material science, loss analysis, electromagnetic design, thermal/mechanical models, topologies, and controller types. Based on general design optimization methods, the review outlines the relevant steps of design optimization and provides a detailed overview of techniques for establishing optimization objective models and algorithms for searching for optimal solutions. To make the development process of motors and drive systems more automated, flexible, and integrated, the literature proposes the topic of application-oriented system-level design optimization and introduces two novel and efficient optimization algorithms.

2.5.2 Comments

(1) A significant highlight of the review is its focus on the integration trend in application-oriented motor drive systems. The literature underscores the importance of system-level design optimization to meet practical needs, particularly by incorporating multidisciplinary factors into the modelling process. This is crucial for addressing real-world challenges in motor design.

(2) One of the key areas discussed is iron loss modelling, which is vital given its substantial contribution to total losses in PMSMs. The complex formation mechanisms of iron loss directly impact the efficiency of the motors. Therefore, the literature rightly emphasizes the need for detailed iron loss modelling within the broader context of system-level loss models.

(3) Moreover, the literature advocates for the introduction of minimum loss controllers to further reduce losses from the controller's perspective. This approach aligns with the overarching goal of enhancing system efficiency. The emphasis on developing a system-level optimization model that includes both motor and control aspects is particularly noteworthy.

(4) Given the high-dimensional and nonlinear characteristics of these optimization problems, the literature proposes the need for efficient optimization algorithms. This is an important consideration, as traditional single-stage optimization methods based on finite element or approximate models face challenges in high-dimensional design optimization problems.

(5) The literature's proposal of application-oriented system-level design optimization and the introduction of two novel and efficient optimization algorithms are timely and relevant. These contributions are poised to make the development process of motors and drive systems more automated, flexible, and integrated, which is essential for advancing the field.

Chapter 3

Advanced Iron Loss Prediction Models Considering Multiphysics Factors

3.1 Introduction

The topology of IPMSMs has been considered suitable for driving EVs under complex operating conditions, thanks to its advantages in the areas of weight and space saving, efficiency improvement, speed range expansion as well as control performance promotion [123]. However, the iron loss of IPMSMs can be significantly interfered by the time-varying working conditions and coupling effects of multiphysics factors like magnetic, thermal and mechanical stress field distributions [124]. Moreover, the harmonics of non-sinusoidal magnetic flux in the motor stator, caused by both stator slotting structure and PWM inverter, would result in additional iron loss [125].

In this case, the development of an accurate iron loss calculation technique, as a prerequisite for the design and optimization of IPMSMs in EVs, has attracted great research interest from academia and industry worldwide. Recently, the finite element analysis (FEA) based on the well-known Bertotti model has shown satisfactory performances for calculating iron loss with reasonable accuracy. In [126], the FEA was utilized to predict the iron loss and the magnet eddy current loss of PMSMs with concentrated windings. In [127] and [128], the iron loss calculation models accounting simultaneously for magnetic hysteresis and eddy currents were investigated for steel laminations at high frequencies by using the FEA method. In [129], the influence of iron loss on IPMSM electromagnetic characteristics was evaluated based on the inverse solution of the flux linkages extracted via FEA. In [130], the iron loss caused by fringing fluxes in an axial-flux PMSM was calculated through FEA. Although the FEA can estimate iron losses conveniently for nonlinear problems with complex structures, it is time-consuming, which poses a great difficulty in the design optimization process of PMSMs with a large number of iterations. Moreover, the impacts of multiphysics factors

such as temperature and stress on motor performance cannot be easily distinguished. It is therefore strongly desired to develop iron loss calculation methods that cannot only greatly shorten the calculation time, but also indicate the interactions of motor parameters, while maintaining the calculation accuracy.

To reduce the computational cost, alternative iron loss calculation methods based on analytical models have been proposed. For instance, the magnetic equivalent circuit (MEC), as a promising analytical method, has been applied to estimate the iron loss and analyze the operating performance as well as the relationship between static and dynamic flux densities for various electrical machines [131]-[133]. However, the MEC calculation accuracy might be discounted since this method prefers the average core magnetic density to the harmonic component, without giving enough consideration to the iron loss from the harmonic contribution. Meanwhile, in EVs, it is impractical for a drive motor to work only under definite and standard conditions. Non-sinusoidal flux density waveforms with rich harmonics can impact significantly on iron loss characteristics.

According to the sources, there exist two types of flux density harmonics: the spatial harmonics due to stator slotting and the carrier harmonics generated by the PWM inverter. To reveal the influences of harmonics, analytical iron loss models are investigated by taking into account both the spatial and carrier harmonics. In [134] and [135], an analytical iron loss calculation method was proposed for a spoke-type in-wheel PMSM with bridge saturation and magnetic field harmonics. In [136], aiming at the influence of harmonics, an analytical iron loss calculation method was proposed for an integer-slot IPMSM during flux weakening, in which a harmonic loss voltage and a harmonic loss coefficient were added to the iron loss resistance model. The relationship between the harmonic additional loss and the harmonic voltage was analyzed. Experimental results reported in [137] indicate that the iron losses of electrical machines fed by PWM inverters could be almost three times higher than those fed by the ideal sinusoidal currents. Similar results were also reported in [138]-[140].

The abovementioned studies have shown successful progress in improving the speed and accuracy of iron loss prediction in electrical machines in the presence of either spatial or carrier harmonics. However, in the presence of both spatial and carrier harmonics, substantial work is still needed to improve the analytical iron loss prediction model. Furthermore, since the magnetic properties including iron losses are susceptible to

temperature and mechanical stress [141], [142], the interaction of multiphysics effects, such as thermal and stress characteristics, also needs to be considered to improve the iron loss prediction accuracy for the design and optimization of PMSMs.

To address the above-mentioned issues, this chapter proposes an improved analytical iron loss prediction model for IPMSMs utilized as the drive motor of EVs. The novelty is mainly manifested in that the influences of different physical factors including both the spatial harmonics from slotting and carrier harmonics due to PWM inverter, the temperature and compressive stress on iron loss are fully considered in the proposed analytical models. The prediction accuracy can be improved while the computational burden is reduced.

3.2 Problem Formulation and Models

Classically, Bertotti's iron loss separation model, consisting of hysteresis loss density P_h, eddy current loss density P_e and additional loss density P_{ad}, has been commonly employed for calculating iron loss density in silicon steel sheets. Under sinusoidal magnetization, the total iron loss density P_{total} in a silicon steel sheet sample can be calculated by:

$$P_{total} = P_h + P_e + P_{ad} \tag{3-1}$$

with

$$\begin{cases} P_h = K_h \dfrac{\omega_s}{2\pi} B_m^{\alpha} \\ P_e = \dfrac{d^2}{12\eta_{Fe}\rho_{Fe}} \dfrac{1}{T}\int_0^T \left(\dfrac{dB(t)}{dt}\right)^2 dt = K_e \dfrac{1}{T}\int_0^T \left(\dfrac{dB(t)}{dt}\right)^2 dt \\ P_{ad} = \dfrac{\sqrt{\sigma_{Fe} GVS}}{\rho_{Fe}} \dfrac{1}{T}\int_0^T \left|\dfrac{dB(t)}{dt}\right|^{3/2} dt = K_{ad} \dfrac{1}{T}\int_0^T \left|\dfrac{dB(t)}{dt}\right|^{3/2} dt \end{cases} \tag{3-2}$$

where ω_s is the motor angular frequency, B_m the amplitude of the magnetic flux density, d the thickness of the silicon steel sheet, S the cross-sectional area of the iron core, G=0.1375 a dimensionless constant, $\sigma_{Fe}=1/\eta_{Fe}$ the conductivity, V a parameter characterizing the statistical distribution of local coercive fields, T the excitation period. η_{Fe} and ρ_{Fe} are the resistivity and density of core material, respectively. K_h and α are both hysteresis loss empirical coefficients, and $1.8 \le \alpha \le 2.2$. $K_e = d^2/(12\eta_{Fe}\rho_{Fe})$ is defined as

the eddy current loss coefficient while $K_{ad} = \sqrt{\sigma_{Fe} GVS} / \rho_{Fe}$ is set as the additional loss coefficient.

Since the additional loss generally accounts for only a small percentage of the total iron loss [143], it is ignored in the iron loss calculation, and according to (3-2), the accurate estimation of magnetic field and coefficients K_h and K_e is crucial for calculating iron loss.

3.2.1 Iron Loss Considering Slot Harmonics

Unlike the ideal case of iron loss estimation in a silicon steel sheet sample under sinusoidal magnetization, the calculation of iron loss in a PMSM must consider both the fundamental and harmonic flux density waveforms. While there exist two types of harmonics, this subsection calculates the iron loss by taking into account the spatial harmonics due to the stator slotting and rotor structure. To consider the effects of spatial harmonics, the stator is divided into the tooth and yoke regions. The hysteresis and eddy current losses in each region are predicted separately with consideration of non-sinusoidal flux density waveforms.

(i) Iron loss model of tooth region

The hysteresis loss is proportional to the area enclosed by the quasi-static hysteresis loop, which is mainly related to the fundamental frequency of magnetic flux density, temperature rise and compressive stress instead of the waveform harmonics. In contrast, the eddy current loss highly depends on the waveform harmonics, and to calculate the eddy current loss, the harmonics of non-sinusoidal flux density waveforms must be considered [144]. Because of the complexity of harmonic evaluation process, by using FEM, the tooth flux density waveform is transformed into piecewise linear or trapezoidal waveform, as shown in Figure 3-1. Under the magnetization of trapezoidal waveform, the eddy current loss density of the tooth can be calculated as [145]:

$$P_e = K_e \frac{1}{T} \sum_{i=1}^{N_{Li}} \int_{t_{i-1}}^{t_i} \left(\frac{dB_i(t)}{dt}\right)^2 dt \tag{3-3}$$

where N_{Li} is the number of linear intervals.

For the tooth region, the non-dominant longitudinal component of flux density can be ignored [145], and the time required for a magnet to pass a slot pitch can be expressed as:

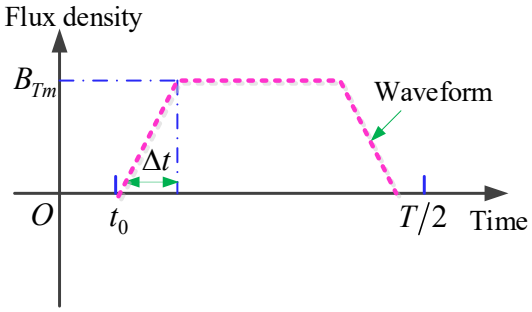

Figure 3-1 Flux density waveform in the tooth region.

$$\Delta t = \frac{T}{2}\frac{1}{N_R N_S} \tag{3-4}$$

where N_R and N_S are the numbers of phases and slots per pole per phase of the PMSM, respectively.

For a trapezoidal waveform, the changing rate of flux density with respect to time can thus be transformed into:

$$\frac{dB_T(t)}{dt} = \frac{B_{Tm}}{\Delta t} \tag{3-5}$$

As shown in Figure 3-1, the mutation of flux density change rate happens four times in one excitation period. In this case, based on (3-3), the eddy current loss density in the tooth region can be expressed by:

$$P_{eT} = K_e \frac{4}{T}\left(\frac{B_{Tm}}{\Delta t}\right)^2 \Delta t \tag{3-6}$$

Substituting Δt of (3-4) into (3-6), one obtains

$$P_{eT} = 8K_e N_R N_S \left(\frac{B_{Tm}}{T}\right)^2 \tag{3-7}$$

The iron loss in the tooth region can be calculated by:

$$P_{totalT} = P_{hT} + P_{eT} = K_h \frac{\omega_s}{2\pi} B_{Tm}^{\alpha} + 8K_e N_R N_S \left(\frac{B_{Tm}}{T}\right)^2 \tag{3-8}$$

where P_{totalT} and P_{hT} are the total iron loss density and hysteresis loss density in the tooth region, respectively.

(ii) Iron loss model of yoke region

In this subsection, the flux densities in the yoke region are also considered as piecewise linear with trapezoidal waveform obtained by using FEM, as shown in Figure 3-2. However, the calculation of the yoke iron loss density is not the same as that for the tooth region, which should be estimated separately with both longitudinal and normal components. Moreover, although the rise and fall times of flux density in the yoke are independent of the position along the radial direction, the amplitude of flux density normal component depends highly on the position [145]. Thus, the eddy current loss models of yoke region are derived under longitudinal and normal components, respectively.

To calculate the eddy current loss due to the longitudinal component, a quantity

$$\beta = \frac{pW_m}{2\pi r} \tag{3-9}$$

is defined to represent the coverage of the width of magnet, where p is the number of poles, W_m the effective width of magnet for the V-shaped IPMSM, and r the rotor outer radius.

The time required by a magnet to rotate from one point to another in the yoke can be expressed as:

$$\Delta t_1 = \frac{W_m}{r\omega_{mech}} \tag{3-10}$$

where ω_{mech} is the motor mechanical speed and $\omega_{mech}=2\omega_s/p$.

Substituting (3-9) into (3-10), one obtains

$$\Delta t_1 = \frac{\beta\pi}{\omega_s} \tag{3-11}$$

During Δt_1, as shown in Figure 3-2 (a), the variation of longitudinal flux density is $2B_{Lm}$, and

$$\frac{dB_L(t)}{dt} = \frac{2B_{Lm}}{\Delta t_1} = \frac{2\omega_s B_{Lm}}{\pi\beta} \tag{3-12}$$

This change happens twice during an excitation period. Substituting B_L in (3-12) as B_i in (3-3), one obtains the average eddy current loss density in the yoke due to the change of longitudinal flux density as:

$$P_{eYL} = 8K_e \frac{\omega_s B_{Lm}^2}{\pi\beta T} \tag{3-13}$$

The eddy current loss due to the varying normal component of flux density is also estimated. Figure 3-2 (b) shows the normal component of flux density waveform in the yoke, where $B_N(x)$ is the magnitude of normal component at distance x from the outer edge of the yoke. By employing the theoretical quadric fitting method [145], $B_N(x)$ can be expressed as:

$$B_N(x) = (ax + bx^2)B_{Lm} \tag{3-14}$$

where a and b are the fitting coefficients.

The time required by a magnet to rotate for one slot pitch can be calculated by:

$$\Delta t_2 = \frac{\Delta x}{r\omega_{mech}} \tag{3-15}$$

$$\Delta x = \frac{2\pi r}{pN_S} \tag{3-16}$$

where N_S is the number of slots per pole per phase

During this time period, the flux density normal component varies linearly with the amount of $B_N(x)$, and can be noted as $B_N(x,t)$. The variation rate of normal component is calculated by:

$$\frac{\partial B_N(x,t)}{\partial(t)} = \frac{N_S}{\pi}\omega_s B_N(x) \tag{3-17}$$

Combining (3-3), (3-15), (3-16) and (3-17), one can obtain the eddy current loss density due to the flux density normal component at point x as:

$$P_N(x) = 4K_e \frac{N_S \omega_s}{\pi T} [B_N(x)]^2 \tag{3-18}$$

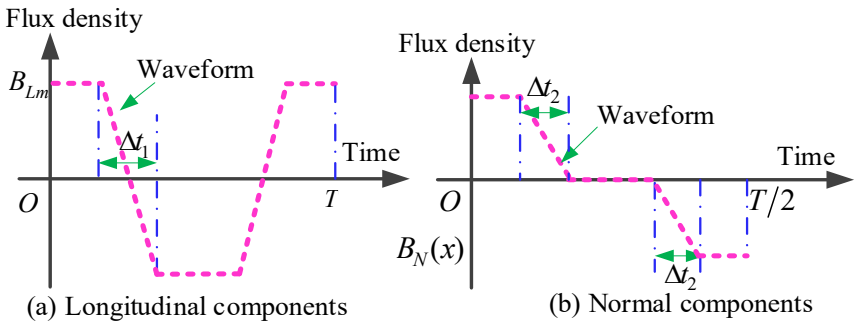

Figure 3-2 Flux density waveforms in the yoke region.

By integrating $P_N(x)$ over x, the average loss density due to the normal component can be obtained as:

$$P_{eYN} = C_N \cdot 4K_e \frac{N_S \omega_s}{\pi T} B_{Lm}^2 \tag{3-19}$$

where

$$C_N = \frac{a^2}{3} + \frac{ab}{2} + \frac{b^2}{5} \tag{3-20}$$

The total iron loss in the yoke region can be obtained as:

$$\begin{aligned} P_{totalY} &= P_{hY} + P_{eYL} + P_{eYN} \\ &= K_h \frac{\omega_s}{2\pi} B_{Lm}^{\alpha} + 8K_e \cdot \frac{\omega_s B_{Lm}^2}{\pi \beta T} + C_N \cdot 4K_e \frac{N_S \omega_s}{\pi T} B_{Lm}^2 \end{aligned} \tag{3-21}$$

Finally, by multiplying the total iron loss densities of the tooth and yoke by the corresponding volumes, the total stator iron loss can be estimated as:

$$P_{iron\_1} = P_{totalT} V_T + P_{totalY} V_Y \tag{3-22}$$

where V_T and V_Y are the tooth and yoke volumes, respectively.

3.2.2 Iron Loss Considering PWM Carrier Harmonics

The iron loss prediction model shown in (3-22) can account for the effects of magnetic field spatial harmonics and distribution, but it is derived under the assumption that the motor is driven by sinusoidal current input. However, the drive motors for EV are supplied by inverters and operate for a wide range of speed and torque, which generates extra iron loss due to the carrier harmonics.

As shown in Figure 3-3, the distorted current injected by the inverter can produce minor hysteresis loops and generate additional hysteresis loss. Additional eddy current loss can also be produced by the flux density harmonics caused by the PWM carrier. To describe the effects of PWM carrier harmonics on iron loss prediction, an improved model is applied. A coefficient k_{h_PWM} is introduced to revise the calculation equations of hysteresis loss while the models of eddy current loss are updated by summing all the eddy current losses caused by harmonics, as given below [146].

$$\begin{cases} P_{h\_PWM} = k_{h\_PWM} P_h \\ P_{e\_PWM} = \sum P_{e\_PWM}(n) \end{cases} \tag{3-23}$$

$$k_{h\_PWM} = 1 + C_h \frac{1}{B_m} \sum_{a=1}^{N} \Delta B_a \tag{3-24}$$

where P_{h_PWM} and P_{e_PWM} are the hysteresis and eddy current losses considering PWM carrier harmonics. $P_{e\_PWM}(n)$ is the eddy current loss caused by the n^{th} PWM harmonic, C_h the constant coefficient between 0.6 and 0.7 which depends on the lamination properties, and ΔB_a denotes the fluctuation in motor flux density, as seen in Figure 3-3.

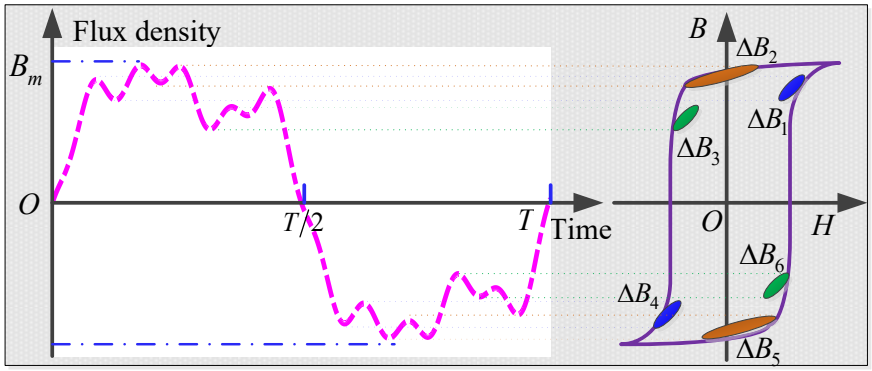

Figure 3-3 Distorted flux density waveform with PWM inverter supply.

In the above-mentioned model, $P_{e\_PWM}(n)$ can be estimated from the flux density harmonics. According to the Faraday's law, the relationship between the supply voltage and flux density can be expressed as:

$$u(t) = N_W S \frac{dB}{dt} \tag{3-25}$$

where N_W is the number of winding turns.

Assuming that the output voltage of the PWM inverter, marked as $v(t)$, is a periodic function, the stator terminal voltage can be expressed as (3-26) by using Fourier decomposition.

$$\begin{aligned} v(t) &= \sum_{n}^{\infty} V_n \cos 2n\pi ft \\ &= V_0 + V_1 \cos \omega_s t + V_2 \cos 2\omega_s t + V_3 \cos 3\omega_s t + \cdots \end{aligned} \tag{3-26}$$

If the PWM inverter is well controlled, the positive and negative parts of the PWM waveform are symmetrical. No direct current component and even-order harmonics exist, and (3-26) can be transformed into:

$$v(t) = V_1 \cos 2\pi ft + \sum_{n=3,5,7,\cdots}^{\infty} V_n \cos 2n\pi ft \tag{3-27}$$

where f is the fundamental frequency of the PWM waveform.

Substitute (3-27) into (3-25). After integration, the expression of magnetic flux density can be illustrated via:

$$B(t)=\frac{1}{N_W S}\left(\sum_{n=1,3,5,\cdots}^{\infty}\frac{V_n}{2n\pi f}\sin 2n\pi ft\right) \tag{3-28}$$

Thus, the magnitude of the n^{th} harmonic of flux density is

$$B_{mn}=\frac{1}{N_W S}\frac{V_n}{2n\pi f} \tag{3-29}$$

where V_n is the magnitude of the n^{th} harmonic voltage, and can be estimated from the magnitude of fundamental voltage V_1 by:

$$\begin{cases} V_n=\dfrac{4J_h\left(\dfrac{\gamma k\pi}{2}\right)}{k\pi\gamma}V_1 \\ n=k\varepsilon\pm h \\ \text{while } k=1,3,5\cdots, \quad h=3(2j-1)\pm 1, j=1,2,3\cdots \\ \text{while } k=2,4,6\cdots, \quad h=\begin{cases}6j+1, j=0,1\\ 6j-1, j=1,2,\cdots\end{cases} \end{cases} \tag{3-30}$$

where J_h is the Bessel function, γ the modulation ratio, and ε the carrier ratio.

To reduce the computing burden, the Bertotti model is employed to predict the additional eddy current loss density due to the n^{th} carrier harmonic, as the following.

$$P_{e\_PWM}(n)=K_e B_{mn}^2 f_n^2=K_e\left(\frac{1}{N_W S}\frac{V_n}{2n\pi f}\right)^2 f_n^2=K_e\left(\frac{1}{2\pi N_W S}\right)^2 V_n^2 \tag{3-31}$$

where f_n is the frequency of the n^{th} harmonic. Combining (3-8), (3-21), (3-22), (3-23), (3-24) and (3-31), the iron loss model in the presence of non-sinusoidal magnetic flux density and PWM carrier harmonics can be obtained as:

$$P_{iron\_2} = \left(k_{h\_PWM}^{T} P_{hT} + P_{eT}\right) V_T + \left(k_{h\_PWM}^{Y} P_{hY} + P_{eYL} + P_{eYN}\right) V_Y + \left[K_e \left(\frac{1}{N_W S} \right)^2 \sum_{i=3,5,7\ldots}^{n} \left(\frac{V_n}{2\pi} \right)^2 \right] \left(V_T + V_Y\right) \tag{3-32}$$

3.3 Iron Loss Considering Multiphysics Factors

To incorporate multiphysics uncertainties including thermal and stress effects, the iron loss model of (3-32) is updated.

3.3.1 Iron Loss with Thermal Effect

Since the properties of core materials are sensitive to temperature, the influence of temperature should be reflected on iron loss. It is well known that the temperature effect mainly acts on the material resistance that is proportional to its length L, and inversely proportional to its cross-sectional area A_{CS}, namely,

$$R = \frac{\eta(T_{\circ C})L}{A_{CS}} \tag{3-33}$$

where R is the resistance of the material, and $\eta(T_{\circ C})$ is the material resistivity varying with temperature $T_{\circ C}$.

Therefore, both K_h and K_e are related to $T_{\circ C}$, or

$$\begin{cases} K_h = K_h(T_{\circ C}) \\ K_e = K_e(T_{\circ C}) = \dfrac{d^2}{12\eta_{Fe}(T_{\circ C})\rho_{Fe}} \end{cases} \tag{3-34}$$

According to the theory of linear relationship, $\eta_{Fe}(T_{\circ C})$ can be estimated by:

$$\eta_{Fe}(T_{\circ C}) = \eta_{Fe}^{0}(1 + \mu_T \Delta T_{\circ C}) \tag{3-35}$$

where η_{Fe}^{0} is the equivalent resistivity of materials at the room temperature, μ_T the temperature coefficient obtained by fitting the iron loss curve under different

temperatures, and $\Delta T_{\mathcal{C}}$ the temperature variation.

3.3.2 Iron Loss with Stress Effect

Apart from the temperature effect, the remaining stress in silicon steel sheet, caused by punching, cutting and pressing, etc., is another important motivating factor responsible for the performance degradation, which would induce the enhancement of iron loss due to the newly arranged internal magnetic domain. To update the stress effect, the iron loss coefficients K_h and K_e should also be functions of stress, and can be noted as $K_h(\sigma)$ and $K_e(\sigma)$.

3.3.3 Measurement of Rotational Magnetic Properties

Since the first measurement of 2D rotational magnetic properties was reported by Baily in 1896 [147], a number of 2D rotational property measuring systems and techniques have been developed [148]–[150]. Of these measurement systems, the square sample single sheet tester, which was developed by Brix *et al*. [151], has proven to be the most favorable, thanks to its high control flexibility on rotating magnetic field patterns, outstanding uniformity of magnetic flux density distribution in the sample and, hence, high measurement accuracy.

Led by J. Zhu, the University of Technology Sydney Magnetic Testing Group developed a square sample single sheet tester [152], which has been used to measure different magnetic materials. This tester is cooperated via a computerized digital signal process system, and it is able to measure the ***B***-***H*** relations as well as the core losses under 1D alternating fluxes in any specific direction, or 2D circularly and elliptical rotating fluxes with different axis ratios. Figure 3-4 shows the schematic diagram of the square single sheet tester and the whole system. The tester contains yokes made up of laminated grain-oriented electrical sheets, and the yoke shapes were designed to form four wedge-type magnetic poles. Two excitation coil groups are wound around the X- and Y-axes, and

each group has two coils, which are connected in series. A square sample of magnetic material is installed in the middle of the tester, where a magnetic field is generated by the X- and Y-axes excitation currents.

The 2D magnetic field in the sample is produced with the currents flowing in the two sets of excitation coils on X- and Y-axes. The excitation currents are provided by two power amplifiers. Through controlling the magnitudes, phase angles and waveforms of the excitation currents, any 1D or 2D magnetic flux density vector can be produced, e.g., a 1D alternating flux density inclined at a specific angle from the X- or Y-axis, a circularly or elliptically rotational flux density or a flux density of any specified locus. Two dedicated differential amplifiers with low and high pass filters are used for the feedback control of the flux density components on the axes. The function generation and data acquisition are both realized by a PC-based digital signal processing system.

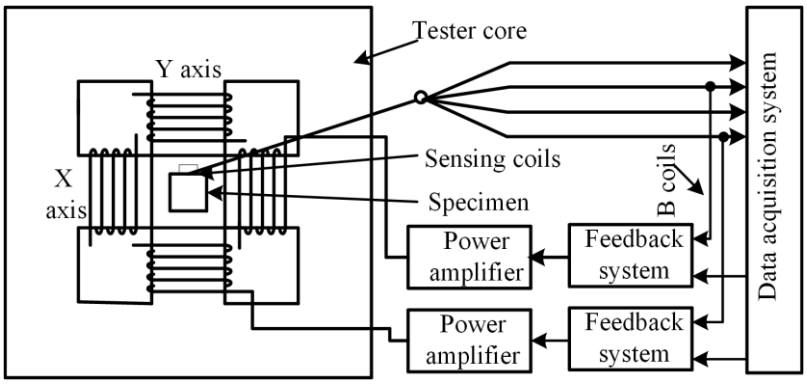

(a)

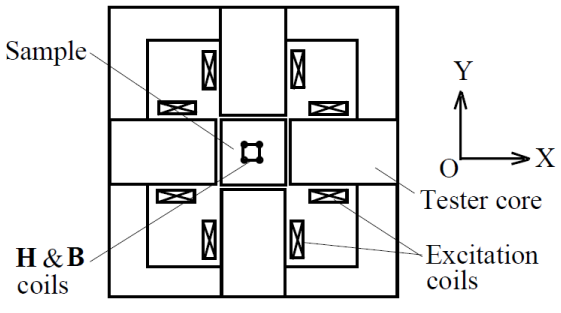

(b)

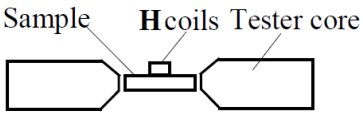

(c)

Figure 3-4 Principle diagram of the 2D rotating magnetic property test system: (a) schematic diagram, (b) single sheet tester for square sample and (c) positions of sample and ***H*** search coils.

To acquire the ***B-H*** relation and associated core loss, the magnetic flux density inside the sample and the magnetic field strength on the surfaces should be measured accurately. As shown in Figure 3-4, the magnetic flux density and field strength in the sample can be acquired by the ***B*** and ***H*** sensing coils connected to the sample. Fifteen turns of enamel insulated copper wire of 0.1 mm in diameter are threaded through four small holes to form a B coil on each axis, as illustrated in Figure 3-5. The perforation is tiny and has little effect on the magnetic field distribution inside the sample. For accurate measurement, the flux density should be uniformly distributed in the sample, which is realized by the optimal design of the tester, particularly the shape and dimensions of the magnetic poles.

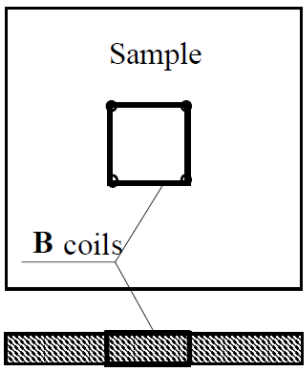

Figure 3-5 Arrangement of 2D ***B*** coils.

The magnetic flux density on one axis can be computed by:

$$B_i = \frac{1}{N_{Bi} A_{Bi}} \int V_{Bi} dt \quad i = x, y \tag{3-36}$$

where A_{Bi} is the cross-sectional area, N_{Bi} is the number of turns, and V_{Bi} the induced voltage across the terminals of the ***B***-coil on the axis.

The surface ***H*** coils, as shown in Figure 3-4 (c), are applied to measure the 2D magnetic field strength. According to the Ampere's law, the field strength on the surface would be equal to that just inside the sample if there were no surface currents. The ***H***-sensing coils can be fabricated very thinly, and they can be attached on the sample surface and thus the true value of the field strength inside the sample can be acquired. The magnetic field strength component on one axis can be computed by:

$$H_i = \frac{1}{\mu_0 K_{Hi}} \int V_{Hi} dt \quad i = x, y \tag{3-37}$$

where V_{Hi} is the induced voltage across the terminals of the ***H***-coil on the axis, μ_0 the permeability of air and K_{Hi} the coil coefficient, which is determined by calibrating a solenoid as shown in Figure 3-6, where A is the frame, B is the ***H*** coils to be calibrated, C is the Gauss meter probe, D is the connector for outputting the coil terminal voltage signals, E is the turn table for placing the coils and F and G are the wheel rubber bands for adjusting the coil orientation.

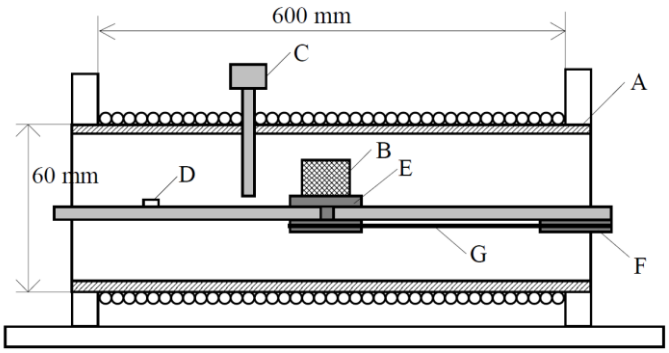

Figure 3-6 Solenoid for calibrating ***H*** sensing coils.

It should be noted that this tester can also be used to measure the 1D alternating magnetic properties. When only the X-axis or Y-axis excitation current is applied, the ***H*** and ***B*** vectors are constrained in the X or Y direction, and the measured ***B-H*** relation would be the traditional ***B-H*** hysteresis loops.

The measurement of rotational magnetic properties is mainly conducted under the so-called circularly rotating magnetization, i.e., the excitation currents of the X- and Y- axes are controlled to form a rotating flux density vector of constant magnitude and speed. Sometimes, measurements under elliptically rotating magnetization are also carried out, e.g., with different ratios of the minor-axis to major-axis magnitudes of flux density. The magnetic properties are usually measured with various frequencies and various maximum flux densities.

After the flux density and field strength of the sample are measured, the total core loss P_t can therefore be calculated with Poynting's theorem:

$$P_t = \frac{1}{T\rho_m}\int_0^T \mathbf{H}\frac{d\mathbf{B}}{dt}dt = \frac{1}{T\rho_m}\int_0^T (H_x\frac{dB_x}{dt} + H_y\frac{dB_y}{dt})dt \tag{3-38}$$

where ρ_m is the mass density of the sample material, T is the time period and H_x, H_y, B_x and B_y are, respectively, the X and Y components of ***H*** and ***B***.

Moreover, led by J. Zhu, the UTS Magnetic Testing Group developed the world-first 3D magnetic testing system in 2001, as illustrated in Figure 3-7 [153]. A photo of the 3D magnetic property tester is shown in Figure 3-8.

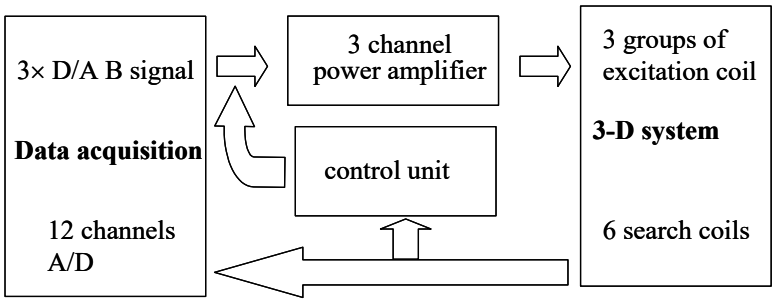

(a)

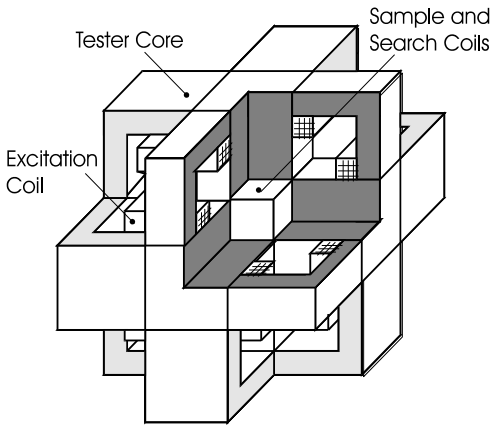

(b)

Figure 3-7 3D Vectorial magnetic property measurement system: (a) block diagram, and (b) structure of 3D view.

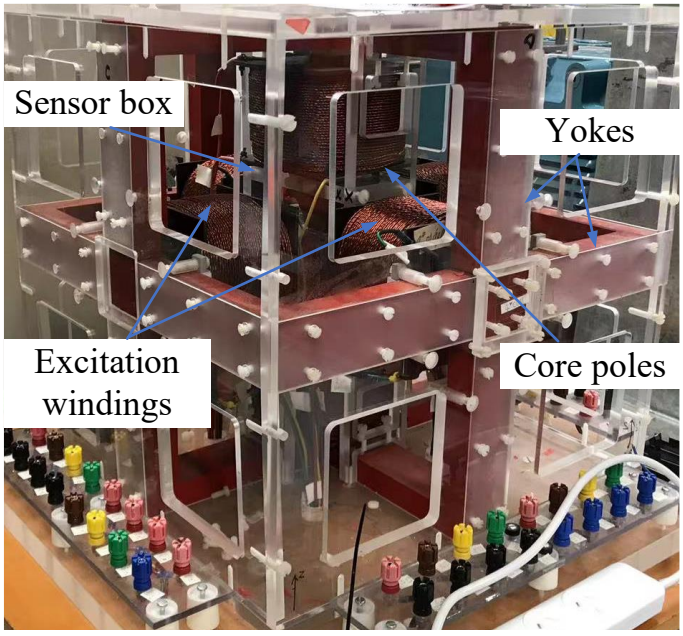

Figure 3-8 A photo of the 3D vectorial magnetic property measurement system.

The measurement system consists of a 3D magnetic property tester, a computer data acquisition and control system, and a 3-channel power amplifier. Three pairs of excitation windings wound around the six yokes of the tester are used to produce 3D magnetic flux in the material sample, which is located in the tester center. By controlling the magnetic excitations in three axes, i.e., the magnitudes and phase angles of excitation currents, the tester is capable of producing various flux patterns, such as 1D alternating in any specified orientation, 2D circularly or elliptically rotating in a plane tilted for a specified angle from an axis and rotating in a 3D pattern with the loci of the ***B*** vector tip forming a specified surface, according to the measurement requirement [154]–[157]. As seen in Figure 3-7 and Figure 3-8, a sample of the testing material is put in the middle of the testing system, in which a 3D vectorial magnetization is generated by the currents passing the three excitation coils.

The magnetic flux density (***B***) and magnetic field strength (***H***) sensing coils are employed to measure the ***B*** and ***H*** components at three axes. As shown in Figure 3-9, on each surface there are two ***H*** coils for measuring the two ***H*** components tangential to the surface, and for each axis four coils are connected in series. Three ***B*** coils are wrapped around the sample for measuring the ***B*** components along three axes.

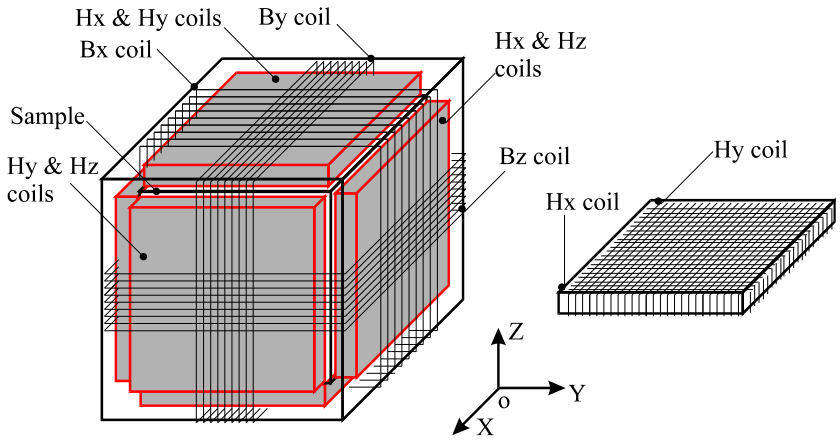

Figure 3-9 A cubic material sample with ***B*** and ***H*** sensing coils.

By measuring the induced electromotive force of the sensing coils, the ***B*** and ***H*** components along each axis can be worked out by:

$$B_i = \frac{1}{K_{B_i}} \int V_{B_i} dt \tag{3-39}$$

$$H_i = \frac{1}{\mu_0 K_{H_i}} \int V_{H_i} dt \tag{3-40}$$

where $i = x, y, z$, K_{Bi} and K_{Hi} are respectively the constants of the ***B*** and ***H*** coils, and the coefficients are determined by calibration [158].

When the ***B*** and ***H*** values have been obtained, the sample core loss P_t in W/kg can be computed according to Poynting's theorem by:

$$P_t = \frac{1}{T\rho_m} \int_0^T \mathbf{H} \cdot \frac{d\mathbf{B}}{dt} dt = \frac{1}{T\rho_m} \int_0^T \left(H_x \frac{dB_x}{dt} + H_y \frac{dB_y}{dt} + H_z \frac{dB_z}{dt} \right) dt \tag{3-41}$$

where $T = 1/f$ is the excitation period, f is the excitation frequency, and ρ_m is the mass density of the sample material.

The prediction of ***B*** from ***H*** or vice versa is necessary for magnetic field analysis of electrical machines. Michelakis *et al*. proposed a 3D moving vectorial Preisach-type model of hysteresis for magnetic material composed of uniaxial interacting particles [159]. Zhong *et al*. presented a 3D vector magnetization model based on the 3D Stoner–Wohlfarth element operator, in which a phenomenological mean-field approximation was used to consider the magnetic interactions among particles [160]. Cardelli *et al*. extended their study on 2D vector hysteresis operator to a 3D case [161]. Li *et al*. presented a 3D magnetic hysteresis model based on a 3D operator according to the minimum energy principle of a stable magnetization state [162].

The term of magnetic reluctivity or permeability is usually applied to relate the $\boldsymbol{B}$ and $\boldsymbol{H}$. For 1D alternating magnetic field, the $\boldsymbol{B}$ and $\boldsymbol{H}$ are in the same direction and the constitutive equation can be expressed as:

$$\mathbf{H} = \nu\mathbf{B} \tag{3-42}$$

The reluctivity v is a scalar and its value may vary with the change of $\boldsymbol{B}$, which is called magnetic nonlinearity. For 2D or 3D rotational magnetization, the reluctivity becomes a full 2D or 3D tensor [163]-[164], and the constitutive equation is,

$$H_i = \sum_j \nu_{ij} B_j \tag{3-43}$$

where v_{ij} is the reluctivity tensor, $i,j = x,y,z$ in Cartesian coordinates, or r,θ,z in cylindrical coordinates.

The nine elements in the tensor can be obtained by a few measurements under 3D or quasi-3D magnetizations [163]. Then they can be used to solve the 3D magnetic field distribution in electrical machines [165].

3.3.4 Correlation Analysis

In order to simplify the fitting process of iron loss coefficients, the Pearson correlation analysis method is employed to analyze the relationship between iron loss coefficients and multiphysics factors. The Pearson correlation coefficient R_{XY} is defined as:

$$R_{XY} = \frac{\sum_{i=1}^{n}\left(X_i - \bar{\mathbf{X}}\right)(Y_i - \bar{\mathbf{Y}})}{\sqrt{\sum_{i=1}^{n}(X_i - \bar{\mathbf{X}})^2}\sqrt{\sum_{i=1}^{n}(Y_i - \bar{\mathbf{Y}})^2}} \tag{3-44}$$

where $\boldsymbol{X}=\{X_i;\ i=1,\cdots N\}$ is the set of input variables, $\boldsymbol{Y}=\{Y_i;\ i=1,\cdots N\}$ the set of corresponding output variables, and $\bar{\boldsymbol{X}}$ and $\bar{\boldsymbol{Y}}$ are the means of $\boldsymbol{X}$ and $\boldsymbol{Y}$, respectively.

Moreover, the closer R_{XY} is to 1, the stronger the correlation between the input and output variables. By taking advantage of the FEM data, the Pearson correlation coefficients between the iron loss coefficients, K_h and K_e, and the multiphysics factors at different operating speeds (from 500 rpm to 5500 rpm) are obtained, as shown in Figure 3-10.

It can be concluded that the hysteresis loss coefficient has a strong relationship with the stress, while the eddy current loss coefficient significantly depends on the temperature. Finally, the proposed iron loss model considering the coupling effects of multiphysics factors can be summarized as:

$$\begin{aligned} P_{iron\_2} = & \left(\frac{k_{h\_PWM}^{T} K_h(\sigma) \omega_s}{2\pi} B_{Tm}^{\alpha} + 8K_e(T_{\circ C}) N_R N_S \left(\frac{B_{Tm}}{T}\right)^2 \right) V_T \\ & + \left\{ \frac{k_{h\_PWM}^{Y} K_h(\sigma) \omega_s}{2\pi} B_{Lm}^{\alpha} + \frac{4K_e(T_{\circ C}) \omega_s (2 + \beta C_N N_S)}{\pi T \beta} B_{Lm}^{2} \right\} V_Y \\ & + \left\{ \frac{K_e(T_{\circ C})}{(N_W S)^2} \sum_{i=3,5,7\ldots}^{n} \left(\frac{V_n}{2\pi}\right)^2 \right\} (V_T + V_Y) \end{aligned} \tag{3-45}$$

where $K_h(\sigma)$ and $K_e(T_{\circ C})$ can be acquired by fitting the iron loss curves.

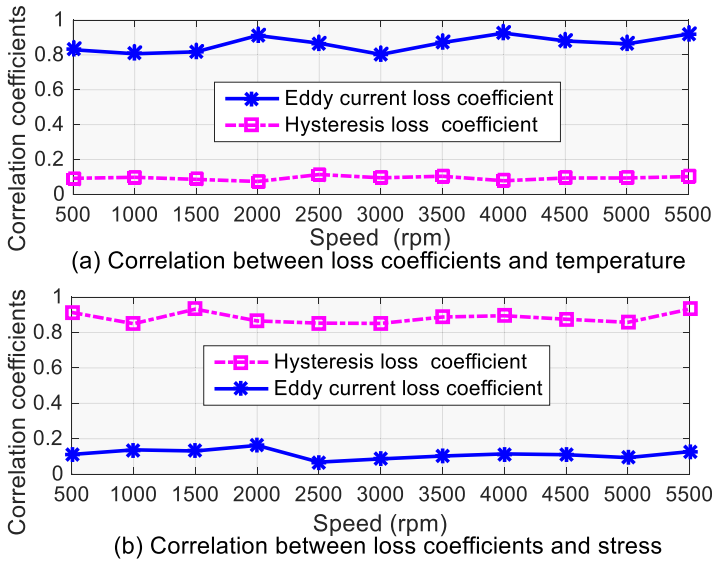

Figure 3-10 Correlations between K_h and K_e with temperature and stress.

3.4 Simulation Validations

An IPMSM prototype for driving EVs is tested to verify the proposed iron loss predictive model. The specifications are listed in Table I. Moreover, the prototype is also simulated by a 2D time-stepping FEM in ANSYS, as shown in Figure 3-11.

TABLE I Specifications of the IPMSM Used in EVs

Items	Values	Items	Values
No. of poles	8	Core material	35WW360
No. of slots	48	Core length	108 mm
No. of phases	3	Stator outer diameter	196 mm
Magnets per pole	2	Stator inner diameter	135 mm
Rated power	20 kW	Rotor outer diameter	134 mm
Rated speed	3600 rpm	Air-gap length	0.5 mm
Maximum power	40 kW	Tooth width	6.35 mm
Maximum speed	5500 rpm	Magnet width	19.5 mm
Rated torque	53 Nm	V-shaped angle	145°
Maximum torque	180 Nm	Phase resistance	0.0052 Ω

3.4.1 Effects of Harmonics

For the inverter-fed IPMSM, there are various harmonic components in the output voltage of PWM inverter [166]. However, the voltage or voltage harmonics would not directly generate the iron loss that is caused by the changing of magnetic flux density, since the magnetic field is generated by current according to Ampere's Law [167]. In this case, when the motor is driven at 3000 rpm under load condition, the output current waveform of inverter is obtained. Figure 3-12 shows the carrier harmonic characteristics with the developed SPWM strategy based on sampling method [167]. As shown, the current waveform mainly contains the 5^{th}, 7^{th}, 11^{th}, 13^{th} and 19^{th} harmonics, which are more than 10% of the fundamental component.

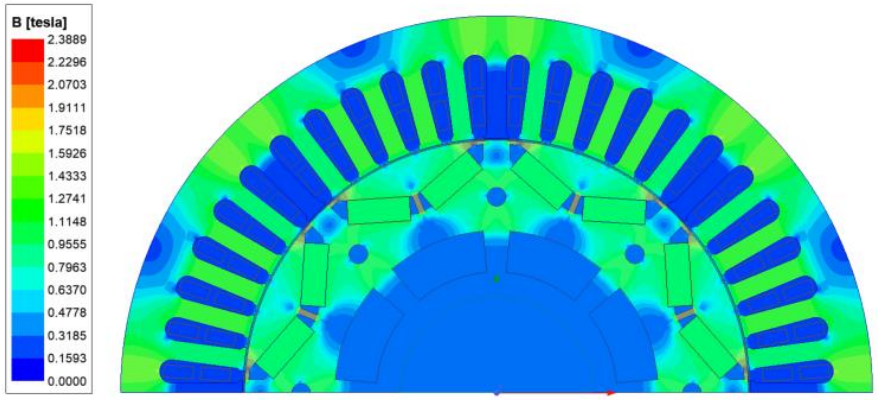

Figure 3-11 2D FEM model of the IPMSM.

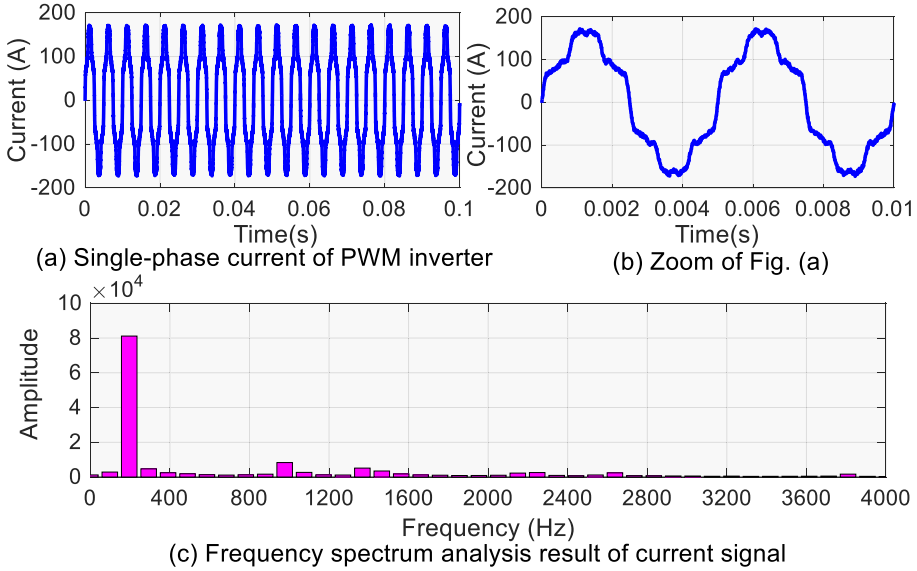

Figure 3-12 Output current waveform of PWM inverter.

In order to show the harmonic effects during iron loss calculation, the air-gap flux density waveforms with PWM current input are also obtained by taking advantage of the established 2D time-stepping FEA model, as shown in Figure 3-13. The magnitudes of the fundamental component and individual harmonics are calculated by using the discrete Fourier transform method, and the combined simulations of Simplorer and ANSYS can be utilized to obtain the airgap flux density with the sinusoidal and PWM supplies. As seen from Figure 3-13, because of the current harmonics, the flux waveforms are distorted significantly. Figure 3-14 gives the framework of the combined simulation model of Simplorer and ANSYS. It is worth mentioning that the magnetic field finite element analysis is conducted with the excitations of both the stator currents and rotor magnets.

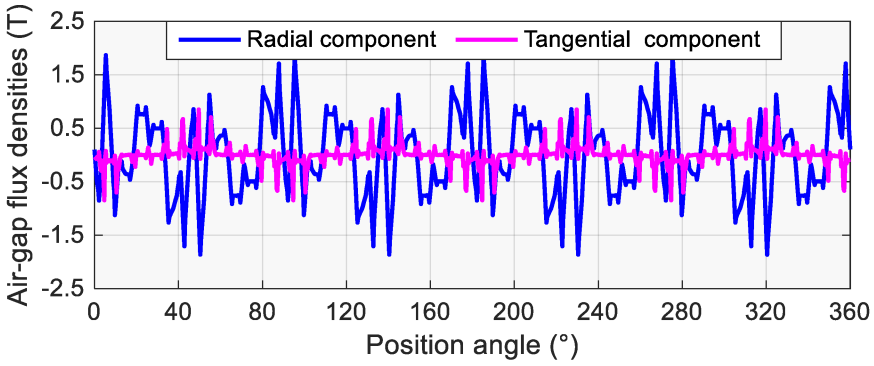

Figure 3-13 Predicted air-gap flux density waveforms.

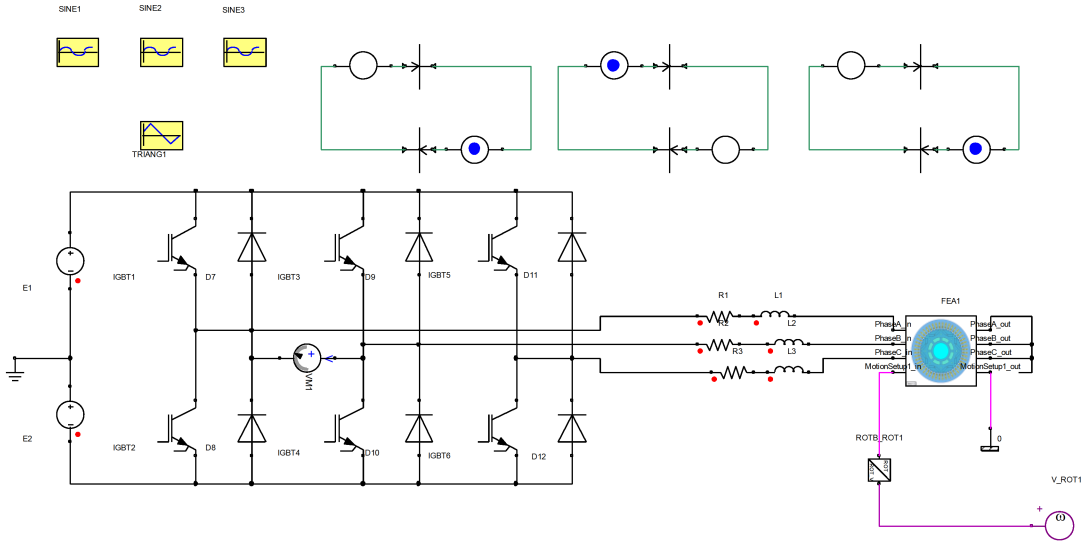

Figure 3-14 Framework of the combined simulation model of Simplorer and ANSYS.

3.4.2 Effects of Multiphysics Factors

Apart from the PWM harmonics, the temperature and stress field distributions of the stator in the IPMSM prototype are also analyzed via FEM. To estimate the temperature distribution, it is assumed that there is no heat exchange between stator and rotor while the mechanical compressive stress in the stator is calculated based on the theory of thick-walled cylinders of elastic mechanics [168]. The FEM maps of temperature and stress field distributions at rated operating point are illustrated in Figure 3-15. It can be seen that the maximum temperature happens at the top of the tooth region and reaches 89 °C, while the maximum stress exists at the bottom of stator slot and can be up to 90 MPa. The average temperature of the stator is about 60 °C and the average stress is around 50 Mpa. In order to precisely predict the iron loss of electrical motors based on the proposed

approaches, the data of the silicon steel sheets loss under different working conditions are measured by using the monolithic measurement method in the built 2-D magnetic property testing system, then utilized to calculate the loss coefficients at different working points (speed range of 500-5500 rpm with the interval of 500 rpm, temperature range of 30-100 ℃ with the interval of 10 ℃, stress range of 20-90 MPa with the interval of 10 MPa) through the Lsqcurve fit in Matlab software. Finally, when the stress values are determined, the 3D maps of loss coefficients shown in Figures 3-16 (a) and (b) can be obtained with the measured data under different working speeds and temperatures. When the temperature values are determined, the 3D maps of loss coefficients under different working speeds and stresses shown in Figures 3-16 (c) and (d) can also be fitted.

The predicted loss coefficients, considering the coupling effects of multiphysics factors, can thus be substituted into (3-45) for iron loss calculation. As shown, when the temperature increases, the eddy current loss coefficient decreases significantly (about 35%) while the hysteresis loss coefficient varies slightly (only around 2%). Meanwhile, K_h increases by 15% with the increase of stress, while K_e varies by only 1% with respect to the stress.

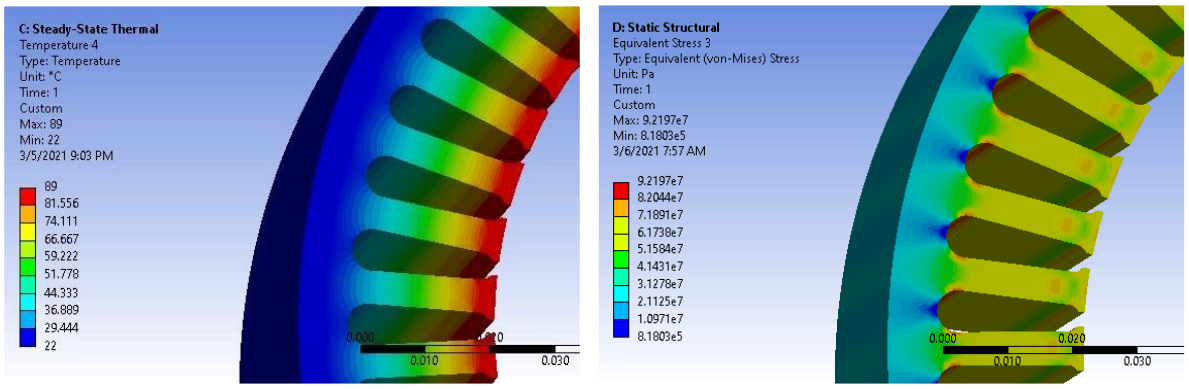

(a) Temperature field distributions of stator

(b) Stress field distributions of stator

Figure 3-15 FEM maps of temperature and stress field distributions.

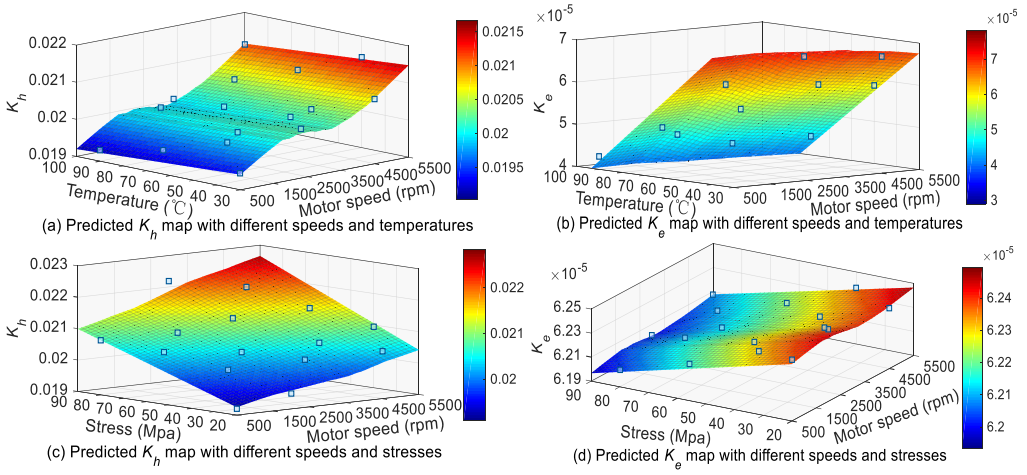

Figure 3-16 Predicted 3D maps of loss coefficients.

3.5 Experiment Comparison

The prototype stator and rotor structures, as well as the setup and operating principles of the integrated experimental platform, are illustrated in Figure 3-17. The control and measuring equipment including the control and drive circuits, the dynamometer, and the dynamic torque/speed sensors are mounted on the counter-towing experimental platform. Besides, a DC power supply is utilized for providing the desired DC power to the test motor, an upper computer is used for writing the control program, an electrical control cabinet is employed to collect speed & torque data and simulate different load conditions, while an oscilloscope is applied for the data recording.

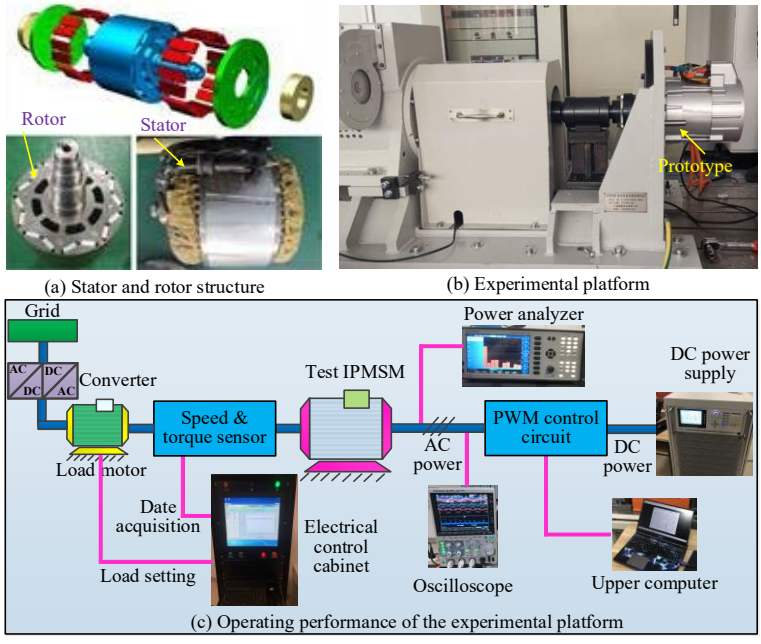

Figure 3-17 Setup and operating principles of the integrated experimental platform.

3.5.1 No-load Condition

To verify the superiority in the prediction accuracy and the computational burden of the proposed iron loss analytical model, the iron loss of the IPMSM prototype under no-load condition is predicted by using the proposed model, then compared with the values obtained by the Bertotti separation analytical model and numerical FEM. In the calculation, $\alpha = 2$ and $C_N = 0.41$ hold. Meanwhile, for better comparison, the magnetic-effect, temperature-effect, and stress-effect on the loss coefficients are considered in both the proposed model and the numerical FEM, while these factors were not given into considerations in the Bertotti model to show the original improvement of the proposed models.

Three conditions are set for case studies, namely, 'case (i): the temperature is fixed at 30 ℃, and stress at 90 MPa, case (ii): the temperature is fixed at 30 ℃, and stress at 20 MPa, and case (iii): the temperature is fixed at 100 ℃, and stress at 20 MPa'. Figure 3-18 to Figure 3-20 illustrate the iron losses obtained by the three models at different motor speeds in the range of 500 - 5500 rpm, under the operating conditions of cases (i), (ii) and (iii), respectively. Since the speed ripples are relatively small, more attentions are paid to the iron loss performance under static operating state and the speed harmonics or ripples are neglected in the case studies. As seen from Figure 3-18 to Figure 3-20, the stator iron loss has a significant upward increase along with the speed increase. Meanwhile, the temperature rise and mechanical stress have non-ignorable impacts on the iron loss, which would be fully analyzed later.

The error analysis between the analytical models and FEM, corresponding to Figure 3-18 to Figure 3-20, is presented in Table II, where EM_i and EA_i (i = 18, 19, 20) represent the maximum and absolute average errors of iron losses which are relative to Figures 3-18, 3-19 and 3-20, respectively.

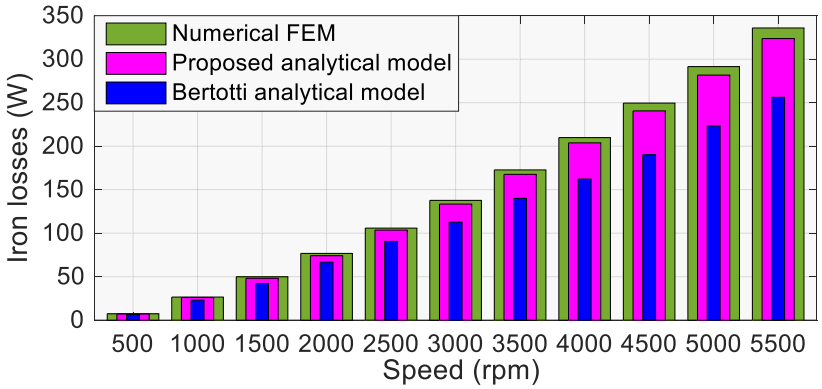

Figure 3-18 Comparative results of iron losses under case (i).

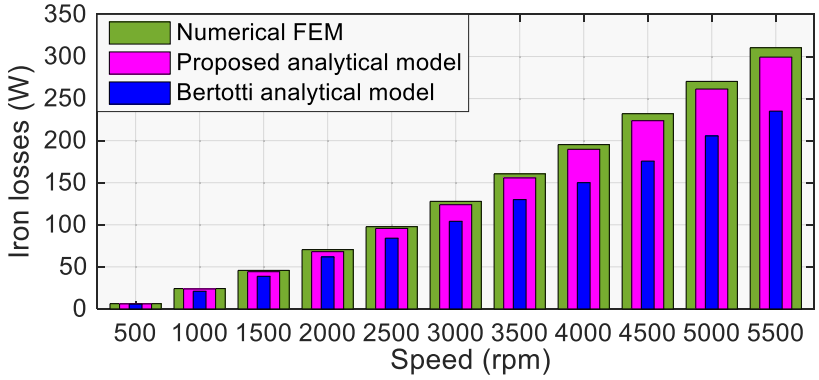

Figure 3-19 Comparative results of iron losses under case (ii).

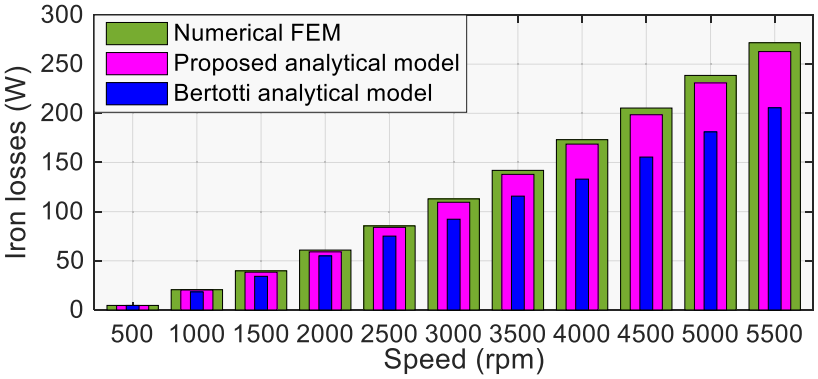

Figure 3-20 Comparative results of iron losses under case (iii).

TABLE II Error Analysis of Figures. 3-18, 3-19 and 3-20

Items	EM_{11}	EA_{11}	EM_{12}	EA_{12}	EM_{13}	EA_{13}
Bertotti	23.68%	17.90%	24.27%	17.85%	24.34%	16.35%
Proposed	3.53%	2.95%	3.59%	3.03%	3.30%	2.73%

As shown, under different working modes, the maximum errors between the iron loss calculated by the proposed approach and the values obtained by FEM are 3.53%, 3.59% and 3.30% for cases (i), (ii) and (iii), respectively, while the absolute average errors are all within 3.03% in spite of the effects of temperature and stress. For Bertotti method, the maximum errors exceed 23.68% and the absolute average errors are all greater than 16.35%. Moreover, the proposed method took only a few minutes for iron loss calculation, while the FEM required about 56 minutes. The results illustrate very well the superior performance of the proposed models in accuracy and conciseness of iron loss prediction with no-load condition.

3.5.2 Load Condition

Although the results under no-load condition indicate that the proposed model is efficient for the iron loss prediction of IPMSMs, the PWM carrier harmonics are not fully considered. For better verification, the measured iron losses of the prototype are compared with those predicted by the FEM, the method considering PWM and slotting harmonics [169], and the proposed model in terms of different input phase currents of 64 A, 180 A, 285 A and 588 A with the average temperature and stress. The PWM effects are considered in all the prediction methods, while the coupling effects of temperature and stress on the loss coefficients are only involved in the proposed methods to clearly verify the contributions of this work. Taking advantage of the simple structure, fast dynamic response and strong robustness, the FOC strategy [170] is used to carry out the experiments, aiming to achieve the maximum torque per ampere. It is worth mentioning that the iron loss of the prototype cannot be measured directly with the experimental platform. The IPMSM mainly contains four kinds of losses, i.e. the iron loss, copper loss, mechanical loss and stray loss. The copper loss can be calculated based on the phase current and winding resistance. The mechanical losses are determined through a so-called dummy rotor method which was successfully employed in our publication [171]. In this scheme, the motor rotor is replaced by a wooden rotor with a similar shape as the real rotor. Assuming that the mechanical losses with the two rotors are the same under the same speed, then the mechanical loss of the test motor at various speeds can be obtained

as the input power of the drive motor since there is no magnetic field, induced voltage and current in the stator, i.e. no iron loss or copper loss. The stray loss is empirically assumed to be 1% of the output power. Thus, the iron loss of the prototype can be calculated by:

$$P_{ironM} = P_{inputM} - P_{copperM} - P_{mechM} - P_{outputM} - P_{strayM} \tag{3-46}$$

where P_{totalM} and $P_{outputM}$ are the measured input and output powers, while $P_{copperM}$, P_{mechM} and P_{strayM} are the derived copper loss, mechanical loss and stray loss based on the experimental data.

To make the mechanical loss data more convincing, we carried out experiments to measure the mechanical losses at any speed for three times, and determined the mechanical losses by the means. Figure 3-21 shows the measured mechanical loss curve with motor speeds. Then, the comparative experimental results are obtained with (3-46) and illustrated in Figure 3-22. The error analysis between the measured iron losses and the predicted values is presented in Table III, where EM_j and EA_j (j = 64, 180, 285 and 588) represent the maximum and absolute average errors of iron loss which are relative to those measured by the experimental platform under 64 A, 180 A, 285 A and 588 A phase currents, respectively.

As shown in Table III, with different phase current inputs, the maximum and absolute average errors of the measured iron losses and the values calculated by the proposed model are less than 5.85% and 4.71%, respectively, which are around 45% of the errors for the numerical FEM. The computational times are also much shorter. Although the method in [169] takes little computational time as the propose models, the maximum and absolute average errors compared with the measured values are bigger by 11.62% and 11.41%, respectively, regardless of the current inputs. Owing to the loss separation error and the unaccountable influence of temperature and stress, there is a deviation of about 10% between the iron losses obtained by the FEM and experiment measurement. Moreover, taking advantage of considering the multiphysics factors, especially the PWM harmonics, the proposed model has better prediction accuracy than FEM. All the results show the satisfactory performances of the proposed iron loss model under load conditions. The visible relationships between these multiphysics factors and the final iron loss are also revealed through the improved iron loss prediction model.

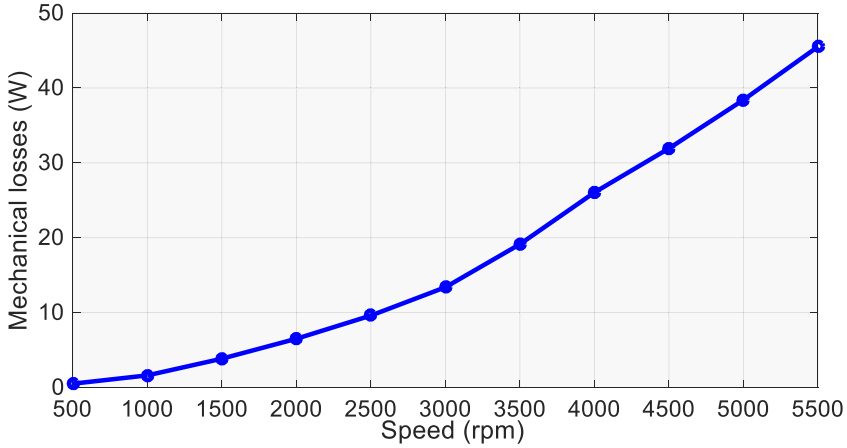

Figure 3-21 Measurement results of mechanical losses.

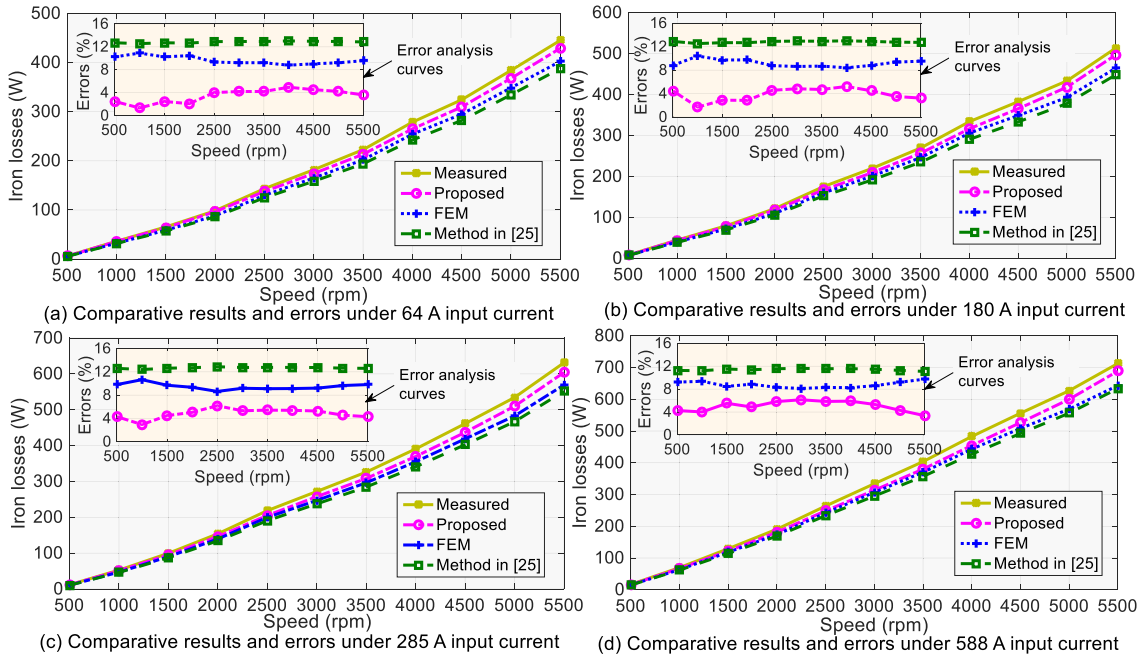

Figure 3-22 Comparative results of iron losses under different speeds and phase current conditions.

TABLE III Data Analysis of Figure 3-21

Items	FEM	Proposed	Method in [169]	Items	FEM	Proposed	Method in [169]
EM_{64}	10.91%	4.95%	13.03%	EM_{285}	10.66%	5.39%	12.87%
EA_{64}	9.61%	3.56%	12.84%	EA_{285}	9.44%	3.89%	12.68%
EM_{180}	10.39%	5.22%	12.99%	EM_{588}	9.37%	5.85%	11.62%
EA_{180}	9.21%	3.80%	12.81%	EA_{588}	8.72%	4.71%	11.41%

3.5.3 Various Conditions

In order to illustrate the coupling effects of multiphysics factors, the control variable method is utilized for analyzing the single temperature-effect, and stress-effect on the final iron loss value of the IPMSM. Based on the verifications outlined above, the iron losses under varying temperatures and stresses are calculated by using the proposed model and given in Figure 3-23. The current is fixed at 180 A and motor speed at 3000 rpm.

As shown, the iron loss decreases by a range of 15.20% when the temperature increases from 30 ℃ to 100 ℃, while the iron loss value increases by 10.03% with the expansion of stress from 20 MPa to 90 MPa. Results indicates that the loss coefficients are not only affected by the frequency but also strongly related to the temperature rise and mechanical stress.

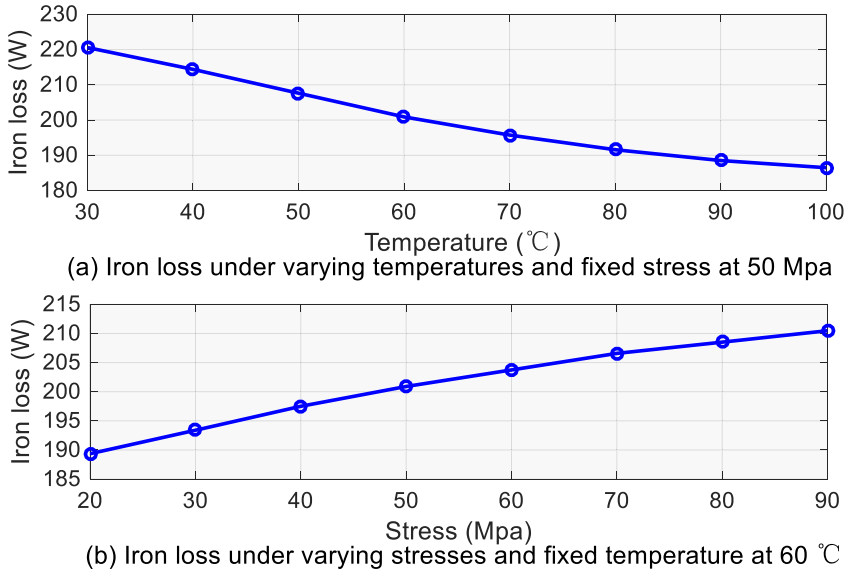

Figure 3-23 Iron losses under varying temperatures and stresses.

3.6 Conclusion

Aiming at the coupling effects of multiphysics factors, an improved iron loss prediction model for IPMSMs, used in EVs, is proposed, which accounts for the slotting harmonics, PWM harmonics, temperature and stress influences. The accuracy and superiority of the proposed model is verified by comparing its results with the results obtained by

experimental testing, FEM, and the Bertotti methods on an IPMSM prototype. The main conclusions are as follows.

i) The proposed model has good performance for iron loss prediction. Under no-load conditions, a comparison with the FEM results shows that the maximum and absolute average errors are less than 3.59% and 3.03%, respectively, in the case of varying motor operating speeds, temperatures and stresses. Under load conditions, the comparison between the iron loss results of experimental measurement and theoretical prediction by the proposed model also shows a very small error that accounts for only 45% of the errors for the numerical FEM. Moreover, the computational cost can also be greatly reduced.

ii) The iron loss is affected by the slotting harmonics, PWM carrier harmonics, temperature rise, and mechanical stress. Specifically, the eddy current loss coefficient is mainly related to the thermal field, and the hysteresis loss coefficient has a strong dependency on the stress field. Furthermore, the iron loss increases when the stress increases, while the iron loss reduces when the temperature rises.

The results of this work may provide useful references for not only the accurate iron loss prediction but also multiphysics design optimization of PM motors. Future works including the validation works of different types of PM motors under extreme working conditions can be conducted to improve the proposed iron loss prediction model in adaptability.

Chapter 4

Improved ECM-Based Loss Minimization Control Method

4.1 Introduction

Recent work has highlighted the strong interdependencies among components in electric drive systems and the advantages of optimizing the system as a whole, encompassing both the motor and controller [172]. Therefore, identifying optimal parameters for the entire system, rather than separately optimizing the motor and controller and then assembling them into their respective applications, holds great significance. The design optimization of EV drive systems at system level typically involves two main parts, namely, the design analysis and the performance optimization [173]. For the design analysis, accurate loss calculation is crucial in efficiency optimization. Researchers have also conducted substantive works on the efficiency optimizations of various types of electric machines and drives [174]. However, the loss models in these achievements only include two main electromagnetic losses, i.e., motor core loss and copper loss, without enough consideration of the losses aroused by the control system, resulting in restrictions on system efficiency improvements.

More specifically, for the motor side, the computation of core losses can be rather intricate and challenging, primarily due to the nonlinear characteristics of core materials and the complex magnetic field distributions [175]. The use of the Bertotti model in FEA has proven effective for accurately calculating core loss [176]. However, FEA is time-consuming, particularly in the iterative design optimization of PMSMs with complex structures [177]. Recently, to lower computational expenses, alternative methods for calculating core loss based on analytical models have been suggested [178]-[179]. Among them, the ECM enables engineers to streamline motor design and optimization. By fine-tuning the parameters, the ECM can consider multiple factors influencing core losses and accelerate the design process [180]. However, to the authors' knowledge, in the

conventional ECMs for PMSMs [181], the omission of core loss leads to considerable calculation inaccuracies, limiting its applicability in high-speed and high-torque/power-density PMSMs. While some researchers, such as Hu *et al*. [182] and Ito *et al*. [183] have attempted core loss modelling within the ECMs, modern PMSMs are extensively employed in variable-speed scenarios, and the single-valued equivalent core loss resistance model cannot accurately predict core loss across a wide range of speeds and loads. Furthermore, the existing ECM structural configurations face challenges in faithfully simulating the rotational magnetization behaviours of core materials.

For the controller part, numerous control methods, including FOC [184], DTC [185], and MPC [186], have been developed and optimized at the controller level. However, they have seldom been integrated with motor design optimization, such that the desired overall system performance and efficiency cannot be guaranteed. Given the widespread applications of electric drive systems, with over half of globally generated electricity used for motor operations, energy saving and efficiency optimization control are effective methods to enhance motor drivers' efficiency, in addition to optimizing motor structural design. Efficiency optimization control methods for PMSMs can be typically categorized into three types, i.e. maximum torque per ampere (MTPA) control, online search control with minimum input power, and model-based loss minimization control [187].

Among them, the online search control method exhibits strong robustness and adaptability to variations in motor parameters. However, because of the real-time computation of electrical losses combined with the iterative optimization process, this method can lead to a substantial computational burden due to exhaustive exploration [188]. When motors operate at relatively low speeds and the copper loss dominates the whole losses, the MTPA strategy becomes a good option for efficiency optimization. It minimizes copper losses by optimizing the *d*-axis and *q*-axis currents, with the operating point nearest to the maximum torque value. Therefore, in the synchronous reference frame, at the MTPA point, the derivative of torque with respect to the load angle should be derived as (4-1).

$$\delta_{MTPA} = \cos^{-1}\left(\frac{-\psi_{PM} + \sqrt{\psi_{PM}^2 + 8(L_d - L_q)^2 \left|i_s^2\right|}}{4(L_d - L_q)|i_s|}\right) \tag{4-1}$$

where

$$\begin{cases} i_{d-MTPA} = i_s \cos(\delta_{MTPA}) \\ i_{q-MTPA} = i_s \sin(\delta_{MTPA}) \end{cases} \tag{4-2}$$

For describing copper losses in terms of stator currents, we can make (4-1) equal zero to find the stator current references that achieve the minimum copper loss. Namely, the specific *d*-axis and *q*-axis current references can be obtained for a given torque, thereby minimizing copper loss. But the MTPA method holds the drawback in direct neglect of iron loss, thereby it is only preferable to design a control method that is less sensitive to the accuracy of iron loss measurements [189].

The principle of model-based loss minimization control involves integrating equivalent iron loss resistances into the PMSM's equivalent circuits. By minimizing both copper and iron losses, the optimal *d*-axis current can be obtained. This method can achieve globally optimal efficiency and offer advantages such as smooth control and fast response, which has been applied to the efficiency optimization control of PMSMs in various industrial fields. As is well known, to implement the model-based loss minimization control, an accurate loss model is very critical. However, the loss models in most existing achievements only include two main electromagnetic losses, i.e., motor iron loss and copper loss, without giving enough consideration of the losses associated with the inverter, while the iron loss model is not sufficient, resulting in restrictions on system efficiency improvements.

In summary, loss minimization control based on mathematical models, in addition to motor topology optimization, is a highly effective method to enhance the drives' efficiency. It considers multiple types of losses, in contrast to the MTPA method, which only addresses copper loss. Moreover, it is more computationally efficient, without the need for convergence requirements, making it readily implementable in controllers without additional hardware demands [190]. However, most mathematical models for loss control in PMSMs may not fully address core losses or control-related losses.

This chapter aims to present an improved ECM-based loss minimization control considering the losses in both motor and control units, which is integrated into the scheme for not only simplifying optimization process, but also better-ensuring efficiency improvement. Moreover, rather than focusing on individual components, this work takes a comprehensive view of the entire system, allowing full concern of complex interactions

between motor and controller, ensuring that all elements work in synergy to achieve enhanced overall system performance. Specifically, a generalized equivalent circuit model with a novel topology that considers rotating magnetization effects is first proposed to accurately predict the core loss of PMSMs under both no-load and loaded conditions. The improved model with updated topology incorporates variable equivalent resistances for hysteresis, eddy current and anomalous losses, together. Moreover, based on the proposed ECM, a system-level loss model of the PMSM drive system is established for the loss minimization control and thus the optimization scheme, where high-order formulas and radical calculations can be iteratively solved online by a numerical approach.

4.2 System-Level Loss Model

Efficiency/loss, regarded as a pivotal factor, holds significant influences on optimal solutions and demands precise modelling. Considering that the electrical loss of control units also plays a decisive role in system efficiency, the system-level loss model for a specific PMSM drive system is formulated as follows.

$$P_{total} = P_{Cu} + P_{Fe} + P_{Inv} \tag{4-3}$$

where P_{Cu}, P_{Fe}, and P_{Inv} are the motor copper loss, motor core loss and inverter loss, respectively.

The losses in a PMSM can be categorized as copper, core loss, mechanical, and additional losses. Among them, the non-dominant mechanical and additional losses are both very small relative to the total motor loss and they are difficult to measure and control [173]. Thus, only controllable electromagnetic losses (core and copper losses) are considered. For the control side, electrical losses in control units such as detection and control circuits, as well as the inverter, also impact system efficiency to some extent. For most common applications, like EVs, the losses in sensors and control circuits are negligible [177], and therefore P_{inv} is primarily considered in this work.

ECM is an important tool used by engineers to understand and analyze the electrical characteristics of PMSMs. In traditional ECMs, the magnetic properties of the iron core are often overlooked [191]. However, in real-world applications, devices experience various losses, including iron losses which generate heat and thus affect overall efficiency and reliability. Thus, in our improved ECM, the iron loss resistances were incorporated,

aiming to provide a more accurate mapping of device behaviors under actual operating conditions.

In this study, an improved ECM is proposed for PMSMs. As shown in Figure 4-1, the upgraded model incorporates three variable equivalent resistances (R_{an}, R_e, R_h) in parallel to the back-*emf* in the *q*-axis circuit to separately represent the anomalous loss, eddy current loss, and hysteresis loss. This placement represents core losses induced solely by the PM flux, enabling the resistances to change with frequency for maintaining a precise analysis of core loss components with respect to working speed through parameter identification. Moreover, to describe additional core losses caused by the load current, an equivalent resistor R_i is employed in parallel with the electromotive force in the synchronous reactance induced by the armature currents in *d*- and *q*-axis, through which the PWM high frequency harmonics and the magnetic saturation effects caused by the load currents can all be considered.

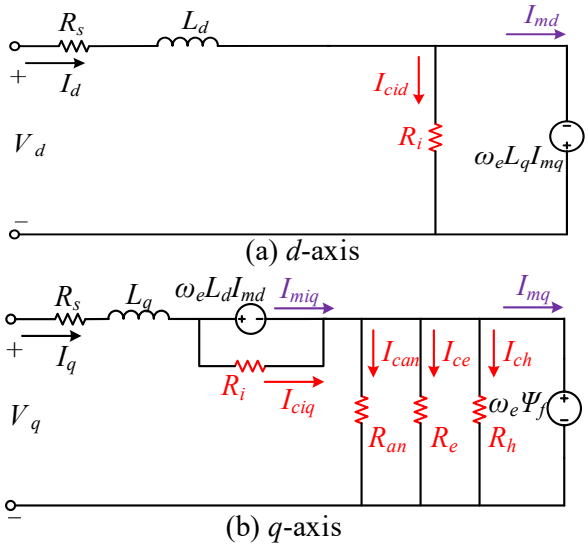

Figure 4-1 Improved equivalent circuit considering core loss resistances.

The proposed ECM model is updated and advanced based on an existing circuit model, introduced by Colby and Novotny [61]. As seen from Figure 2-5, an equivalent resistor was added in parallel with the internal voltage to predict iron losses. As the electromotive force is proportional to the magnetic flux or flux density, the iron losses of the motor can be approximated as proportional to the square of the internal voltage. Thus, the equivalent iron loss resistance can be determined from the no-load iron losses. As the armature current is nearly zero under no-load conditions, the voltage across the resistance equals the back

electromotive force or the terminal voltage. Then, the equivalent iron loss resistance can be obtained by (2-3).

Despite the advantages of this kind of ECM, several issues still exist. For example, due to the rotor saliency, especially in IPMSMs, the *d*-axis inductance is not equal to the *q*-axis inductance [192]. Therefore, it is necessary to employ two equivalent circuits to account for the influence of the difference in *d*- and *q*-axis inductances. Secondly, most ECMs can only analyze the iron losses of PMSMs operating normally at synchronous speed. But in variable speed conditions, a single-valued equivalent resistance model would always fail to accurately reflect and compute iron losses [193]. Moreover, during the steady-state operation of a PMSM with a fixed terminal voltage, the iron losses computed from traditional ECMs typically remain almost constant across various loads, as the stator resistance is generally much smaller compared to the synchronous reactance. However, this contradicts the fact that armature currents may lead to extra iron losses [191].

Meanwhile, it should be noted that iron losses usually consist of three components, namely, hysteresis loss, classical eddy current loss, and anomalous loss. Each component varies differently with magnetic flux density and frequency. Specifically, hysteresis loss varies with the x (x = 1.6-1.9) power of magnetic flux density and linearly with frequency; classical eddy current loss varies with the square of magnetic flux density and frequency; and anomalous eddy current loss varies with the 1.5 power of magnetic flux density and frequency. When using linear equivalent resistors to calculate iron losses, the results typically provide reasonably accurate predictions at low frequencies and small magnetic flux density conditions. But when the motor operates at high speeds and larger stator currents, the magnetization characteristics of the iron core become nonlinear. Additionally, the proportion of classical eddy current loss in total iron losses increases. In such cases, using linear equivalent resistors to calculate motor iron losses may lead to significant errors.

To address these issues, in the proposed ECM, each iron loss component is considered separately, and three equivalent resistors (R_h, R_e, and R_{an}) that can vary with frequency are defined to describe the hysteresis, eddy current, and anomalous losses under no-load conditions, respectively. These resistors are directly connected in parallel to the induced electromotive force in the *q*-axis and represent the iron losses induced solely by the PM flux.

As for load conditions, the load current flows through armature winding, and the magnetic flux within the motor is actually a combined result of the flux generated by the PMs and the

flux generated by the load current. Additionally, due to the magnetic saturation, the total magnetic flux does not increase linearly with the load current. For example, in [193], the load iron loss of a three-phase PM claw-pole motor was calculated by the ECM of Figure 2-5. Assuming that the equivalent resistance R_c is linearly related to speed, (4-4) can be used to compute the load iron loss. It can be seen that as the load or armature current increases, the iron losses increase. However, this formula may significantly overestimate the additional iron losses due to the armature current. In fact, due to magnetic saturation, the total flux does not increase significantly, and the additional iron losses are mainly caused by flux waveform distortion. In this case, to describe the additional iron losses caused by the load current, an equivalent resistor R_i is employed in parallel with the electromotive force in the synchronous reactance induced by the armature current in *d*- and *q*-axis. This resistor is added to carry a portion of the input current that accounts for the additional iron losses caused by the load.

$$P_c = 3\frac{V_x^{\,2}}{R_c} = 3\frac{E^2 + \left(XI_2\right)^2}{R_c} \tag{4-4}$$

The meanings of the variables in (4-4) are explained in Figure 2-5.

According to the proposed ECM, mathematical models are employed to derive equivalent circuit representations of *d*- and *q*-axis voltages and currents.

$$\begin{cases} V_d = (R_s + pL_d)I_d - \omega_e L_q I_{mq} \\ V_q = (R_s + pL_q)I_q + \omega_e L_d I_{md} + \omega_e \psi_f \end{cases} \tag{4-5}$$

and

$$\begin{cases} I_d = I_{cid} + I_{md} \\ I_q = I_{ciq} + I_{miq} = I_{can} + I_{ce} + I_{ch} + I_{mq} \end{cases} \tag{4-6}$$

where V_d and V_q represent the *d*- and *q*-axis terminal voltages, L_d and L_q are the *d*- and *q*-axis inductances. Ψ_f, Ψ_d, and Ψ_q stand for the PM and *d*-axis, *q*-axis flux linkages. R_s is the resistance of armature winding, ω_e the rotor speed in electrical angular frequency, and p the differential operator (=d/dt). I_d and I_q denote the *d*- and *q*-axis armature currents, I_{cid} and I_{ciq} are the *d*- and *q*-axis load core loss currents, I_{md}, I_{miq}, and I_{mq} are the *d*- and *q*-axis magnetizing currents, and I_{can}, I_{ce}, and I_{ch} are the currents flowing through the resistances R_{an}, R_e, and R_h.

The electromagnetic torque T_{em} can be determined by the following equation, where n_p is the number of pole pairs.

$$T_{em} = \frac{3}{2} n_p \left(\psi_d I_q - \psi_q I_d \right) = \frac{3}{2} n_p [\psi_f + (L_d - L_q) I_d] I_q \tag{4-7}$$

Using (4-8), the ECM allows for the estimation of the copper loss P_{Cu}, no-load core loss P_{Fe_N}, and load core loss P_{Fe_L}.

$$\begin{cases} P_{Cu} = \frac{3}{2} R_s (I_d^2 + I_q^2) \\ P_{Fe\_N} = \frac{3}{2} (R_{an} I_{can}^2 + R_e I_{ce}^2 + R_h I_{ch}^2) \\ P_{Fe\_L} = \frac{3}{2} \left[(R_{an} I_{can}^2 + R_e I_{ce}^2 + R_h I_{ch}^2) + R_i (I_{cid}^2 + I_{ciq}^2) \right] \end{cases} \tag{4-8}$$

The inverter is a critical component that converts DC power into AC power to drive the motors. During this process, some losses occur due to the switching operations and current flow in the electronic components. Thus, the inverter losses can usually be calculated with switching loss and conduction loss.

$$P_{Inv} = m_1 I_{rms} + m_2 {I_{rms}}^2 \tag{4-9}$$

where m_1 and m_2 are the inverter loss coefficients that depend on the specific inverter design, topology, and operating conditions. I_{rms} is the magnitude of inverter output current, and,

$$I_{rms} = \sqrt{I_d^2 + I_q^2} \tag{4-10}$$

Then, combining (4-3), (4-8), (4-9) and (4-10), the system-level loss model for a PMSM drive system is obtained as (4-11). Given that the no-load losses can also be calculated using (4-11), this paper focuses solely on presenting the system-level loss model under load conditions.

$$\begin{aligned} P_{total\_L} = {} & \frac{3}{2} R_s (I_d^2 + I_q^2) + \frac{3}{2} (R_{an} I_{can}^2 + R_e I_{ce}^2 + R_h I_{ch}^2) \\ & + \frac{3}{2} R_i (I_{cid}^2 + I_{ciq}^2) + m_1 \sqrt{I_d^2 + I_q^2} + m_2 (I_d^2 + I_q^2) \end{aligned} \tag{4-11}$$

4.3 Loss Minimization Control

Based on (4-11), a revised loss minimization control method is synthesized to improve the drive system efficiency, in which the relationships between T_{em}, I_d and I_q are derived to minimize the system losses. Meanwhile, the currents I_{cid}, I_{ciq}, I_{can}, I_{ce}, and I_{ch} need to be eliminated or replaced for the implementation of loss minimization control.

For eliminating I_{can}, I_{ce} and I_{ch}, based on Figure 4-1 (b), the power loss in R_{an}, R_e and R_h can also be calculated via:

$$\begin{cases} P_{Fe\_N} = \dfrac{3(\omega_e \psi_f)^2}{2} C_{Fe} \\ C_{Fe} = \dfrac{1}{R_{an}} + \dfrac{1}{R_e} + \dfrac{1}{R_h} \end{cases} \tag{4-12}$$

where C_{Fe} donates the equivalent core loss conductance.

Also, according to the circuit principles shown in Figure 4-1, the current equation of (4-6) can be updated as:

$$\begin{cases} I_d = I_{cid} + I_{md} = I_{md} - \dfrac{\omega_e L_q I_{mq}}{R_i} \\ I_q = I_{ciq} + I_{miq} = I_{mq} + C_{Fe} \omega_e \psi_f \end{cases} \tag{4-13}$$

Then, the unknown variables I_{md} and I_{mq} can be derived as:

$$\begin{cases} I_{md} = I_d + \dfrac{\omega_e L_q}{R_i} (I_q - C_{Fe} \omega_e \psi_f) \\ I_{mq} = I_q - C_{Fe} \omega_e \psi_f \end{cases} \tag{4-14}$$

and

$$\begin{cases} I_{cid} = -\dfrac{\omega_e L_q I_{mq}}{R_i} = -\dfrac{\omega_e L_q (I_q - C_{Fe} \omega_e \psi_f)}{R_i} \\ I_{ciq} = \dfrac{\omega_e L_d I_{md}}{R_i} = \dfrac{\omega_e L_d}{R_i} \cdot \left[I_d + \dfrac{\omega_e L_q}{R_i} (I_q - C_{Fe} \omega_e \psi_f) \right] \end{cases} \tag{4-15}$$

In combination with (4-11), (4-12) and (4-15), the system-level loss model with respect to I_d and I_q can thus be calculated via:

$$P_{total\_L}=\frac{3}{2}R_s(I_d^2+I_q^2)+\frac{3(\omega_e\psi_f)^2}{2}C_{Fe}+\frac{3\left[\omega_e L_q(I_q-C_{Fe}\omega_e\psi_f)\right]^2}{2R_i}$$
$$+\frac{3\left[\omega_e L_d R_i I_d+\omega_e^2 L_d L_q(I_q-C_{Fe}\omega_e\psi_f)\right]^2}{2R_i^3}+m_1\sqrt{I_d^2+I_q^2}+m_2(I_d^2+I_q^2) \tag{4-16}$$

To simplify the following calculation, we define,

$$\begin{cases} a_1=\dfrac{3\left[\left(\omega_e L_d\right)^2+R_s R_i\right]}{2R_i};a_2=\dfrac{3\left[R_s R_i^3+\left(\omega_e L_q R_i\right)^2+\left(\omega_e^2 L_d L_q\right)^2\right]}{2R_i^3} \\ a_3=-\dfrac{3C_{Fe}\omega_e\psi_f\left[\left(\omega_e^2 L_d L_q\right)^2+\left(\omega_e L_q R_i\right)^2\right]}{R_i^3} \\ a_4=-\dfrac{3C_{Fe}\psi_f\omega_e^4 L_d^2 L_q}{R_i^2};a_5=\dfrac{3\omega_e^3 L_d^2 L_q}{R_i^2} \\ a_6=\dfrac{3C_{Fe}\omega_e^2\psi_f^2\left[R_i^3+C_{Fe}\left(\omega_e L_q R_i\right)^2+C_{Fe}\left(\omega_e^2 L_d L_q\right)^2\right]}{2R_i^3} \end{cases} \tag{4-17}$$

Then, by substituting (4-7) and (4-17) into (4-16) to eliminate I_q, the system-level loss model of a PMSM drive system considering load loss can be expressed with:

$$P_{total\_L}=(a_1+m_2)I_d^2+(a_2+m_2)\left\{\frac{2T_{em}}{3n_p[\psi_f+(L_d-L_q)I_d]}\right\}^2$$
$$+\frac{2a_3T_{em}}{3n_p[\psi_f+(L_d-L_q)I_d]}+a_4I_d+\frac{2a_5T_{em}I_d}{3n_p[\psi_f+(L_d-L_q)I_d]}$$
$$+m_1\sqrt{I_d^2+\left\{\frac{2T_{em}}{3n_p[\psi_f+(L_d-L_q)I_d]}\right\}^2}+a_6 \tag{4-18}$$

As the loss minimization control of an electric motor is usually targeted towards load rather than no-load conditions in practice, and hence (4-18) is used for the control law derivation. As seen, the total power loss is a function related to I_d, ω_e and T_{em}, with known parameters like inductances, resistances, PM flux linkage, and number of pole pairs. During steady-state operation, the losses in PMSMs mainly arise from resistance and core losses. By employing a good control strategy, it is possible to minimize these losses and achieve high efficiency in practical applications. During transient operations, like start-up, acceleration, deceleration, or sudden load changes, the motor parameters experience instantaneous variations. In such situations, the control becomes complex, and the

transient loss is challenging to estimate and control accurately. Thus, PMSM drive systems working in steady-state are primarily investigated.

In steady-state operation, ω_e and T_{em} can be taken as fixed, and the power loss is only related to I_d. That is, if $dP_{total\_L}/dI_d = 0$ is satisfied, the minimum loss of PMSMs can be realized. Then, based on (4-18), making $dP_{total\_L}/dI_d = 0$, one has:

$$\begin{aligned}&\frac{m_1\left\{2I_d-\frac{8(L_d-L_q)T_{em}^2}{9n_p^2\left[\psi_f+(L_d-L_q)I_d\right]^3}\right\}}{2\sqrt{{I_d}^2+\frac{4T_{em}^2}{9n_p^2\left[\psi_f+(L_d-L_q)I_d\right]^2}}}-\frac{8T_{em}^2(L_d-L_q)(a_2+m_2)}{9n_p^2\left[\psi_f+(L_d-L_q)I_d\right]^3}\\&+\frac{2T_{em}[a_5\psi_f-a_3(L_d-L_q)]}{3n_p\left[\psi_f+(L_d-L_q)I_d\right]^2}+2(a_1+m_2)I_d+a_4=0\end{aligned} \tag{4-19}$$

It is seen that (4-19) is a complicated nonlinear equation about I_d, such that it is very difficult to solve the function $I_d = f(T_{em})$ conveniently to realize the loss minimization control. Thus, for simplifying computation, (4-19) is further written as:

$$F\left(T_{em}\right)=\frac{m_1(2I_d-Z_2T_{em}^2)}{2\sqrt{{I_d}^2+Z_3T_{em}^2}}+Z_4T_{em}^2+Z_5T_{em}+Z_1=0 \tag{4-20}$$

where

$$\begin{cases}Z_1=2(a_1+m_2)I_d+a_4\\Z_2=\dfrac{8(L_d-L_q)}{9n_p^2\left[\psi_f+(L_d-L_q)I_d\right]^3}\\Z_3=\dfrac{4}{9n_p^2\left[\psi_f+(L_d-L_q)I_d\right]^2}\\Z_4=-\dfrac{8(L_d-L_q)(a_2+m_2)}{9n_p^2\left[\psi_f+(L_d-L_q)I_d\right]^3}\\Z_5=\dfrac{2[a_5\psi_f-a_3(L_d-L_q)]}{3n_p\left[\psi_f+(L_d-L_q)I_d\right]^2}\end{cases} \tag{4-21}$$

As seem, (4-20) looks compact and the non-linearity also leads to difficulty in solving $dP_{total\_L}/dI_d = 0$ analytically. Consequently, the numerical Newton–Raphson search method [194] is employed to obtain the solution of (4-20). The iteration formula is,

$$T_{em}(k+1) = T_{em}(k) - \frac{F(T_{em}(k))}{F'(T_{em}(k))} \tag{4-22}$$

where $T_{em}(k)$ is the approximate solution at the k^{th} iteration.

With the solution of (4-20), the relationship between T_{em} and I_d is described, based on which the functions $I_d = F(T_{em})$ and $I_q = F(T_{em})$ can also be acquired with the numerical polynomial fitting method.

Therefore, the specific control diagram of the proposed loss minimization control method is given as Figure 4-2. In the control scheme, a proportional-integral (PI) regulator is employed to determine the optimal reference torque T_{em}^* by calculating the difference between the reference and actual speeds. The reference d-axis and q-axis currents (I_d^* and I_q^*) are determined using polynomial functions based on (4-20) - (4-22). The PWM controller is then employed to drive the inverter, effectively controlling the PMSM, aiming to enable the motor to operate efficiently and meet the desired loss minimization requirements.

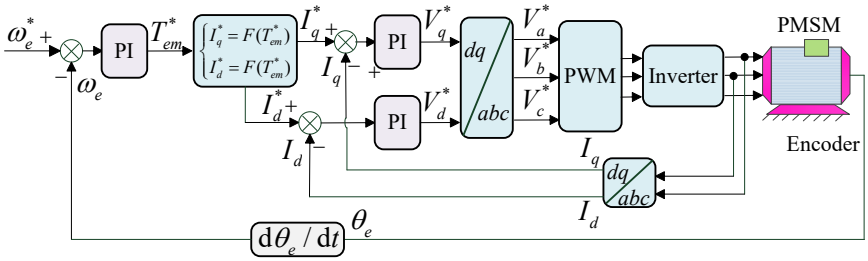

Figure 4-2 Block diagram of the proposed loss minimization control method.

4.4 Experiment Validation

Testing is performed on a 48-slot 8-pole V-type IPMSM prototype designed for EVs to validate the proposed approaches. It should be noted that all experiments were conducted under the sinusoidal PWM technique to obtain a sinusoidal output waveform. Effective values are used here, and the load equivalent resistance R_l is defined to be equal in both the d- and q-axis due to the symmetry of the circuit. This equivalent load resistance allows for the incorporation of complex factors that are challenging to model, including high-frequency harmonics, friction, and temperature variations, through the process of parameter identification.

4.4.1 Loss Analysis

Using the proposed ECM, the no-load iron loss P_{Fe_N} can be calculated as:

$$P_{Fe\_N} = \frac{3}{2}\left(\frac{1}{R_h} + \frac{1}{R_e} + \frac{1}{R_{an}}\right)E_0^2 \tag{4-23}$$

where E_0 is the back electromotive force.

At the same time, the no-load iron losses of a PMSM can also be estimated using the Bertotti model.

$$P_{Fe\_N} = K_h n + K_e n^2 + K_{an} n^{1.5} \tag{4-24}$$

where n is the motor speed, K_h, K_e, and K_{an} are the iron loss coefficients.

In combination with (4-23) and (4-24), one can get:

$$P_{Fe\_N} = \frac{3}{2}\left(\frac{1}{R_e} + \frac{1}{R_h} + \frac{1}{R_{an}}\right)E_0^2 = K_h n + K_e n^2 + K_{an} n^{1.5} \tag{4-25}$$

As known, the back electromotive force $E_0 = 4.44fN\phi_m$, where $f = nn_p/60$, n_p is the number of pole pairs. For our design, the number of poles is 8, and $E_0 = 0.0296nN\phi_m$. In order to determine R_h, R_e, and R_{an}, the no-load iron losses under different working speeds were obtained, based on which the loss coefficients can thus be fitted as $K_h = 1.854\times10^{-3}$ W/rpm, $K_e = 2.253\times10^{-6}$ W/(rpm)^2, and $K_{an} = 6.004\times10^{-4}$ W/rpm. The fundamental magnetic flux per pole can also be worked out as 2.048 mWb, while the number of turns of one phase winding was obtained as 48 by:

$$N_w = \frac{ZN_c}{ma} \tag{4-26}$$

where $Z = 48$ is the number of stator slots, $N_c = 3$ the number of coil turns, $m = 3$ the number of phases, and $a = 1$ the number of winding branches.

Furthermore, according to (4-25), it can also be deduced that R_h is a linear function of motor speed n, R_e is a constant, and R_{an} is proportional to the square root of n in this case. Finally, we can get that $R_h = 0.685n\ \Omega$, $R_e = 563.71\ \Omega$, and $R_{an} = 2.1153n^{0.5}\ \Omega$.

For load conditions, to describe the additional iron losses caused by the load current, an equivalent resistor R_i is employed to carry a portion of the input current that accounts for the additional iron loss caused by the load. To determine the value of R_i, the motor iron losses under various load currents and speeds were figured out. Then, according to the improved ECM in Figure 4-1, the relationship among load current, speed, and the additional iron loss can be expressed as:

$$P_{Fe\_add} = \frac{3}{2}[(\frac{(\omega_e L_q I_{mq})^2}{R_i} + \frac{(\omega_e L_d I_{md})^2}{R_i})] \tag{4-27}$$

Moreover, by observing the additional iron loss versus load current and speed curves, assuming that the additional iron loss is proportional to the square of the load current and motor speed, then, as for the prototype designs, the relationship (4-27) can be obtained by fitting methods. Finally, R_i can be calculated as 106.4069 Ω by $1.5(\omega_e L_d)^2/R_i$.

On the other hand, in our previous work [191], an improved iron loss analytical prediction model considering the effects of slotting harmonics and PWM carrier high-frequency harmonics was developed. Meanwhile, by measuring the magnetic properties of stator materials, temperature- and stress-dependent loss coefficients were obtained. However, compared to the model in [191], the presented ECM possesses advantages in computational complexity and implementation process, such that it was utilized to derive loss minimization control law in this manuscript. To demonstrate the effectiveness and accuracy of the proposed ECM under various operating points, a series of experiments were conducted, in which the iron losses of the IPMSM prototype were measured, and then compared with the values obtained by FEM, the improved analytical model in [191], and the proposed ECM.

Finally, the comparative results of core losses under both no-load and load (rated input current) conditions are obtained as Figure 4-3. As shown, under no-load condition, as the resistances including R_{an}, R_e, R_h are all fitted with actual loss data, the core loss values predicted with the proposed ECM are relatively close to those measured with the IPMSM prototype at different working speeds. Both the maximum and absolute average errors are below 2%, compared to the measured core loss values, which are smaller than the FEM results and accounting only around one third of the method in [191]. Under load condition, as seen from Figure 4-3 (b), because the model in [191] has considered coupling effects of multiphysics factors like harmonics, temperature rise and mechanical stress, it can predict the load core loss with high accuracy (within 5.22%). Moreover, the core loss

calculated with the proposed ECM also shows satisfactory prediction stability and accuracy. The maximum error is only 5.08%, while the absolute average error accounts for 3.74%, which are both only around 40% of the errors for the numerical FEM. All the results well-verify the effective performance of the proposed EMC for predicting no-load and load core losses of IPMSMs.

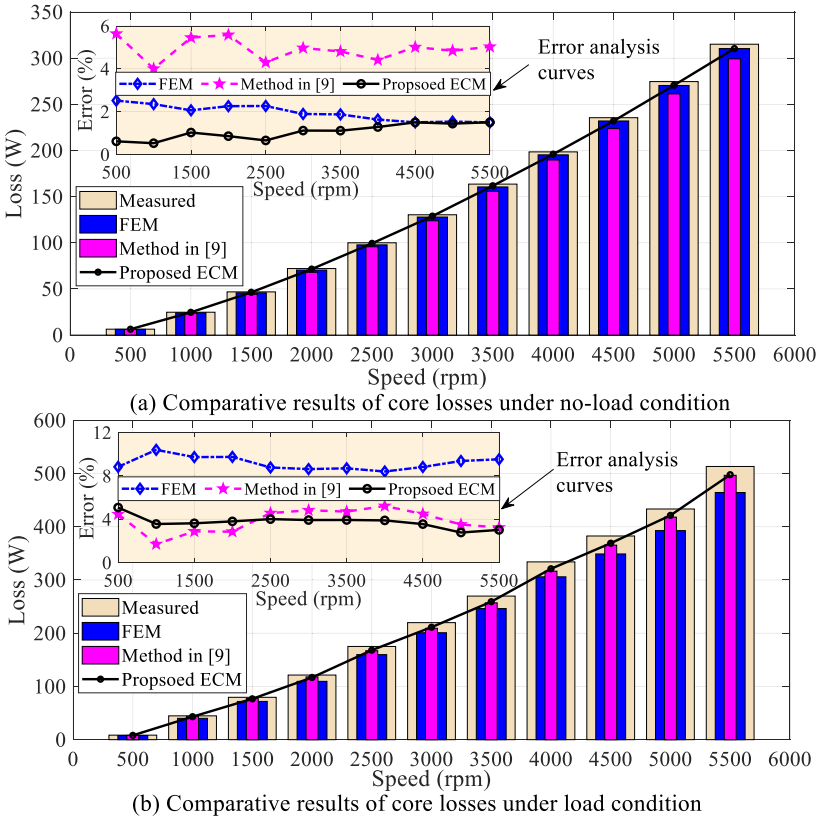

Figure 4-3 Comparative results of core losses obtained with various models.

4.4.2 Proposed ECM Model

The ECM can be used not only to calculate the losses of the motor but also to accurately determine the torque. This is crucial for motor design and application, as torque is one of the key performance indicators for measuring the motor's ability to drive loads. In conventional ECMs, the motors are usually idealized as lossless, and the electromagnetic torque T_{em} can be modeled as (4-7).

In the proposed ECM, the introduction of iron loss resistance components will cause changes in circuit currents, thereby affecting electromagnetic torque. Actually, the improved ECM with loss resistances is more realistic and can provide more accurate calculations of

electromagnetic torque. In this case, the torque calculation formula for the proposed ECM model should have been modified as:

$$P_{em} = \frac{3}{2}\omega_e \left(\lambda_f I_{mq} + L_d I_{md} I_{miq} - L_q I_{mq} I_{md} \right) \tag{4-28}$$

$$T_{em} = \frac{P_{em}}{\omega_m} = \frac{3}{2} n_p \left(\lambda_f I_{mq} + L_d I_{md} I_{miq} - L_q I_{mq} I_{md} \right) \tag{4-29}$$

In this study, before deriving the loss minimization control model, the authors have employed the proposed ECM model shown as (4-29), to calculate the mechanical characteristic curves of motor speed versus output torque, and then compared the data to those obtained by the electromagnetic torque model given as (4-7), and measured with the experimental prototype. The results are given as Figure 4-4. As seen, the adscititious iron loss resistances introduce additional physical phenomena and energy conversion processes. Therefore, when calculating the electromagnetic torque, the model of (4-29) can provide a bit more accurate and reliable results. However, the calculation results of ECMs when considering and not-considering the losses are quite close, and the errors are within a controllable range (maximum deviation is 3.21%, while average deviation is 2.76%) under various working conditions. More importantly, although the model in (4-29) is more accurate, it is also more complex and requires more circuit parameters to describe the physical characteristics. For establishing the loss minimization control model, using (4-29) would significantly increase the computational complexity. Thus, in order to balance the accuracy and computational efficiency, this work used the simplified model (4-7) for eliminating I_q in the system-level loss model.

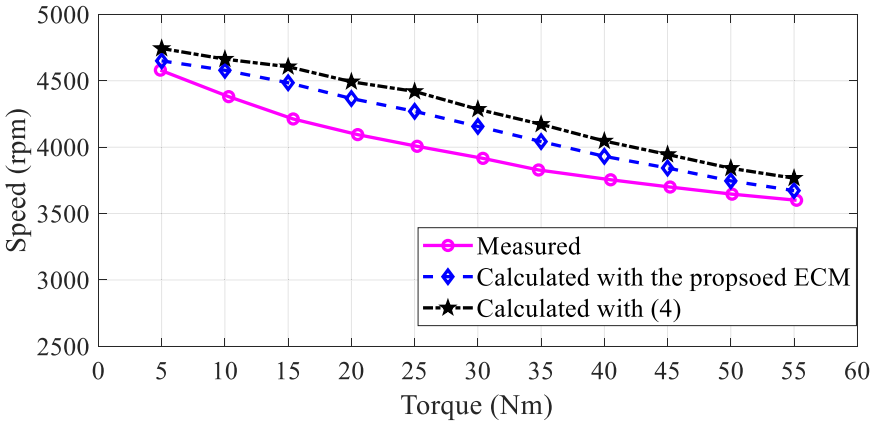

Figure 4-4 Comparative results of PMSM mechanical characteristics with fixed DC link voltage.

4.4.3 Improved Loss Minimization Control

An improved loss minimization control method was designed in this work. The proposed approach integrates a system-level loss model based on the enhanced ECM model, in which the iron loss, copper loss and inverter loss are all considered simultaneously, as shown in (4-16). It is seen that in steady-state operation, ω_e and T_{em} can be taken as fixed and the power loss is only related to I_d. That is, if $dP_{total\_L}/dI_d = 0$ is satisfied, the minimum loss of PMSMs can be realized. Similar with MTPA, through solving $dP_{total\_L}/dI_d = 0$, given as (4-20), the functions $I_d=f(T_e)$ and $I_q=f(T_e)$ can be obtained.

Considering that the performance of the proposed loss minimization controller significantly influences the following design optimization of the PMSM drive system, three groups of comparative experiments are demonstrated, in which the loss control performance of the proposed controller is deeply analyzed and compared with those obtained with traditional FOC and MTPA methods. The results concerning loss indicators are all given as Figure 4-5.

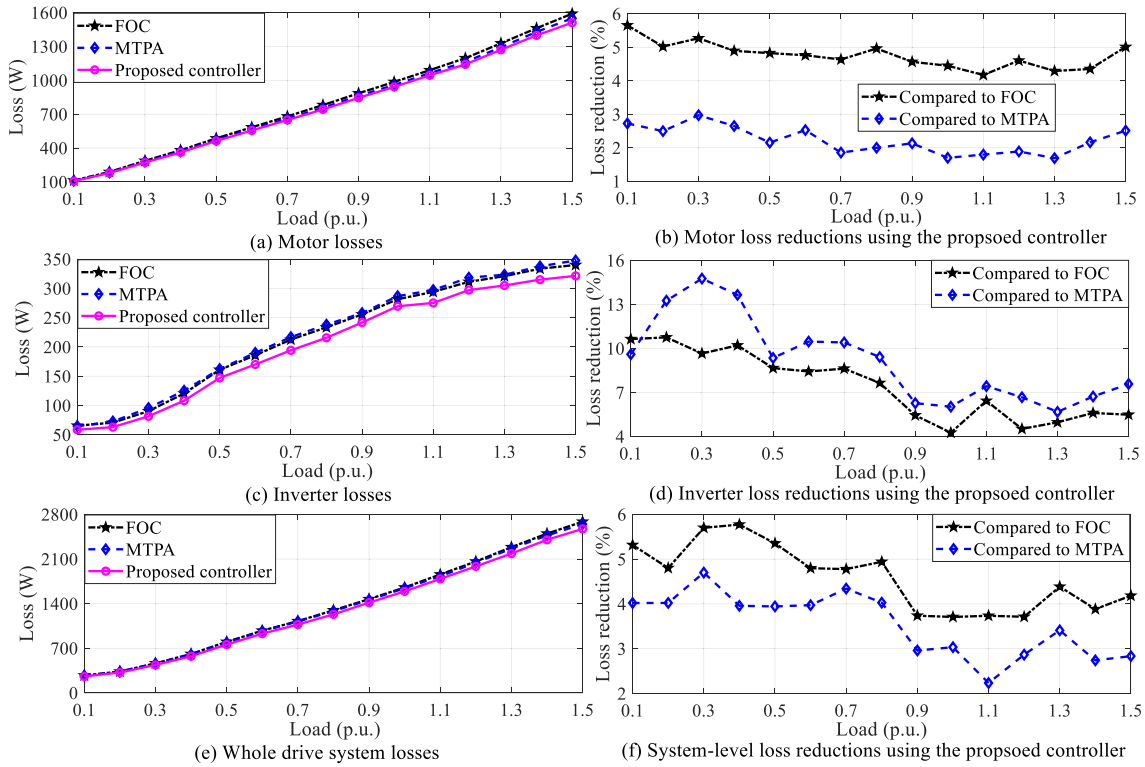

Figure 4-5 Comparative results of loss performances with various controllers.

As shown, under different working loads, using the proposed loss minimization controller, the PMSM drive system has the minimum motor loss, inverter loss and whole drive

system loss. Compared to FOC, the motor, inverter and system losses can be reduced by about 4.76 %, 7.42% and 4.59%, respectively, while the three loss indicators can be reduced by about 2.21%, 9.15% and 3.53%, compared to the MTPA method. The superiority of the proposed controller in efficiency improvement is verified.

4.5 Conclusion

This work proposes a comprehensive loss model for a PMSM system that includes both motor and inverter losses, and it develops an improved minimum loss control strategy to minimize steady-state drive losses. First, based on the mathematical model of the IPMSM drive system, the relationship between electromagnetic torque and *dq*-axis currents is derived using an equivalent transformation method to minimize electrical losses. Then, the reference *dq*-axis currents are calculated using a polynomial fitting method. The proposed overall strategy has been successfully applied to a 20 kW PMSM drive prototype system. Numerical simulations and experimental tests validate that, in steady-state operation, the proposed strategy effectively reduces motor, inverter, and total losses at various speeds and loads compared to MPTA and FOC controllers.

Chapter 5

System-Level Design Optimization for An IPMSM Drive System of Electric Vehicles

5.1 Introduction

Designing and optimizing electric drive systems for enhanced performance and higher efficiency is urgent and significant, garnering considerable innovation investments and research focus [195]. While researchers have made substantial efforts to optimize PMSMs and drive systems, technical challenges in complex operating conditions for EV drive systems remain [196]. First, existing design optimization has predominantly employed single-objective approaches, and to fully exploit optimization benefits, a shift towards multi-objective optimization is crucial to achieving a balanced set of performances [197]. Furthermore, previous optimization methods have often focused on component-level enhancements, which may not always lead to the overall optimization of the entire drive system [195]. Modern systems demand specific, integrated design and optimization to support multiple performance indicators effectively.

The effectiveness of system-level performance optimizations depends highly on the accuracy of the developed models and the efficiency of the optimization strategies employed. For the optimization models, multi-objective optimization is quite suitable for optimizing PMSM drive systems as they typically involve multiple performance metrics, like efficiency, torque, response time, current waveform quality, cost, and reliability [198]. Furthermore, these metrics are often interrelated and may present trade-offs and conflicts. Several intelligent algorithms, like MOGA [199], NSGA and NSGA II [200], and MPSO [201], effectively address non-inferior Pareto optimums. Despite their global optimization advantages and robustness, their application in electric drive system design optimization is hindered by limited calculation efficiency, particularly in handling high-dimensional FEMs. A novel multi-level optimization strategy can be explored to overcome these challenges with enhanced optimization for conflicting parameters.

To address these challenges and better optimize the sensitive parameters, some improved optimization strategies have been developed. Crevecoeur *et al*. [202] and Gong *et al*. [203] introduced space mapping methods for the design optimization of electrical machines, in which the optimization issues can be conducted in the coarse model space only. However, the undesirable accuracy of the coarse model leads to optimization solution errors. Considering the unnecessary waste of computation cost that comes from the samples outside the interested subspaces, Lebensztajn *et al*. [204] and Lim *et al*. [205] reported space reduction sequential optimization methods for multi-objective design optimization of electrical machines. Although the sequential optimization method is efficient to reduce the samples of single- and multi-objective optimization, the large amount computation cost of FEM still exists in high-dimensional optimization problems, as the design parameters are not simplified. In our previous publications [206]-[208], a novel multi-level optimization method was investigated, by which the initial big and high-dimensional design parameter space is refined into several low dimensional subspaces by using sensitivity analysis methods to the covered parameters. As a result, the general optimization approximate models can be utilized in all sublevels to reduce the calculation complexity while maintaining optimization accuracy.

In summary, this work aims to present a system-level design optimization strategy for PMSM drive systems using an improved ECM-based loss minimization control method, targeting to maximize the torque and efficiency, while minimizing the torque ripple and speed overshoot. The critical contributions are manifested as follows. (i) A system-level loss analysis model is derived considering both the motor and inverter/controller, which is beneficial to the following loss minimization controller construction. (ii) The system level optimization model is developed for both the electrical machines and control units to guarantee the optimal whole system level performance of an IPMSM drive system in EVs. (iii) After dividing the design parameters into four subspaces based on the Pearson correlation coefficient analysis, the multi-level strategy is employed to solve the optimization model for calculation burden reduction and accuracy improvement.

5.2 Efficient Design Optimization

In this work, we have meticulously crafted a framework that intricately connects motor design with control optimization within a holistic system-level optimization. As given in Figure 5-1, an entire system-level design optimization framework of electric drive

systems with a specific PMSM and control system is presented. As given, there are five key steps including 1) defining system requirements; 2) selecting the motor and controller types & topology; 3) initially designing the motor and controller types & topology; 4) establishing system-level optimization models as (2-8); and 5) optimizing the models of the whole electric drive system, including both the motor and controller. Meanwhile, employing an advanced multi-level strategy, we systematically optimize the model step-by-step, focusing on specific subspaces within the whole parameter space. This hierarchical approach not only alleviates computational burden but also ensures optimal accuracy by efficiently exploring the design space and enhancing convergence towards a globally optimal solution.

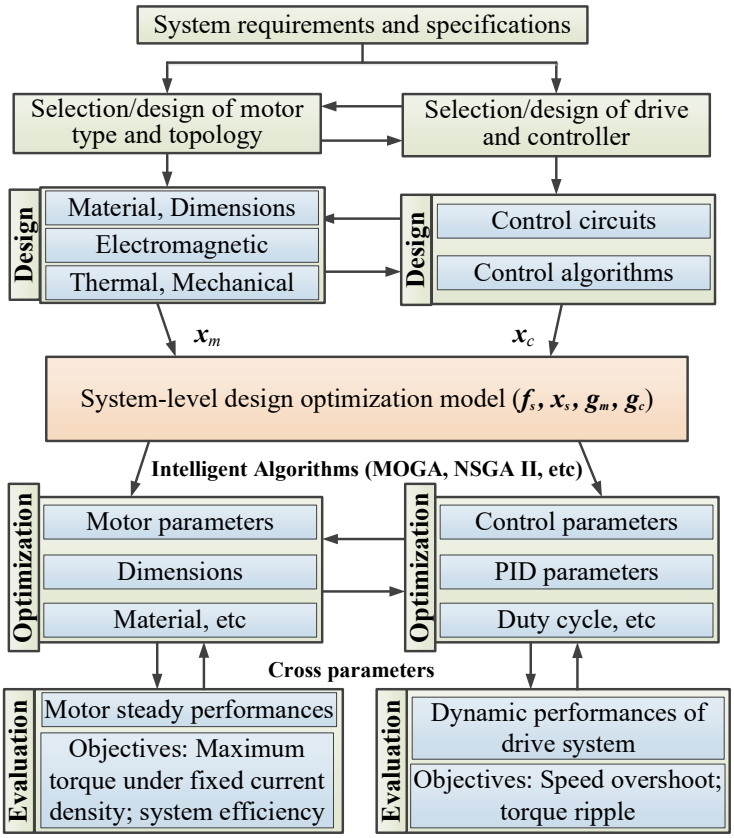

Figure 5-1 Framework of system-level design optimization of electric drive systems.

In the context of PMSM drive systems, our methodology strategically prioritizes the optimization of motor parameters preceding loss minimization controller parameters. This strategic sequencing is grounded in the pivotal influence of motor characteristics on overall system performance, encompassing dynamic response, efficiency, and stability. By prioritizing the optimization of key motor parameters, we establish a robust

foundation for subsequent fine-tuning of controller parameters. This sequential optimization strategy, validated in our prior publications [209]-[210], facilitates seamless coordination between optimized motor characteristics and control algorithms, thus elevating the overall system performance.

While our approach initially emphasizes motor design optimization followed by controller optimization, it is imperative to underscore the intrinsic interconnection between these processes within the used framework. Motor design and controller optimization are not conducted in isolation; rather, they engage in a symbiotic relationship throughout the optimization journey. At each iteration, motor parameters derived from the preceding optimization stage serve as pivotal inputs for refining controller parameters in subsequent stages. Moreover, the optimized controller parameters together with the motor parameters in this iteration, will also be employed as the new initial design values for the next iteration of optimization. This iterative refinement process ensures a tightly coupled optimization trajectory between motor design and controller parameters, fostering synergistic enhancement of the entire system.

5.3 Multi-Objective Optimization with Multi-Level Strategy

5.3.1 System-level Multi-objective Optimization Method

Several steps are highlighted for system-level design optimization of drive systems with specific PMSMs and controllers in this work.

Step 1: Define application-oriented system requirements including power, torque, speed, volume, weight, efficiency, etc. in allowed ranges based on the applications.

Step 2: Select the motor and controller types & topology. The interplay between multiphysics and control aspects should be considered. As for EVs, IPMSMs have been increasingly considered as suitable driving units considering their advantages in terms of efficiency, torque density, and speed range. However, IPMSMs may face challenges when developing high-order loss minimization controllers due to the unequal *d*-axis and *q*-axis inductances and the complex torque expressions.

Step 3: Initially design the motor and controller types & topology, including but not limited to materials, dimensions, electromagnetic, thermal and mechanical characteristics for the motor level, and the control circuits and algorithms for the control level.

Step 4: Establish system-level optimization models to accomplish the performance improvement for the whole system. In practice, the design requirements and optimization objectives of PMSM drive systems are complicated, and engineers prefer multi-objective optimization models to deal with the coupling effects among multiple factors.

To guarantee system-level performances of the drive systems, a system-level multi-objective model can be derived by combining the motor and controller design optimization models.

$$\begin{aligned} &\min: f_s(\mathbf{x}_s) = F(f_{mi}, f_{cj}), \quad i = 1,...,P_m; j = 1,...,P_c \\ &s.t. \quad g_{mi}(\mathbf{x}_s) \le 0, \quad i = 1,...,N_m \\ &s.t. \quad g_{ci}(\mathbf{x}_s) \le 0, \quad i = 1,...,N_c \\ &\mathbf{x}_{sl} \le \mathbf{x}_s \le \mathbf{x}_{su} \end{aligned} \tag{5-1}$$

where $\boldsymbol{x}_s = [\boldsymbol{x}_m, \boldsymbol{x}_c]$ is the decision variable set, $\boldsymbol{x}_m$ and $\boldsymbol{x}_c$ are the parameter vectors of motor level and control level, respectively, $\boldsymbol{x}_{sl}$ and $\boldsymbol{x}_{su}$ are the lower and upper boundaries of $\boldsymbol{x}_s$, f_s is the system-level objective, which is generally a function of motor level objectives f_{mi} and control level objectives f_{ci}, P_m and P_c are the numbers of objectives, while N_m and N_c are the numbers of constraints in motor and control levels, respectively. All the objectives and constraints should be defined in advance according to the requirements/specifications of applications.

Step 5: Optimize the models of the whole electric drive system, including both the motor and controller.

Step 6: Evaluate the whole system's performance.

5.3.2 Multi-level Optimization Strategy

The optimization models are often high-dimension problems, which leads to a huge computational cost for FEM and control simulation. To enhance the optimal efficiency, in this work, an advanced multi-level strategy is utilized, which optimizes the model step-by-step by focusing on specific subspaces within the whole parameter space, thereby

reducing the overall computational burden while achieving satisfactory optimal accuracy. The flowchart of a multi-level optimization strategy for PMSM drive systems is outlined as Figure 5-2. The specific processes are illustrated as follows.

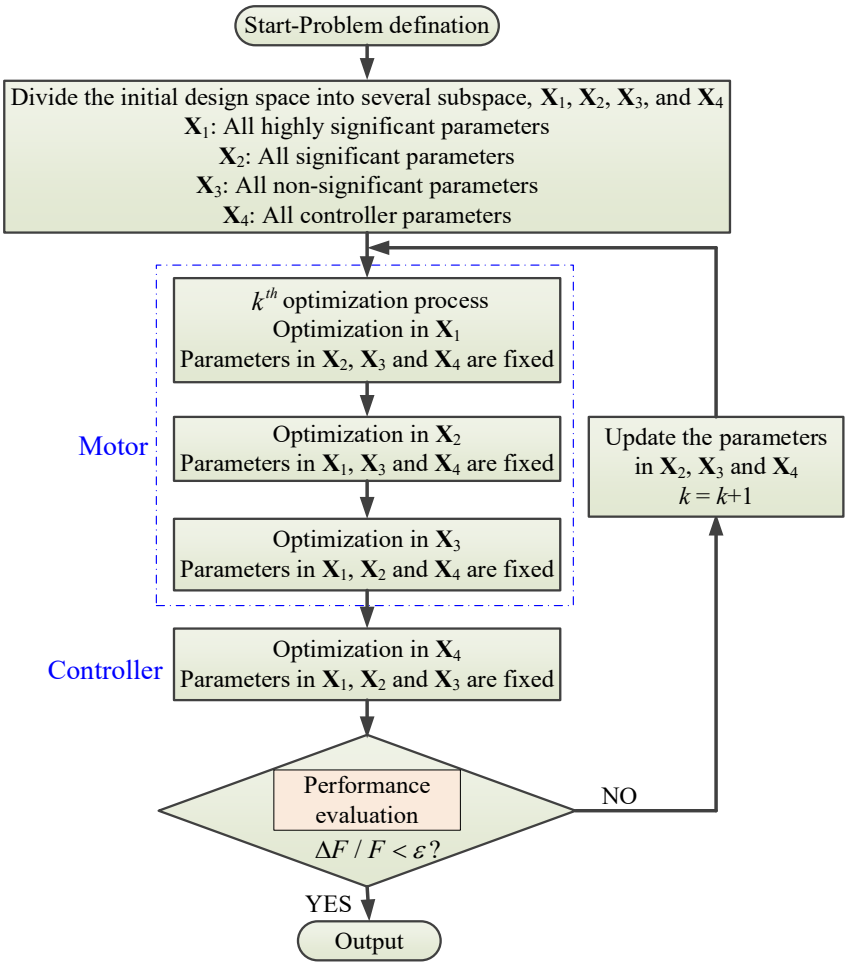

Figure 5-2 Flowchart of the proposed multi-level optimization strategy.

Step 1: With system-level optimization models, sensitivity analysis for all motor parameters will be carried out, by which the initial design space can be divided into several subspaces, i.e., $\mathbf{X}_1$ (highly-significant parameters), $\mathbf{X}_2$ (significant parameters), and $\mathbf{X}_3$ (non-significant parameters). Usually, the controller parameters are assigned in subspace $\mathbf{X}_4$. More subspaces can be defined reasonably if the dimensions are large.

In this study, the SPSS statistical tool is utilized. For example, in our case, it is necessary to specify the ranges of the parameters for the 10 defined motor variables as shown in Table I. Subsequently, perform a parameterized FEM analysis and document the effects of different design parameters on key motor performance indicators. Create a new data

table in SPSS and import the simulation results data into it. Conduct a correlation analysis using Pearson's coefficient to study the relationships among the target variables and the motor variables.

Step 2: Optimize subspace $\mathbf{X}_1$ when parameters in $\mathbf{X}_2$, $\mathbf{X}_3$ and $\mathbf{X}_4$ are fixed. In this study, an optimization process is conducted using approximate models and intelligent algorithms. Initially, a parametric FEM is developed in $\mathbf{X}_1$ for the studied PMSM, and simulations are performed. Then, the results will be utilized to evaluate motor performances and construct an approximate model for reducing computational costs. Subsequently, an intelligent algorithm is employed to find the Pareto solution set of $\mathbf{X}_1$, and the optimal solution is selected for optimizing $\mathbf{X}_2$.

Step 3: Optimize subspace $\mathbf{X}_2$ using the optimized parameters in $\mathbf{X}_1$, and the fixed parameters in $\mathbf{X}_3$ and $\mathbf{X}_4$. The same optimization process will be demonstrated.

Step 4: Optimize subspace $\mathbf{X}_3$ using the optimized parameters in $\mathbf{X}_1$ and $\mathbf{X}_2$, and the fixed parameters in $\mathbf{X}_4$. Similarly, after developing the FEM and the optimization model, the Pareto optimal solutions set of $\mathbf{X}_3$ can be obtained with an optimization algorithm.

Step 5: Optimize subspace $\mathbf{X}_4$ using the optimized parameters in $\mathbf{X}_1$, $\mathbf{X}_2$ and $\mathbf{X}_3$, the similar optimization process is carried out.

Step 6: Performance evaluation for PMSM drive systems with the optimal parameters. Continuously monitor the evolution of objective function F. If the relative error, defined as the changing rate of objective function $\Delta F/F$ in two consecutive iterations, is below a pre-determined threshold ε, end the iteration process and generate the optimized results. Otherwise, update the parameters in $\mathbf{X}_2$, $\mathbf{X}_3$ and $\mathbf{X}_4$, and proceed with another iteration following steps 2 to 6.

5.3.3 Optimization Techniques

Approximate models provide an efficient alternative to FEM, reducing computational burden, which express the relationships between objectives and parameters in multi-objective optimization. Among various modelling techniques, such as the response surface model, and radial basis functions model, the Kriging model stands out for its superior handling of local nonlinearities, as it considers both mean trend and variances of

responses. In this paper, the Kriging model is utilized and its required parameters are estimated by the software package DACE (Design and Analysis of Computer Experiments) in Matlab. The above parameters are involved in the main statements of the Kriging model script file as depicted in Figure 5-3.

```
theta = 10*ones(1,D);
lob = 0.01*ones(1,D);
upb = 200*ones(1,D);
[dmodel_ipmsm_reg1 perf] = dacefit(S,Y,@regpoly1,@corrgauss,theta,lob,upb);
```

Figure 5-3 A code example of the Kriging model in Matlab.

Multi-objective optimization involves finding solutions that strike a balance among multiple objectives. The Pareto solutions, which represent the best compromises, are obtained using optimization algorithms. Various techniques, such as DEA, NSGA, and its improved version NSGA II, have been applied to tackle multi-objective optimization problems. Notably, NSGA II stands out as a highly efficient multi-objective evolutionary algorithm and has been widely adopted in solving industrial multi-objective optimization problems. It usually includes two important components, i.e. the non-dominated sorting approach and the crowd comparison operator.

5.4 Experiment Validation

To clearly show the stator/rotor structure, the cross-section parameters are given as Figure 5-4, while 14 key dimensions are rationalized and confined as in Table IV. The IPMSM prototype with the FOC controller was manufactured with the parameters after component-level optimization.

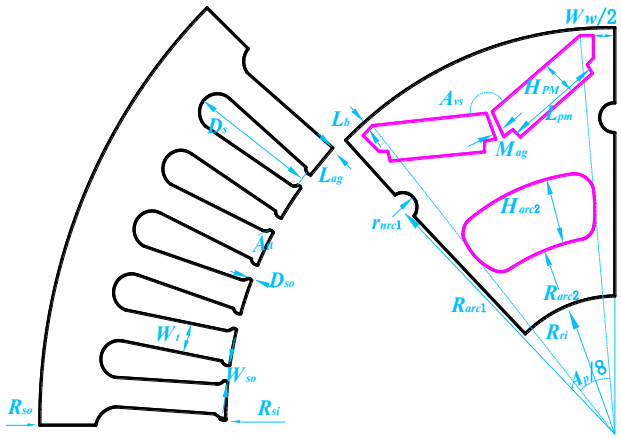

Figure 5-4 Structural parameters of the IPMSM.

TABLE IV Initial Design Parameters of The IPMSM

PARAMETERS	NOM.	VAL.	PARAMETERS	NOM.	VAL.
Stator inner radius	R_{ro}/mm	60-70	Bridge length	L_b/mm	1
Slot depth	D_s/ mm	17-22	Magnet air gap	M_{ag}/mm	1.57
Slot opening depth	D_{so}/mm	0.5-1.2	PM height	H_{pm}/mm	6
Slot opening width	W_{so}/mm	1.5-3.5	PM length	L_{pm}/mm	7-9
Tooth width	W_t/ mm	4.2	Pole angle	A_p/ deg	128-136
Tooth tip angle	A_{tt}/ deg	20-45	V-shape angle	A_{vs}/ deg	130-160
Air gap length	L_{ag}/mm	0.5-2	Web width	W_w/mm	5-7

Among these geometric parameters, the tooth width (W_t) and bridge length (L_b) are crucial for stator/rotor structural strength and magnetic flux leakage. While smaller values of W_t, L_b and magnet air gap (M_{ag}) can lead to better electromagnetic performance during electromagnetic finite element optimization, they cannot be too small due to stator and rotor mechanical strength limitations as well as over-saturation. The PM height (H_{pm}) is essential for PMs' demagnetization performance. A relatively small H_{pm} might lead to motor demagnetization, reducing motor reliability. Finally, the remaining ten motor parameters and the six PI gains for speed, *d*-axis and *q*-axis currents control, shown in Figure 4-2, are considered as the optimization decision variables.

There are a number of operation requirements of an EV drive system, concerning high steady and dynamic performance, cost, energy saving, environment, comfortability, etc. In this study, the optimization model is defined as:

$$\min: \begin{cases} f_1(\mathbf{X}_S) = -T_{\max} \\ f_2(\mathbf{X}_S) = T_{rip} \\ f_3(\mathbf{X}_S) = n_{os} \end{cases} \quad s.t.: \begin{cases} 0.85 - \eta_m \le 0; 150 - T_{\max} \le 0 \\ sf - 0.8 \le 0; J_C - 6 \le 0 \\ n_{os} - 0.1 \le 0; T_{rip} - 0.1 \le 0 \end{cases} \tag{5-2}$$

where T_{max} is the maximum torque, n_{os} the speed overshoot, and T_{rip} the torque ripple at the rated operating point. $\boldsymbol{X}_S$ is the designed decision variable vector in the system level, η_m the motor efficiency, *sf* the slot filling factor, and J_C the current density of stator winding. It should be noted that, in this study, the maximum efficiency goal is achieved through the proposed loss minimization control for not only further simplifying the optimal dimensions but also reducing the system-level loss.

As given in (5-2), it is a multi-objective optimization model which can achieve a balanced performance comprehensively with only Pareto optimal solutions instead of the single solution set. Therefore, a selection criterion is defined as (5-3), by which the candidate point can be chosen from the Pareto solutions for the iterations. The power loss is calculated through FEM.

$$\min: F_{cri} = \alpha_1 \frac{T_{\max\_ini}}{T_{\max}} + \alpha_2 \frac{P_{total}}{P_{total\_ini}} + \alpha_3 \frac{T_{rip}}{T_{rip\_ini}} + \alpha_4 \frac{n_{os}}{n_{os\_ini}} \tag{5-3}$$

where the subscript *ini* represents the parameters under the initial design. α_1, α_2, α_3 and α_4 are all weighting factors. Through extensive consultations, along with rich literature references, it is concluded that the torque and efficiency metrics are slightly more important than the latter two indicators, especially for EV drive systems. Consequently, the selection of the objective functions is typically defined based on the needs and goals from the users or relevant stakeholders. In this work, for effectively implementing the multi-level optimization strategy, the final optimal point needs to be selected reasonably from the Pareto optimal solutions, and then transmitted to the next level. Thus, a single-objective selection criterion is defined as (5-3) with four weighting coefficients.

It is established based on the required objective function instead of using a completely heuristic approach. Considering both the steady-state and dynamic performances, the maximum torque under fixed current density (T_{max}) ensuring stable operation and high performance, the system efficiency (η_s), reducing energy losses (P_{total}) and heat dissipation, thereby lowering energy consumption and operating costs, the torque ripple at rated working point (T_{rip}), reducing mechanical vibration and noise, as well as the speed overshoot (n_{os}), ensuring the performance stability, are set as the optimization objectives. Through extensive consultations and consideration from the authors, along with rich literature references, it was concluded that torque and efficiency metrics are slightly more important than the latter two indicators, especially for EV drive systems. Coupled with the rich experiences of the authors in the design and optimization of electric drive systems, the allocation of weights was determined as 0.3, 0.3, 0.2 and 0.2 for the four indicators, respectively. After obtaining the Pareto solutions, the single objective (5-3) can be used to choose the candidate points.

The Pearson sensitivity analysis method is also well-suited for assessing the relationships between objectives and decision variables efficiently, even when dealing with a large

number of parameters. Moreover, in practice, we need to estimate the sample standard deviations $s_{\mathbf{x}}$ and $s_{\mathbf{y}}$ to obtain the sample Pearson correlation coefficient with:

$$\rho(x_i, y_i) = \frac{\sum x_i y_i - n\overline{\mathbf{xy}}}{(N_s - 1)s_{\mathbf{x}}s_{\mathbf{y}}} = \frac{N_s \sum x_i y_i - \sum x_i \sum y_i}{\sqrt{N_s \sum x_i^2 - (\sum x_i)^2}\sqrt{N_s \sum y_i^2 - (\sum y_i)^2}} \tag{5-4}$$

where x_i are the design parameters, y_i are the optimization objectives, and N_s is the sample size.

In addition to the four non-optimized parameters mentioned above, the Pearson correlation coefficients of the remaining ten motor parameters on the objectives are calculated, as given in Figure 5-5. As shown, the air gap length (L_{ag}), PM length (L_{pm}), web width (W_w) and stator inner radius (R_{ro}) exhibit significant influences on the majority of objectives. The absolute average Pearson correlation coefficients for these variables are all greater than 0.85. The pole angle (A_p), slot depth (D_s) and slot opening width (W_{so}) have notably high Pearson correlation coefficients, averaging at 0.779, 0.776 and 0.782, respectively, while other parameters show values below 0.6. In this case, the subsections are distinguished as $\mathbf{X_1} = [x_1, x_2, x_3, x_4] = [L_{ag}, L_{pm}, W_w, R_{ro}]$, $\mathbf{X_2} = [x_5, x_6, x_7] = [A_p, D_s, W_{so}]$, and $\mathbf{X_3} = [x_8, x_9, x_{10}] = [D_{so}, A_{tt}, A_{vs}]$.

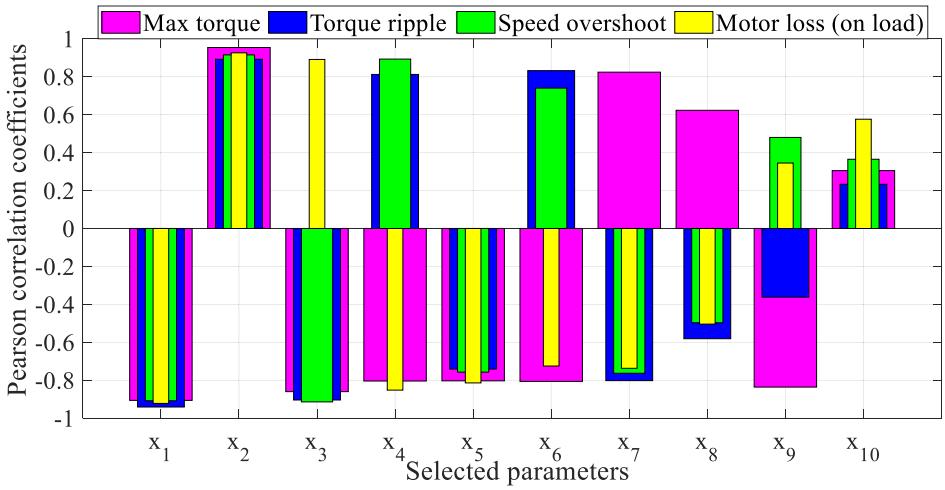

Figure 5-5 Sensitivities analysis results of the selected motor parameters.

On the other hand, considering that motor parameters are intrinsic to the design and construction, which may affect steady-state behaviors, but cannot be adjusted during operation, the six PI gains are categorized under the fourth level $\mathbf{X_4}$, optimizing responses to changing work conditions. The precedence of optimizing the motor parameters before

the controller parameters is grounded in the fundamental influence of motor characteristics on the overall drive system performance. By prioritizing the optimization of motor parameters initially, a robust foundation can be laid for subsequent tuning of controller parameters. This sequential optimization strategy, rooted in empirical observations of motor drive systems, ensures harmonious coordination between optimized motor characteristics and control algorithms, thus enhancing the system's overall performance.

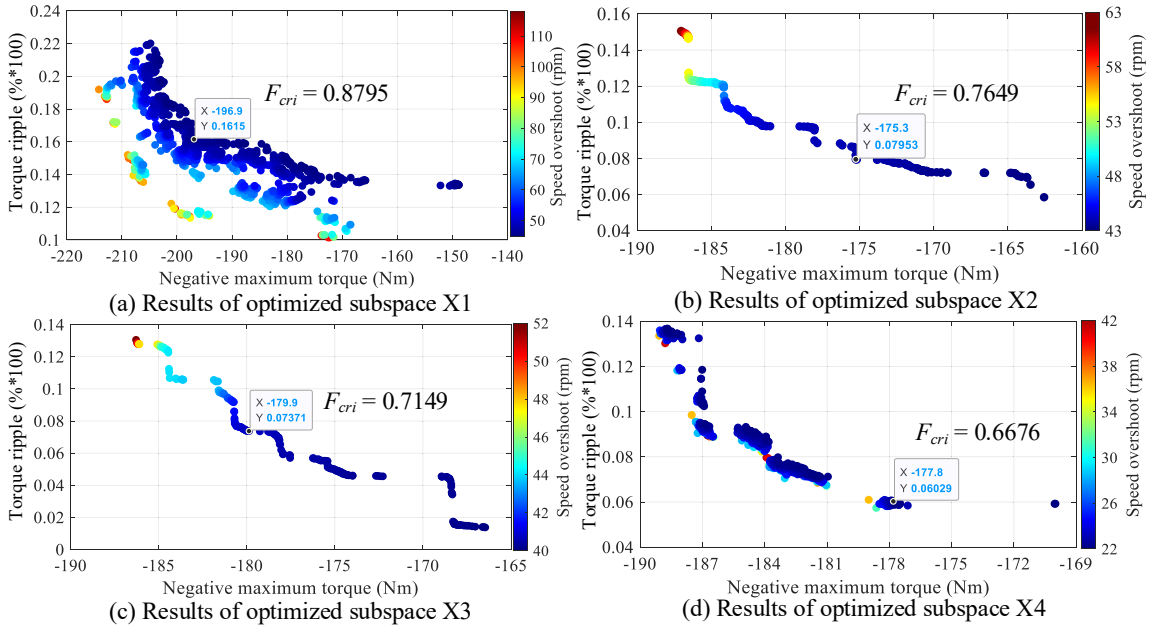

Figure 5-6 Pareto optimal solutions of iteration 1.

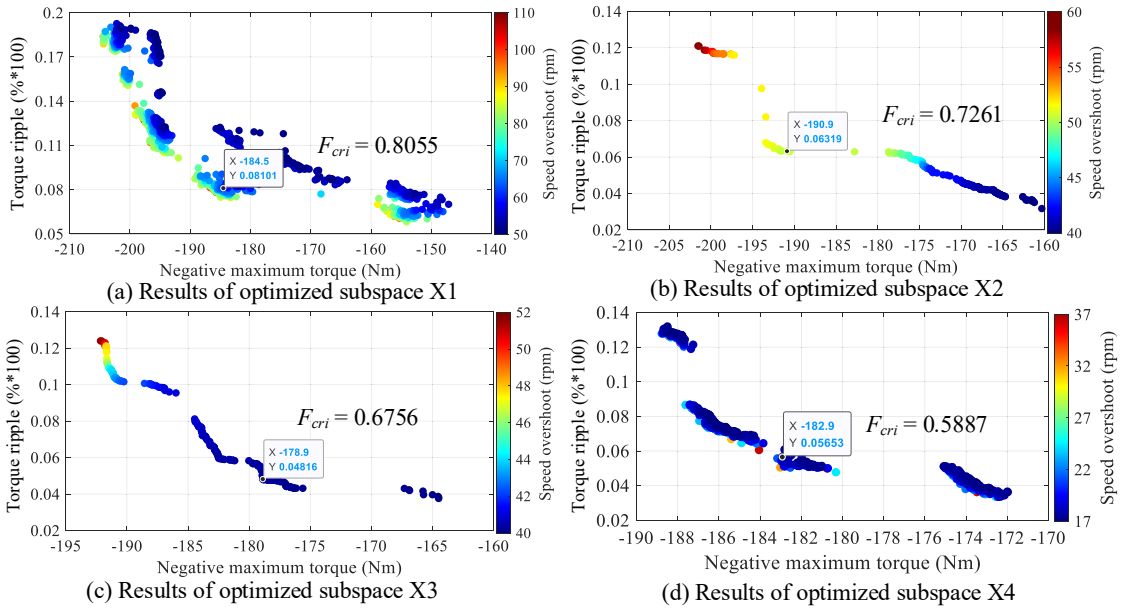

Figure 5-7 Pareto optimal solutions of iteration 2.

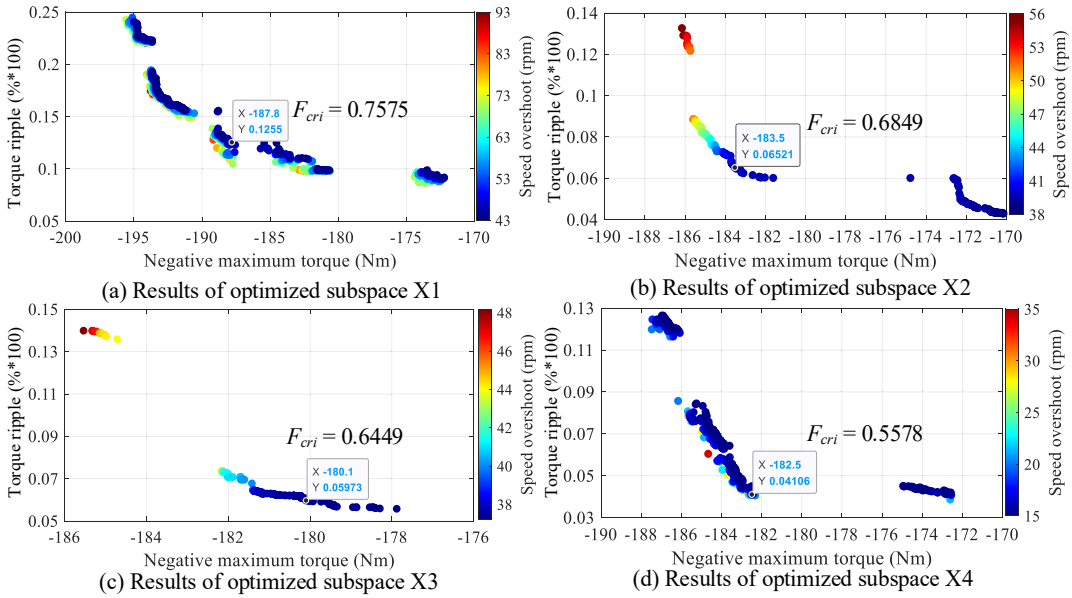

Figure 5-8 Pareto optimal solutions of iteration 3.

As illustrated, the Kriging model is utilized to approximate the IPMSM drive system model, while the NSGA-II optimization algorithm is selected for the solving process in each level. FEM and Matlab/Simulink are employed to calculate the system performances such as torque, speed, and torque ripple at rated speed. After three iterations, the convergence criterion of F_{cri} is triggered, and the Pareto optimal solutions of each sub-space under different iterations are expressed in Figure 5-6 to Figure 5-8.

In subspace $\mathbf{X}_1$ with 4 dimensions, 6^4 = 1296 FEM samples are generated for the optimization. As shown in Figure 5-6 (a), the proposed approach can obtain a series of Pareto solutions after the first level optimization. And the result with a minimum F_{cri} defined in (5-3) will be sent to the second level optimization of subspace $\mathbf{X}_2$, in which 6^3 = 216 samples are collected. Similarly, based on the selected optimal solution in $\mathbf{X}_1$ and $\mathbf{X}_2$, the optimization of subspaces $\mathbf{X}_3$ and $\mathbf{X}_4$ are accomplished using 6^3 = 216 and 3^6 = 729 samples, respectively. Thus, the total number of samples when using the proposed multi-level strategy is only 2457, much smaller than those in single-level optimization with 16 dimensions (about 5^{16}), which can undoubtedly reduce the computing costs greatly. Taking Figure 5-6 as an example for analysis, and comparing Figures 5-6 (a) and (b), it is seen that the torque ripple is reduced greatly, while comparing Figures 5-6 (c) and (d), the speed overshoot is suppressed, which indicates that optimization of subspace $\mathbf{X}_2$ and $\mathbf{X}_4$ is better in reducing the torque ripple and speed overshoot, respectively. The unanimous conclusion can also be obtained from Figure 5-7 and Figure 5-8.

The comparative results of each iteration are listed in Table V. As the iteration number increases, most performance metrics in the used IPMSM drive system are optimized. Compared to the initial scheme, the maximum torque is promoted from 160.5 to 182.5 Nm, while the torque ripple is reduced from 15.5% to 4.2%, and the speed overshoot is reduced from 75 to around 18.2 rpm. Moreover, the objective value F_{cri} also shows improvement, decreasing from 0.6676 to 0.5578, indicating that the final optimization results bring about the best balance in performance for the drive system. However, it is observed that during the iteration process, the maximum torque experiences a slight decrease, which may be a result of striking a balance among different objectives. Furthermore, the system's losses are maintained at around 1600 W, remaining relatively low due to the benefits of the proposed loss minimization control.

TABLE V Optimization Results of Each Iteration

NOM.	UNIT	INITIAL	ITERATION1	ITERATION2	ITERATION3
D_s	mm	17-22	19.8	20.2	19.9
L_{ag}	mm	0.5-2	1.67	0.89	1.63
W_{so}	mm	1.5-3.5	2.78	2.16	1.97
R_{ro}	mm	60-70	69.5	67.6	68.8
L_{pm}	mm	7-9	7.5	8.2	8.3
A_p	deg	128-136	128	128.1	128.1
W_w	mm	5-7	6.6	6.8	6.9
D_{so}	mm	0.5-1.2	0.72	0.79	0.70
A_{tt}	deg	20-45	27.4	26.1	24.7
A_{vs}	deg	130-160	153	155	145
C_{P1}	---	0.1	1.25	1.36	1.38
C_{P2}	---	0.1	0.47	0.42	0.42
C_{P3}	---	0.1	0.95	1.15	1.16
C_{I1}	---	0.05	0.16	0.11	0.13
C_{I2}	---	0.05	0.04	0.04	0.02
C_{I3}	---	0.05	0.35	0.64	0.70
T_{max}	Nm	160.5	177.8	182.9	182.5
T_{rip}	%	15.5	6.0	5.7	4.2
n_{os}	rpm	75	24.6	19.5	18.2
P_{total}	W	2500	2115	1666	1594
F	---	1.00	0.6676	0.5887	0.5578

The computational costs for each subspace are listed in Table VI. The optimization dimension is greatly reduced by using the multi-level strategy and the loss minimization controller. Most computational costs (less than 12 hours in each subspace, and less than 24 hours in total) are used for generating samples in simulations, while only several seconds are taken for solving models. The computing time is greatly reduced compared to one-level optimization with 16 dimensions (5^{16} samples).

TABLE VI Comparison of Computational Costs for Each Subspace

ISSUES	TIME $\mathbf{X}_1$	TIME $\mathbf{X}_2$	TIME $\mathbf{X}_3$	TIME $\mathbf{X}_4$
Simulation sample	11.26 h	2.47 h	3.19 h	6.72 h
Model solving	39.93 s	1.92 s	2.77 s	19.24 s

To verify the effectiveness of the proposed system-level optimization approaches utilizing the improved ECM-based loss minimization controller, the torque performances including the maximum and cogging torques, of the final optimized IPMSM drive system are analyzed and compared with those in the initial design point and prototype with the component-level optimized parameters and FOC, given as Figure 5-9 to Figure 5-10, respectively.

As shown in Figure 5-9, the maximum torque of the optimized drive system is about 182.5 Nm, 2.5% and 13.7% larger than that of the prototype (178 Nm) and the initial design scheme (160.5 Nm). Moreover, the torque ripple is reduced to 4.17%, only about one third of that in the initial drive system. As illustrated in Figure 5-10, the optimized cogging torque curve outperforms both the prototype and the initial design. Meanwhile, the maximum cogging torque in the optimized scheme is only 0.51 Nm, about 85% and 60% of the values measured with the prototype and those obtained via initial motor parameters.

Combining with the FEM model and Matlab/Simulink, the comparative results of working speed behaviors are outlined in Figure 5-11. As seen, the optimized IPMSM drive system exhibits significantly smaller speed overshoots (less than 1%) compared to the initial and measured systems across the entire speed range. Moreover, the average steady-state errors stay within 0.5% consistently, providing clear evidence of the enhanced dynamic performance achieved by the proposed optimization strategy.

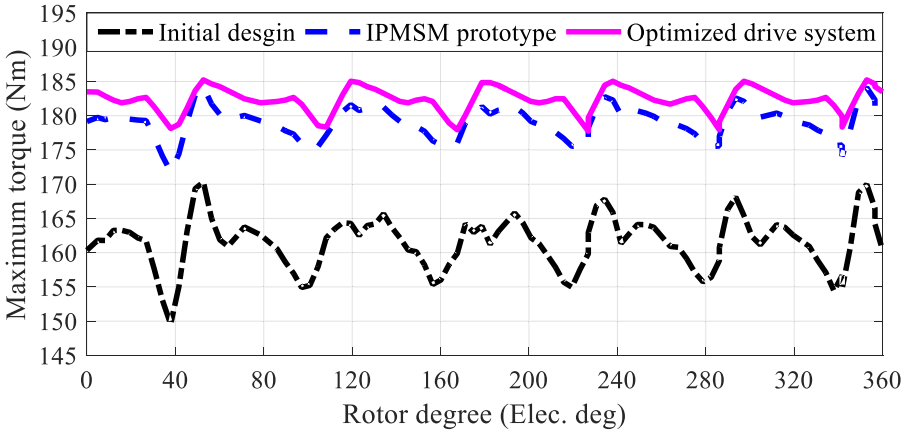

Figure 5-9 Comparative results of maximum torque.

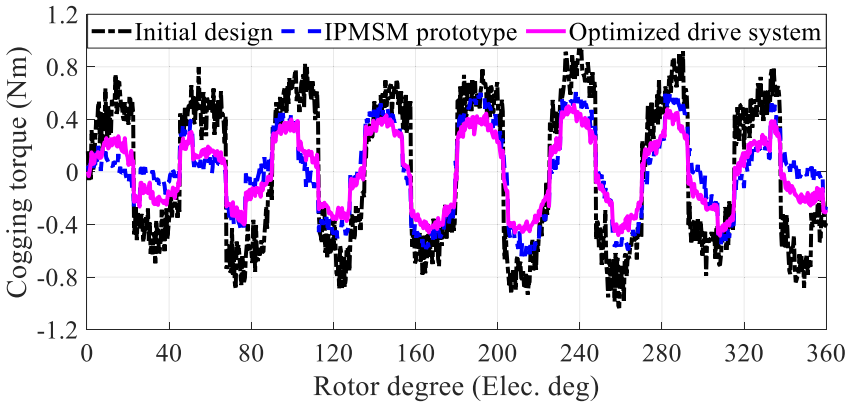

Figure 5-10 Comparative results of cogging torque.

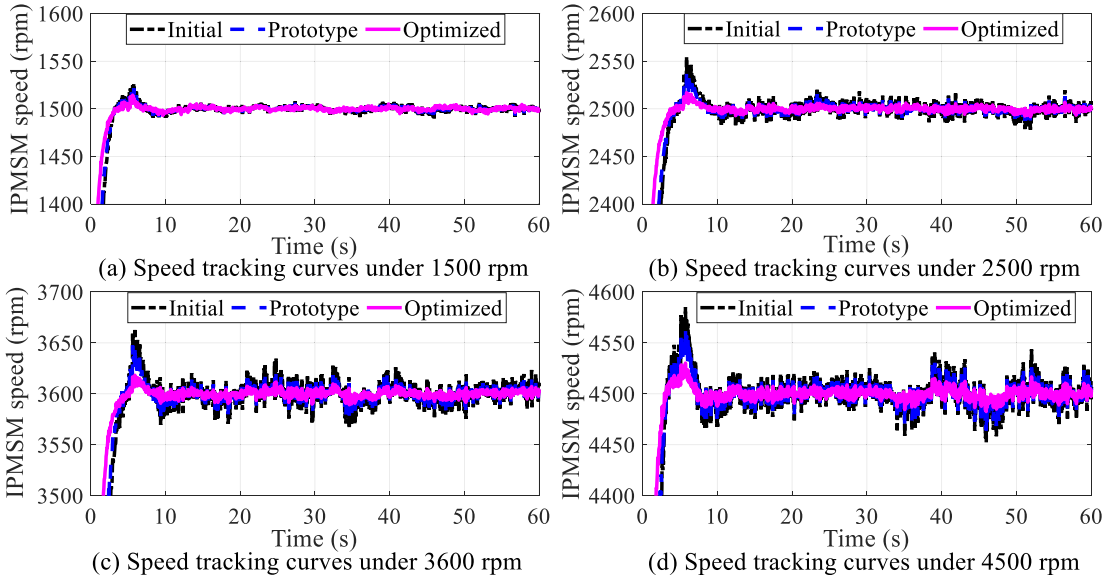

Figure 5-11 Comparative results of speed tracking curves.

Finally, to further validate the optimized results as well as the functions of the proposed loss minimization control method, the motor, inverter and system losses of the optimized PMSM drive system are calculated under rated load conditions and compared with those measured using the integrated experimental platform with a FOC method. The results are shown in Figure 5-12. Under different working speeds, the optimized IPMSM drive system with the proposed loss minimization control, can effectively reduce the motor loss and inverter loss by about 5.64% and 3.86%, as well as the system loss by about 4.57%. This is crucial for improving system efficiency with considerable significance. It can also be seen from Figure 5-13 that the optimized average system-level efficiency is up to 90.45%, higher than the average value measured with the prototype (87.20%).

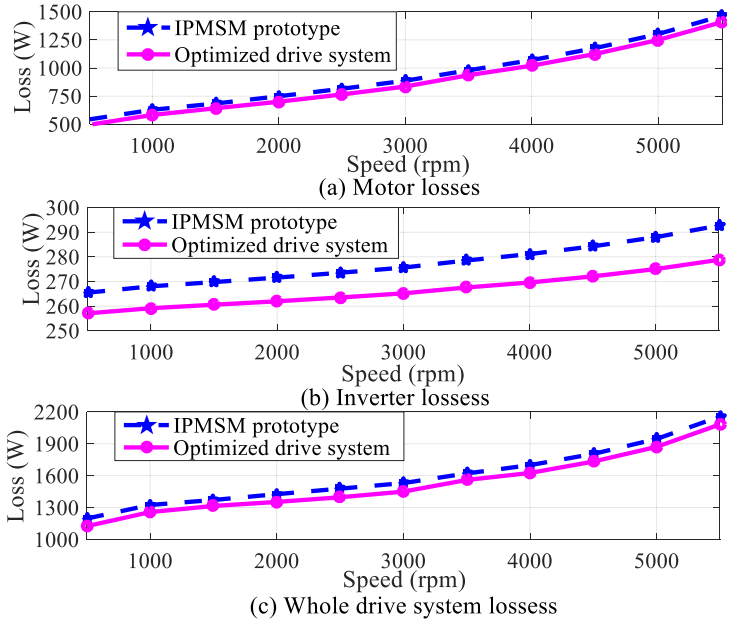

Figure 5-12 Comparative results of power losses.

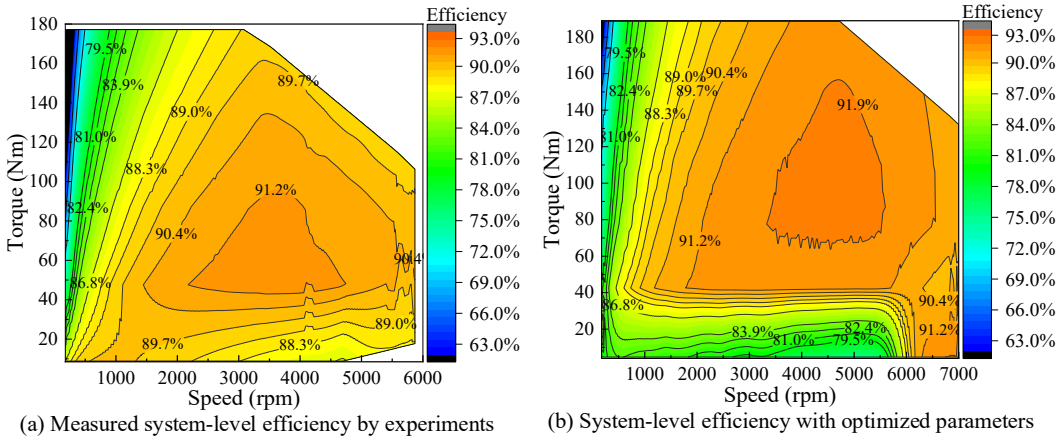

Figure 5-13 Comparative results of system-level efficiency map.

5.5 Conclusion

This work presented an improved system-level design optimization strategy for PMSM drive systems used in EVs. Multi-objectives were considered to achieve an optimal balance performance, and the multi-level scheme was utilized to reduce the computation burden. An effective loss minimization control method was synthesized to realize the system efficiency optimization. Comparative experimental and simulation case studies were demonstrated in an IPMSM drive system, by which the effectiveness of the proposed approaches was well verified. The main conclusions are as follows.

The proposed loss minimization control method successfully achieves its goal of minimizing energy losses, thereby boosting overall system efficiency without requiring multiple optimization stages. Meanwhile, both the steady-state and dynamic performances of the system are improved, while the design space is expanded and the searching speed is enhanced.

An optimal solution was selected from Pareto optimal sets with the defined selection criterion. Coupled with the sensitivity analysis and multi-level strategies, the optimization accuracy and efficiency can be guaranteed.

Experimental results validated that the optimized drive system realizes promoted performances in all aspects of efficiency, maximum torque, torque ripple and speed overshoot.

The outcomes from this study may provide a valuable guideline for the design optimization of various drive systems in electrified transportation. Future works will focus on exploring the robustness of the proposed optimization strategy under varying operating conditions and driving scenarios.

Chapter 6

Conclusions and Recommendations for Future Works

6.1 Conclusions

This thesis primarily focuses on the design and optimization techniques of application-oriented permanent magnet synchronous motor drive systems, with an emphasis on multidisciplinary coupling factors and system-level development. Chapter 2 provides a comprehensive review of the relevant literature, examining multidisciplinary design model establishment methods, basic optimization steps, and effective techniques and strategies for motors and their drive systems. Following this review, the study identifies key research areas, addresses existing issues, and validates the proposed techniques' effectiveness through various case studies.

i) This work presents a loss analysis model that integrates the coupling of multiple physical fields, such as magnetic fields, stress fields, and temperature fields, with the aim of more accurately analyzing and predicting the magnetic properties of materials. Using a novel magnetic measurement device, magnetic property data can be obtained under various conditions, such as stress, temperature, and frequency, to validate and optimize this model. The effects of slotting harmonics, PWM carrier harmonics, temperature rise and mechanical stress are considered in the proposed models. Through extensive simulations and experiments, it has been demonstrated that the proposed model possesses relatively accurate predictive performance under various conditions.

ii) A refined ECM featuring a novel topology is proposed for the expeditious and

efficient computation of core losses in PMSMs under both loaded and no-load conditions. In contrast to traditional ECMs, this improved model considers magnetic saturation while incorporates variable equivalent resistances for hysteresis, eddy current and anomalous losses, together. Moreover, based on the improved ECM model, a system-level loss model for PMSM drive systems that considers both motor and control units is established for implementing the loss minimization control, through which the high-order formulas and radical calculations are iteratively solved online by a numerical approach.

iii) A system-level design optimization strategy for PMSM drive systems is proposed in which the improved ECM-based system-level loss minimization control is integrated for not only simplifying the optimization process, but also better-guaranteeing efficiency improvement. Unlike conventional approaches focusing on individual components, this study adopts a holistic view of the entire system, allowing thorough consideration of complex interactions between the motor and controller. This ensures that all elements synergize to enhance overall system performance.

iv) Recognizing the high dimensionality of the optimization model, leading to significant computational costs for FEM and control simulation, a multi-level optimization strategy is introduced to solve the multi-objective optimization models. This strategy optimizes the models step-by-step by focusing on specific subspaces within the parameter space, thereby reducing the overall computational burden while achieving satisfactory optimal accuracy.

6.2 Recommendations for Future Works

Electric drive systems are the backbone of modern electric vehicles and industrial machinery. As the demand for higher efficiency, reliability, and performance grows, so does the need for advanced research in this field. Future work should focus on three main

areas: the impact of multidisciplinary factors, comprehensive performance evaluation, and the integration of AI technologies.

i) The performance of electric drive systems is influenced by a myriad of multidisciplinary factors, including material properties, thermal dynamics, mechanical stresses, and electromagnetic interference. Future research should delve into how these factors interact and affect the system throughout its entire life cycle. By understanding these interactions, it will be possible to develop more robust and efficient electric drive systems. This holistic approach requires collaboration across various fields such as material science, mechanical engineering, thermal management, and electrical engineering.

ii) Traditionally, the design and optimization of electric drive systems have focused on steady-state conditions. However, this approach provides an incomplete picture of the system's performance and reliability. Future work should incorporate transient analysis and multi-operation scenario analysis. Transient analysis considers the system's response to changes in load, speed, and other dynamic conditions. Multi-operation scenario analysis evaluates performance across different operating conditions, such as varying temperatures, load profiles, and environmental conditions. By adopting these methods, researchers can more comprehensively assess and enhance the performance and reliability of electric drive systems.

iii) The complexity of multidisciplinary coupling effects in electric drive systems poses significant challenges. AI technologies, particularly machine learning and deep learning, offer powerful tools to address these challenges. Future research should focus on leveraging AI to analyze large datasets, identify patterns, and predict system behavior under various conditions. AI can also optimize system design by exploring a vast space of design parameters and

configurations more efficiently than traditional methods. By integrating AI, it is possible to achieve more accurate predictions and optimizations, ultimately leading to superior electric drive systems.

References

[1] K. Hu, C. Raghutla, K. R. Chittedi, R. Zhang, and M. A. Koondhar, "The effect of energy resources on economic growth and carbon emissions: a way forward to carbon neutrality in an emerging economy," *Journal of Environmental Management*, vol. 298, no. 3, pp. 113448, Nov. 2021.

[2] P. Liu, Z. Wang, S. Wei, Y. Bo, and S. Pu, "Recent developments of modulation and control for high-power current-source-converters fed electric machine systems," *CES Transactions on Electrical Machines and Systems*, vol. 4, no. 3, pp. 215-226, Sep. 2020.

[3] G. Lei, T. Wang, J. Zhu, Y. Guo, and S. Wang, "System-level design optimization method for electrical drive systems-robust approach," *IEEE Transactions on Industrial Electronics*, vol. 62, no. 8, pp. 4702-4713, Aug. 2015.

[4] X. Sun, Z. Shi, Y. Cai, G. Lei, Y. Guo, and J. Zhu, "Driving cycle oriented design optimization of a permanent magnet hub motor drive system for a four-wheel-drive electric vehicle," *IEEE Transactions on Transportation Electrification*, vol. 6, no. 3, pp. 1115-1125, Sep. 2020.

[5] J. Benzaquen, J. He and B. Mirafzal, "Toward more electric powertrains in aircraft: Technical challenges and advancements," *CES Transactions on Electrical Machines and Systems*, vol. 5, no. 3, pp. 177-193, Sep. 2021.

[6] Z. Yang, F. Shang, I. P. Brown, and M. Krishnamurthy, "Comparative study of interior permanent magnet, induction, and switched reluctance motor drives for EV and HEV applications," *IEEE Transactions on Transportation Electrification*, vol. 1, no. 3, pp. 245-254, Oct. 2015.

[7] G. Choi and G. Bramerdorfer, "Comprehensive design and analysis of an interior permanent magnet synchronous machine for light-duty passenger EVs," Early access in *IEEE Access*, doi: 10.1109/ACCESS.2021.3137897.

[8] Y. Sun, H. Yue, J. Zhang, and C. Booth, "Minimization of residential energy cost considering energy storage system and EV with driving usage probabilities," *IEEE Transactions on Sustainable Energy*, vol. 10, no. 4, pp. 1752-1763, Oct. 2019.

[9] G. Liu, M. Liu, and Y. Zhang, "High-speed permanent magnet synchronous motor iron loss calculation method considering multi-physics factors," *IEEE Transactions on Industrial Electronics*, vol. 67, no. 7, pp. 5360-5368, Jul. 2020.

[10] G. Lei, J. Zhu, and Y. Guo, *Multidisciplinary Design Optimization Methods for Electrical Machines and Drive Systems*, Berlin, Heidelberg: Springer Berlin / Heidelberg, 2016.

[11] G. Lei, T. Wang, Y. Guo, J. Zhu, and S. Wang, "System-level design optimization methods for electrical drive systems: deterministic approach," *IEEE Transactions on Industrial Electronics*, vol. 61, no. 12, pp. 6591-6602, Dec. 2014.

[12] G. Lei, W. Xu, J. Hu, J. Zhu, Y. Guo, and K. Shao, "Multilevel design optimization of a FSPMM drive system by using sequential subspace optimization method," *IEEE Transactions on Magnetics*, vol. 50, no. 2, pp. 685-688, Feb. 2014.

[13] K. Ahn, A. E. Bayrak, and P. Y. Papalambros, "Electric vehicle design optimization: integration of a high-fidelity interior-permanent-magnet motor model," *IEEE Transactions on Vehicular Technology*, vol. 64, no. 9, pp. 3870-3877, Sep. 2015.

[14] L. Jia, M. Lin, W. Le, N. Li, and Y. Kong, "Dual-skew magnet for cogging torque minimization of axial flux PMSM with segmented stator," *IEEE Transactions on Magnetics*, vol. 56, no. 2, pp. 1-6, Feb. 2020.

[15] H. Ying, S. Huang, and D. Xu, "An high-speed low-noise rotor topology for EV/HEV PMSM," *CES Transactions on Electrical Machines and Systems*, vol. 1, no. 4, pp. 354-359, Dec. 2017.

[16] Y. Zhang, S. McLoone, and W. P. Cao, "Power loss and thermal analysis of a MW high speed permanent magnet synchronous machine," *IEEE Transactions on Energy Conversion*, vol. 32, no. 4, pp. 1468–1478, Dec. 2017.

[17] M. Lim, J. Kim, and Y. Hwang, *et al*., "Design of an ultra-high-speed permanent-magnet motor for an electric turbocharger considering speed response characteristics," *IEEE/ASME Transactions on Mechatronics*, vol. 22, no. 2, pp. 774-784, Apr. 2017.

[18] T. Sun, J. M. Kim, and G. H. Lee, *et al*., "Effect of pole and slot combination on noise and vibration in permanent magnet synchronous motor," *IEEE Transactions on Magnetics*, vol. 47, no. 5, pp. 1038–1041, May 2011.

[19] M. Lim, S. Chai, and J. Yang, *et al*., "Design and verification of 150-rpm PMSM based on experiment results of prototype," *IEEE Transactions on Industrial Electronics*, vol. 62, no. 12, pp. 7827-7836, Dec. 2015.

[20] N. Bianchi and S. Bolognani, "High speed drive using a slotless PM motor," *IEEE Transactions on Power Electronics*, vol. 21, no. 4, pp. 1083-1090, Jul. 2006.

[21] J. Wang, F. Wang, and X. Kong, "Design and analysis of electromagnetic properties for high speed PM generator," *Proceedings of the CSEE*, vol. 28, no. 20, pp. 105-110, Jul. 2008.

[22] A. Borisavljević, "Limits, modelling and design of high-speed permanent magnet machines," Delft, Netherlands: Delft University of Technology, thesis (PhD), 2011.

[23] G. Cvetkovski and L. Petkovska, "Performance improvement of PM synchronous motor by using soft magnetic composite material," *IEEE Transactions on Magnetics*, vol. 44, no. 11, pp. 3812-3815, Nov. 2008.

[24] Y. Huang, Q. Hu, and J. G. Zhu, "Magneto-thermal anaIysis of a highspeed claw pole motor consjdering rotational core loss," *Transactions of China Electrotechnical Society*, vol. 25, no. 5, pp. 54-60, May 2010.

[25] Y. Guo and J. Zhu, "Applications of soft magnetic composite materials in electrical machines: A Review," *Australian Journal of Electrical and Electronics Engineering*,

vol. 3, no. 1, pp. 37-46, Jan. 2006.

[26] A. G. Jack, B. C. Mecrow, and C. P. Maddison, "Combined radial and axial permanent magnet motors using soft magnetic composites," *Ninth International Conference on Electrical Machines and Drives*, Canterbury, UK, 1999, pp. 25-29.

[27] G. Cvetkovski, L. Petkovska, M. Cundev, and S. Gair, "Improved design of a novel PM disk motor by using soft magnetic composite material," *IEEE Transactions on Magnetics*, vol. 38, no. 5, pp. 3165-3167, Sep. 2002.

[28] C. -W. Kim, G. -H. Jang, J. -M. Kim, J. -H. Ahn, C. -H. Baek, and J. -Y. Choi, "Comparison of axial flux permanent magnet synchronous machines with electrical steel core and soft magnetic composite core," *IEEE Transactions on Magnetics*, vol. 53, no. 11, pp. 1-4, Nov. 2017.

[29] M. Aoyama, H. Tsuya, S. Hirata, and L. Sjöberg, "Experience of toroidally wound double rotor axial-gap induction machine with soft magnetic composites," *IEEE Open Journal of Industry Applications*, vol. 2, pp. 378-393, Dec. 2021.

[30] Y. Huang, J. Zhu, Y. Guo, Z. Lin, and Q. Hu, "Design and analysis of a high-speed claw pole motor with soft magnetic composite core," *IEEE Transactions on Magnetics*, vol. 43, no. 6, pp. 2492-2494, Jun. 2007.

[31] Y. Guo, J. Zhu, and D. G. Dorrell, "Design and analysis of a claw pole permanent magnet motor with molded soft magnetic composite core," *IEEE Transactions on Magnetics*, vol. 45, no. 10, pp. 4582-4585, Oct. 2009.

[32] W. Du, S. Zhao, H. Zhang, M. Zhang, and J. Gao, "A novel claw pole motor with soft magnetic composites," *IEEE Transactions on Magnetics*, vol. 57, no. 2, pp. 1-4, Feb. 2021.

[33] J. G. Zhu, Y. G. Guo, Z. W. Lin, Y. J. Li, and Y. K. Huang, "Development of PM transverse flux motors with soft magnetic composite cores," *IEEE Transactions on Magnetics*, vol. 47, no. 10, pp. 4376-4383, Oct. 2011.

[34] J. Doering, G. Steinborn, and W. Hofmann, "Torque, power, losses, and heat calculation of a transverse flux reluctance machine with soft magnetic composite materials and disk-shaped rotor," *IEEE Transactions on Industry Applications*, vol. 51, no. 2, pp. 1494-1504, Mar.-Apr. 2015.

[35] C. Liu, G. Lei, B. Ma, Y. Wang, Y. Guo, and J. Zhu, "Development of a new low-cost 3-D flux transverse flux FSPMM with soft magnetic composite cores and ferrite magnets," *IEEE Transactions on Magnetics*, vol. 53, no. 11, pp. 1-5, Nov. 2017.

[36] O. Maloberti *et al*., "3-D–2-D dynamic magnetic modelling of an axial flux permanent magnet motor with soft magnetic composites for hybrid electric vehicles," *IEEE Transactions on Magnetics*, vol. 50, no. 6, pp. 1-11, Jun. 2014.

[37] R. Kobler, D. Andessner, G. Weidenholzer, and W. Amrhein, "Development of a compact and low cost axial flux machine using soft magnetic composite and hard ferrite," *2015 IEEE 11th International Conference on Power Electronics and Drive*

Systems, Sydney, NSW, Australia, 2015, pp. 810-815.

[38] W. Du, S. Zhao, H. Zhang, M. Zhang, and J. Gao, "A novel claw pole motor with soft magnetic composites," *IEEE Transactions on Magnetics*, vol. 57, no. 2, pp. 1-4, Feb. 2021.

[39] S. Chu, D. Liang, S. Jia, and Y. Liang, "Research and analysis on design characteristics of high-speed permanent magnet claw pole motor with soft magnetic composite cores for wide temperature range," *IEEE Transactions on Industry Applications*, vol. 58, no. 6, pp. 7201-7213, Nov.-Dec. 2022.

[40] B. Li, X. Li, S. Wang, R. Liu, Y. Wang, and Z. Lin, "Analysis and cogging torque minimization of a novel flux reversal claw pole machine with soft magnetic composite cores," *Energies*, vol. 15, no. 4, pp. 1285, Feb. 2022.

[41] S. Kim, Y. Kim, and G. Lee, *et al*., "A novel rotor configuration and experimental verification of interior pm synchronous motor for highspeed applications," *IEEE Transactions on Magnetics*, vol. 48, no. 2, pp. 843-846, Feb. 2012.

[42] J. Dong, Y. Huang, and L. Jin, *et al*., "Review on high speed permanent magnet machines including design and analysis technologies," *Proceedings of the CSEE*, vol. 34, no. 27, pp. 4640-4653, Sep. 2014.

[43] F. Zhang, G. Du, and T. Wang, *et al*., "Review on development and design of high speed machines," *Transactions of China Electrotechnical Society*, vol. 31, no. 7, pp. 1-18, Apr. 2016.

[44] J. M. Yon, P. Mellor, and R. Wrobel, *et al*, "Analysis of semipermeable containment sleeve technology for high-speed permanent magnet machines," *IEEE Transactions on Energy Conversion*, vol. 27, no. 3, pp. 646-653, Sep. 2012.

[45] D. Gerada, A. Mebarki, and N. L. Brown, *et al*., "High-speed electrical machines: technologies, trends, and developments," *IEEE Transactions on Industrial Electronics*, vol. 61, no. 6, pp. 2946-2959, Jun. 2014.

[46] O. Aglén and A. Andersson, "Thermal analysis of a high-speed generator," *Proc. of 38th Industry Applications Conference*, Salt Lake City, 2003, pp. 547-554.

[47] K. Weeber, "Advanced electric machines technology," *Presentations from the 2009 Workshop on Future Large CO2 Compression Systems*, San Jose, CA, USA, 2009, pp. 1-15.

[48] J. J. H. Paulides, G. W. Jewell, and D. Howe, "An evaluation of alternative stator lamination materials for a high-speed, 1.5 MW, permanent magnet generator," *IEEE Transactions on Magnetics*, vol. 40, no. 4, pp. 2041-2043, Jul. 2004.

[49] S. Jang, D. You, and K. Ko, *et al*., "Design and experimental evaluation of synchronous machine without iron loss using double-sided Halbach magnetized PM rotor in high power FESS," *IEEE Transactions on Magnetics*, vol. 44, no. 11, pp. 4337-4340, Nov. 2008.

[50] J. Shen, H. Hao, and M. Jin, *et al*., "Reduction of rotor eddy current loss in high speed

PM brushless machines by grooving retaining sleeve," *IEEE Transactions on Magnetics*, vol. 49, no. 7, pp. 3973-3976, Jul. 2013.

[51] O. Aglen, "Loss calculation and thermal analysis of a high-speed generator," *Proceedings of International Electric Machines and Drives Conference*, 2003, pp. 1117-1125.

[52] Y. Yin and L. Li, "Improved method to calculate the high-frequency eddy currents distribution and loss in windings composed of round conductors," *IET Power Electronics*, vol. 10, no. 12, pp. 1494-1503, Oct. 2017.

[53] R. Fu and M. Dou, "Research on rotor harmonic copper losses of line-start REPMSM based on FEM," *2008 International Conference on Electrical Machines and Systems*, Wuhan, China, 2008, pp. 3085-3089.

[54] G. Bertotti, "General properties of power losses in soft ferromagnetic materials," *IEEE Transactions on Magnetics*, vol. 24, no. 1, pp. 621-630, Jan. 1988.

[55] J. G. Zhu and V. S. Ramsden, "Improved formulations for rotational core losses in rotating electrical machines," *IEEE Transactions on Magnetics*, vol. 34, no. 4, pp. 2234-2242, Jul. 1998.

[56] B. Tumberger, A. Hamler, and V. Gorican, *et al*., "Accuracy of iron loss estimation in induction motors by using different iron loss models," *Journal of Magnetism and Magnetic Materials*, vol. 276, no. 1, pp. 1723-1725, May 2004.

[57] S. L. Jiang, J. B. Zou, and Y. X. Xu, "Variable coefficient iron loss calculating model considering rotational flux and skin effect," *Proceedings of the CSEE*, vol. 31, no. 3, pp. 104–110, Jan. 2011.

[58] S. Shisha and C. Sadarangani, "Analysis of losses in inverter fed large scale synchronous machines using 2D FEM software," *2007 7th International Conference on Power Electronics and Drive Systems*, Bangkok, Thailand, 2007, pp. 807-811.

[59] N. Zhao, Z. Q. Zhu, and W. Liu, "Rotor eddy current loss calculation and thermal analysis of permanent magnet motor and generator," *IEEE Transactions on Magnetics*, vol. 47, no. 10, pp. 4199-4202, Oct. 2011.

[60] J. Xing, F. Wang, and D. Zhang, *et al*., "Research on rotor air friction loss of high-speed permanent magnet machines," *Proceedings of the CSEE*, vol. 30, no. 27, pp. 14-19, Sep. 2010.

[61] R. S. Colby and D. W. Novotny, "Efficient operation of surface-mounted PM synchronous motors," *IEEE Transactions on Industry Applications*, vol. IA-23, no. 6, pp. 1048-1054, Nov. 1987.

[62] Ji-Young Lee, Sang-Ho Lee, Geun-Ho Lee, Jung-Pyo Hong, and Jin Hur, "Determination of parameters considering magnetic nonlinearity in an interior permanent magnet synchronous motor," *IEEE Transactions on Magnetics*, vol. 42, no. 4, pp. 1303-1306, Apr. 2006.

[63] X. Ba, Y. Guo, J. Zhu, and C. Zhang, "An equivalent circuit model for predicting the

core loss in a claw-pole permanent magnet motor with soft magnetic composite core," *IEEE Transactions on Magnetics*, vol. 54, no. 11, pp. 1-6, Nov. 2018.

[64] L. Liu, X. Ba, Y. Guo, G. Lei, X. Sun, and J. Zhu, "Improved iron loss prediction models for interior PMSMs considering coupling effects of multiphysics factors," *IEEE Transactions on Transportation Electrification*, vol. 9, no. 1, pp. 416-427, Mar. 2023.

[65] B. Guo, Y. Huang, and Y. Guo, *et al*., "Thermal analysis of the conical rotor motor using LPTN with accurate heat transfer coefficients," *IEEE Transactions on Applied Superconductivity*, vol. 26, no. 7, pp. 1-7, Oct. 2016.

[66] J. Dong, Y. Huang, and L. Jin, *et al*., "Thermal optimization of a highspeed permanent magnet motor," *IEEE Transactions on Magnetics*, vol. 50, no. 2, pp. 749-752, Feb. 2014.

[67] S. Nategh, Z. Huang, and A. Krings, *et al*., "Thermal modelling of directly cooled electric machines using lumped parameter and limited CFD analysis," *IEEE Transactions on Energy Conversion*, vol. 28, no. 4, pp. 979- 990, Dec. 2013.

[68] B. Dong, K. Wang, and B. Han, *et al*., "Thermal analysis and experimental validation of a 30 kW 60000 r/min high-speed permanent magnet motor with magnetic bearings," *IEEE Access*, vol. 7, pp. 92184-92192, Jul. 2019.

[69] C. Dong, Y. Qian, and Y. Zhang, *et al*., "A Review of thermal designs for improving power density in electrical machines," *IEEE Transactions on Transportation Electrification*, doi: 10.1109/TTE.2020.3003194.

[70] C. Zhang, J. G. Zhu, and X. Y. Han, "Rotor strength analysis of highspeed surface mounted permanent magnet rotors," *Proceedings of the CSEE*, vol. 36, no. 17, pp. 4719-4727, Sep. 2016.

[71] C. Gong, S. Li, and T. Habetler, "High-strength rotor design for ultrahigh speed switched reluctance machines," *IEEE Transactions on Industry Applications*, vol. 56, no. 2, pp. 1432-1442, Mar.-Apr. 2020.

[72] Y. Le and J. Sun, "Modelling and design of 3-DOF magnetic bearing for high-speed motor including eddy-current effects and leakage effects," *IEEE Transactions on Industrial Electronics*, vol. 63, no. 6, pp. 3656-3665, Jun. 2016.

[73] T. Reichert, T. Nussbaumer, and W. Gruber, *et al*., "Bearingless permanent-magnet motor with 4/12 slot-pole ratio for bioreactor stirring applications," *IEEE/ASME Transactions on Mechatronics*, vol. 16, no. 3, pp. 431-439, Jun. 2011.

[74] G. Munteanu and A. Binder, "Loss measurement of a 40 kW highspeed bearingless PM synchronous motor," *2011 IEEE Energy Conversion Congress and Exposition*, Phoenix, AZ, 2011, pp. 722-729.

[75] H. Zhu and T. Zhang, "Finite element analysis for bearingless permanent magnet-type synchronous motors," *Proceedings of the CSEE*, vol. 26, no. 3, pp. 136-140, Feb. 2006.

[76] Q. Liao, Z. Deng, and X. Wang, *et al*., "Suspension force pulse analysis of consequent-pole bearingless PM motor," *Proceedings of the CSEE*, vol. 27, no. 30, pp. 49-54, Oct. 2007.

[77] K. N. Srinivas and R. Arumugam, "Static and dynamic vibration analyses of switched reluctance motors including bearings, housing, rotor dynamics, and applied loads," *IEEE Transactions on Magnetics*, vol. 40, no. 4, pp. 1911-1919, Jul. 2004.

[78] D. G Holmes and T. A. Lipo, *Pulse Width Modulation for Power Converters: Principles and Practice*, USA: Wiley & Sons, 2003.

[79] A. M. Hava, R. J. Kerkman, and T. A. Lipo, "A high-performance generalized discontinuous PWM algorithm," *IEEE Transactions on Industry Applications*, vol. 34, no. 5, pp. 1059-1071, Sep.-Oct. 1998.

[80] A. M. Hava, R. J. Kerkman, and T. A. Lipo, "Simple analytical and graphical methods for carrier-based PWM-VSI drives," *IEEE Transactions on Power Electronics*, vol. 14, no. 1, pp. 49-61, Jan. 1999.

[81] H. Qamar, H. Qamar, and R. Ayyanar, "Performance analysis and experimental validation of 240°-clamped space vector PWM to minimize common mode voltage and leakage current in EV/HEV traction drives," *IEEE Transactions on Transportation Electrification*, vol. 8, no. 1, pp. 196-208, Mar. 2022.

[82] T. Bhavsar and G. Narayanan, "Harmonic analysis of advanced bus-clamping PWM techniques," *IEEE Transactions on Power Electronics*, vol. 24, no. 10, pp. 2347-2352, Oct. 2009.

[83] H. Khan, E. Miliani, and K. E. K. Drissi, "Discontinuous random space vector modulation for electric drives: a digital approach," *IEEE Transactions on Power Electronics*, vol. 27, no. 12, pp. 4944-4951, Dec. 2012.

[84] C. B. Jacobina, A. M. N. Lima, E. R. C. da Silva, and A. M. Trzynadlowski, "Current control for induction motor drives using random PWM," *IEEE Transactions on Industrial Electronics*, vol. 45, no. 5, pp. 704-712, Oct. 1998.

[85] X. Mao, A. K. Jain, and R. Ayyanar, "Hybrid interleaved space vector PWM for ripple reduction in modular converters," *IEEE Transactions on Power Electronics*, vol. 26, no. 7, pp. 1954-1967, Jul. 2011.

[86] K. Shukla, V. Malyala, and R. Maheshwari, "A novel carrier-based hybrid PWM technique for minimization of line current ripple in two parallel interleaved two-level VSIs," *IEEE Transactions on Industrial Electronics*, vol. 65, no. 3, pp. 1908-1918, Mar. 2018.

[87] G. Lei, J. Zhu, and Y. Guo, *Multidisciplinary Design Optimization Methods for Electrical Machines and Drive Systems*, Berlin, Heidelberg: Springer Berlin / Heidelberg, 2016.

[88] F. Blaschke, "The principle of field orientation as applied to the new transvector closed-loop system for rotating-field machines," *Siemens Review*, Vol. 34, No. 3,

1972, pp. 217-220.

[89] Z. Tang and B. Akin, "A new LMS algorithm based deadtime compensation method for PMSM FOC drives," *IEEE Transactions on Industry Applications*, vol. 54, no. 6, pp. 6472-6484, Nov.-Dec. 2018.

[90] I. Takahashi and Y. Ohmori, "High-performance direct torque control of an induction motor," *IEEE Transactions on Industry Applications*, vol. 25, no. 2, pp. 257-264, Mar.-Apr. 1989.

[91] L. Zhong, M. F. Rahman, W. Y. Hu, and K. W. Lim, "Analysis of direct torque control in permanent magnet synchronous motor drives," *IEEE Transactions on Power Electronics*, vol. 12, no. 3, pp. 528-536, May 1997.

[92] P. D. C. Perera, F. Blaabjerg, J. K. Pedersen, and P. Thogersen, "A sensorless, stable V/f control method for permanent-magnet synchronous motor drives," *IEEE Transactions on Industry Applications*, vol. 39, no. 3, pp. 783-791, May-Jun. 2003.

[93] Z. Wang, Y. Zheng, Z. Zou and M. Cheng, "Position sensorless control of interleaved CSI fed PMSM drive with extended kalman filter," *IEEE Transactions on Magnetics*, vol. 48, no. 11, pp. 3688-3691, Nov. 2012.

[94] W. Xu, Y. Jiang, C. Mu and F. Blaabjerg, "Improved nonlinear flux observer-based second-order SOIFO for PMSM sensorless control," *IEEE Transactions on Power Electronics*, vol. 34, no. 1, pp. 565-579, Jan. 2019.

[95] V. I. Utkin, "Sliding mode control design principles and applications to electric drives," *IEEE Transactions on Industrial Electronics*, vol. 40, no. 1, pp. 23-36, Feb. 1993.

[96] J.P.S, R. Melício, V.M.F. Mendes, and J.P.S. Catalão, "Fractional-order control and simulation of wind energy systems with PMSG/full-power converter topology," *Energy Conversion and Management*, vol. 51, no. 6, pp. 1250-1258, Jun. 2010.

[97] X. Rui, W. Yin, Y. Dong, L. Lin, and Xin Wu, "Fractional-order sliding mode control for hybrid drive wind power generation system with disturbances in the grid," *Wind Energy*, vol. 22, no. 1, pp. 49-64, 2019.

[98] B. Yao and M. Tomizuka, "Adaptive robust control SISO nonlinear systems in a semi-strict feedback form," *Automatica*, vol. 33, no. 5, pp. 893-900, May 1997.

[99] B. Yao and M. Tomizuka, "Adaptive robust control MIMO nonlinear systems in a semi-strict feedback form," *Automatica*, vol. 37, no. 9, pp. 1305-1321, Sep. 2001.

[100] W. Yin, X. Wu, and X. Rui, "Adaptive robust backstepping control of the speed regulating differential mechanism for wind turbines," *IEEE Transactions on Sustainable Energy*, vol. 10, no. 3, pp. 1311-1318, Jul. 2019.

[101] X. Sun, M. Wu, G. Lei, Y. Guo, and J. Zhu, "An improved model predictive current control for PMSM drives based on current track circle," *IEEE Transactions on Industrial Electronics*, vol. 68, no. 5, pp. 3782-3793, May 2021.

[102] W. Huang, W. Hua, and Q. Fan, "Performance analysis and comparison of two fault-tolerant model predictive control methods for five-phase PMSM drives," *CES Transactions on Electrical Machines and Systems*, vol. 5, no. 4, pp. 311-320, Dec. 2021.

[103] G, Lei, J. Zhu, Y. Guo, C. Liu, and B. Ma., "Review of design optimization methods for electrical machines," *Energies*, vol. 10, no. 12, pp. 1962, Nov. 2017.

[104] G. Lei, C. Liu, Y. Guo, and J. Zhu, "Robust multidisciplinary design optimization of PM machines with soft magnetic composite cores for batch production," *IEEE Transactions on Magnetics*, vol. 52, no. 3, pp. 1-4, Mar. 2016.

[105] A. H. F. Dias and J. A. de Vasconcelos, "Multiobjective genetic algorithms applied to solve optimization problems," *IEEE Transactions on Magnetics*, vol. 38, no. 2, pp. 1133-1136, Mar. 2002.

[106] Z. Jin, X. Sun, Y. Cai, J. Zhu, G. Lei, and Y. Guo, "Comprehensive sensitivity and cross-factor variance analysis-based multi-objective design optimization of a 3-DOF hybrid magnetic bearing," *IEEE Transactions on Magnetics*, vol. 57, no. 2, pp. 1-4, Feb. 2021.

[107] J. Chu, H. Cheng, J. Sun, C. Peng, and Y. Hu, "Multi-objective optimization design of hybrid excitation double stator permanent magnet synchronous machine," *IEEE Transactions on Energy Conversion*, vol. 38, no. 4, pp. 2364-2375, Dec. 2023.

[108] A. H. F. Dias and J. A. de Vasconcelos, "Multiobjective genetic algorithms applied to solve optimization problems," *IEEE Transactions on Magnetics*, vol. 38, no. 2, pp. 1133-1136, Mar. 2002.

[109] G. Lei, T. Wang, J. Zhu, Y. Guo, and S. Wang, "System-level design optimization method for electrical drive systems—robust approach," *IEEE Transactions on Industrial Electronics*, vol. 62, no. 8, pp. 4702-4713, Aug. 2015.

[110] Y. Duan and D. M. Ionel, "A Review of recent developments in electrical machine design optimization methods with a permanent-magnet synchronous motor benchmark study," *IEEE Transactions on Industry Applications*, vol. 49, no. 3, pp. 1268-1275, May-Jun. 2013.

[111] P. Putek, P. Paplicki, and R. Pałka, "Low cogging torque design of permanent magnet machine using modified multi-level set method with total variation regularization," *IEEE Transactions on Magnetics*, vol. 50, no. 2, pp. 657-660, Feb. 2014.

[112] X. Sun, K. Diao, G. Lei, Y. Guo, and J. Zhu, "Direct torque control based on a fast modelling method for a segmented-rotor switched reluctance motor in HEV application," *IEEE Journal of Emerging and Selected Topics in Power Electronics*, vol. 9, no. 1, pp. 232-241, Feb. 2021.

[113] J. Chu, H. Cheng, J. Sun, C. Peng, and Y. Hu, "Multi-objective optimization design of hybrid excitation double stator permanent magnet synchronous machine," *IEEE Transactions on Energy Conversion*, vol. 38, no. 4, pp. 2364-2375, Dec. 2023.

[114] P. Putek, P. Paplicki, and R. Pałka, "Low cogging torque design of permanent magnet machine using modified multi-level set method with total variation regularization," *IEEE Transactions on Magnetics*, vol. 50, no. 2, pp. 657-660, Feb. 2014.

[115] P. Asef, R. B. Perpiñà, S. Moazami, and A. C. Lapthorn, "Rotor shape multi-level design optimization for double-stator permanent magnet synchronous motors," *IEEE Transactions on Energy Conversion*, vol. 34, no. 3, pp. 1223-1231, Sep. 2019.

[116] P. Asef, R. B. Perpiñà, M. R. Barzegaran, A. Lapthorn, and D. Mewes, "Multiobjective design optimization using dual-level response surface methodology and booth's algorithm for permanent magnet synchronous generators," *IEEE Transactions on Energy Conversion*, vol. 33, no. 2, pp. 652-659, Jun. 2018.

[117] L. Mo, Z. Gangxu, T. Zhang, L. Qing, and L. Baolian, "Multilevel optimization design for a flux-concentrating permanent-magnet brushless machine considering PM demagnetization limitation," *IEEE Transactions on Magnetics*, vol. 57, no. 2, pp. 1-5, Feb. 2021.

[118] G. Lei, C. Liu, J. Zhu, and Y. Guo, "Techniques for Multilevel Design Optimization of Permanent Magnet Motors," *IEEE Transactions on Energy Conversion*, vol. 30, no. 4, pp. 1574-1584, Dec. 2015.

[119] G. Lei, W. Xu, J. Hu, J. Zhu, Y. Guo, and K. Shao, "Multilevel design optimization of a fspmm drive system by using sequential subspace optimization method," *IEEE Transactions on Magnetics*, vol. 50, no. 2, pp. 685-688, Feb. 2014.

[120] G. Lei, G. Bramerdorfer, B. Ma, Y. Guo, and J. Zhu, "Robust design optimization of electrical machines: multi-objective approach," *IEEE Transactions on Energy Conversion*, vol. 36, no. 1, pp. 390-401, Mar. 2021.

[121] L. Lebensztajn, C. A. R. Marretto, M. C. Costa, and J.-L. Coulomb, "Kriging: a useful tool for electromagnetic device optimization," *IEEE Transactions on Magnetics*, vol. 40, no. 2, pp. 1196-1199, Mar. 2004.

[122] G. Lei, C. Liu, Y. Guo, and J. Zhu, "Multidisciplinary design analysis and optimization of a PM transverse flux machine with soft magnetic composite core," *IEEE Transactions on Magnetics*, vol. 51, no. 11, pp. 1-4, Nov. 2015.

[123] W. Wang, P. Zheng, M. Wang, Y. Liu, Z. Fu, and Y. Sui, "Demagnetization and permanent-magnet minimization analyses of less-rare-earth interior permanent-magnet synchronous machines used for electric vehicles," *IEEE Transactions on Magnetics*, vol. 54, no. 11, pp. 1-5, Nov. 2018.

[124] Y. Oda, H. Toda, N. Shiga, S. Kasai, and T. Hiratani, "Effect of Si content on iron loss of electrical steel sheet under compressive stress," *IEEE Transactions on Magnetics*, vol. 50, no. 4, pp. 1-4, Apr. 2014.

[125] G. Bertotti, A. Canova, M. Chiampi, D. Chiarabaglio, F. Fiorillo, and A. M. Rietto, "Core loss prediction combining physical models with numerical field analysis," *Journal of Magnetism and Magnetic Materials*, vol. 133, pp. 647–650, 1994.

[126] K. Yamazaki, Y. Fukushima, and M. Sato, "Loss analysis of permanent-magnet motors with concentrated windings-variation of magnet eddy-current loss due to stator and rotor shapes," *IEEE Transactions on Industry Applications*, vol. 45, no. 4, pp. 1334-1342, Jul.-Aug. 2009.

[127] F. Henrotte, S. Steentjes, K. Hameyer, and C. Geuzaine, "Iron loss calculation in steel laminations at high frequencies," *IEEE Transactions on Magnetics*, vol. 50, no. 2, pp. 333-336, Feb. 2014.

[128] O. Payza, Y. Demir, and M. Aydin, "Investigation of losses for a concentrated winding high-speed permanent magnet-assisted synchronous reluctance motor for washing machine application," *IEEE Transactions on Magnetics*, vol. 54, no. 11, pp. 1-5, Nov. 2018.

[129] X. Chen, J. Wang, B. Sen, P. Lazari, and T. Sun, "A high-fidelity and computationally efficient model for interior permanent-magnet machines considering the magnetic saturation, spatial harmonics, and iron loss effect," *IEEE Transactions on Industrial Electronics*, vol. 62, no. 7, pp. 4044-4055, Jul. 2015.

[130] B. Scheerlinck, H. De Gersem, and P. Sergeant, "Reducing losses due to fringing flux in an axial-flux permanent-magnet synchronous machine," *IEEE Transactions on Magnetics*, vol. 52, no. 10, pp. 1-8, Oct. 2016.

[131] A. Hemeida, A. Lehikoinen, P. Rasilo, H. Vansompel, A. Belahcen, A. Arkkio, and P. Sergeant, "A simple and efficient quasi-3D magnetic equivalent circuit for surface axial flux permanent magnet synchronous machines," *IEEE Transactions on Industrial Electronics*, vol. 66, no. 11, pp. 8318-8333, Nov. 2019.

[132] A. R. Tariq, C. E. Nino-Baron, and E. G. Strangas, "Iron and magnet losses and torque calculation of interior permanent magnet synchronous machines using magnetic equivalent circuit," *IEEE Transactions on Magnetics*, vol. 46, no. 12, pp. 4073-4080, Dec. 2010.

[133] H. W. Derbas, J. M. Williams, and S. D. Pekarek, "A comparison of nodal- and mesh-based magnetic equivalent circuit models," *IEEE Transactions on Energy Conversion*, vol. 24, no. 2, pp. 388-396, Jun. 2009.

[134] P. Liang, F. Chai, and Y. Wang, "Analytical prediction of no-load stator iron losses in spoke-type permanent-magnet synchronous machines," *IEEE Transactions on Energy Conversion*, vol. 33, no. 1, pp. 252-259, Mar. 2018.

[135] P. Liang, Y. Tang, F. Chai, K. Shen, and W. Liu, "Calculation of the iron losses in a spoke-type permanent magnet synchronous in-wheel motor for electric vehicles by utilizing the Bertotti model," *IEEE Transactions on Magnetics*, vol. 55, no. 7, pp. 1-7, Jul. 2019.

[136] Q. Li, T. Fan, and X. Wen, "Characterization of iron loss for integral-slot interior permanent magnet synchronous machine during flux weakening," *IEEE Transactions on Magnetics*, vol. 53, no. 5, pp. 1-8, May 2017.

[137] W. Q. Chu, Z. Zhu, X. Liu, D. A. Stone, and M. P. Foster, "Iron loss calculation

in permanent magnet machines under unconventional operations," *IEEE Transactions on Magnetics*, vol. 50, no. 11, pp. 1-4, Nov. 2014.

[138] Y. Miyama, M. Hazeyama, S. Hanioka, N. Watanabe, A. Daikoku, and M. Inoue, "PWM carrier harmonic iron loss reduction technique of permanent-magnet motors for electric vehicles," *IEEE Transactions on Industrial Electronics*, vol. 52, no. 4, pp. 2865-2871, Jul.-Aug. 2016.

[139] L. Yu, Z. Zhang, Z. Bian, D. Gerada, and C. Gerada, "Dual-pulse mode control of a high-speed doubly salient electromagnetic machine for loss reduction and speed range extension," *IEEE Transactions on Industrial Electronics*, vol. 67, no. 6, pp. 4391-4401, Jun. 2020.

[140] S. Zhu, J. Dong, Y. Li, and W. Hua, "Fast calculation of carrier harmonic iron losses caused by pulse width modulation in interior permanent magnet synchronous motors," *IET Electric Power Applications*, vol. 14, no. 7, pp. 1163-1176, May 2020.

[141] D. Miyagi, Y. Aoki, and N. Takahashi, "Effect of compressive stress in thickness direction on iron losses of non-oriented electrical steel sheet," *IEEE Transactions on Magnetics*, vol. 46, no. 6, pp. 2040-2043, Jun. 2010.

[142] S. Xue, J. Feng, S. Guo, J. Peng, and Z. Q. Zhu, "A new iron loss model for temperature dependencies of hysteresis and eddy current losses in electrical machines," *IEEE Transactions on Magnetics*, vol. 54, no. 1, pp. 1-10, Jan. 2018.

[143] C. Zhang, L. Chen, X. Wang, and R. Tang, "Loss calculation and thermal analysis for high-speed permanent magnet synchronous machines," *IEEE Access*, vol. 8, pp. 92627-92636, May 2020.

[144] D. Zhang, T. Liu, H. Zhao, and T. Wu, "An analytical iron loss calculation model of inverter-fed induction motors considering supply and slot harmonics," *IEEE Transactions on Industrial Electronics*, vol. 66, no. 12, pp. 9194-9204, Dec. 2019.

[145] J. Lavers, P. Biringer, and H. Hollitscher, "Estimation of core losses when the flux waveform contains the fundamental plus a single odd harmonic component," *IEEE Transactions on Magnetics*, vol. 13, no. 5, pp. 1128-1130, Sep. 1977.

[146] W. Roshen, "Iron loss model for permanent-magnet synchronous motors," *IEEE Transactions on Magnetics*, vol. 43, no. 8, pp. 3428-3434, Aug. 2007.

[147] F.G., Baily, "The hysteresis of iron and steel in a rotating magnetic field," *Philosophical Transactions of the Royal Society*, vol. 187, no. 1896, pp. 715-746, Jan. 1896.

[148] J. Sievert, "Recent advances in the one- and two-dimensional magnetic measurement technique for electrical sheet steel," *IEEE Transactions on Magnetics*, vol. 26, no. 5, pp. 2553-2558, Sep. 1990.

[149] Y. Guo, J. G. Zhu, J. Zhong, H. Lu, and J. X. Jin, "Measurement and modelling of rotational core losses of soft magnetic materials used in electrical machines: a review," *IEEE Transactions on Magnetics*, vol. 44, no. 2, pp. 279-291, Feb. 2008.

[150] J. Sievert, “Two-dimensional magnetic measurements - history and achievements of the workshop,” *Przeglad Elektrotechniczny*, vol. 87, pp. 2-10, Jan. 2011.

[151] W. Brix, K. Hempel, and W. Schroeder, “Method for the measurement of rotational power loss and related properties in electrical steel sheets,” *IEEE Transactions on Magnetics*, vol. 18, no. 6, pp. 1469-1471, Nov. 1982.

[152] J. G. Zhu and V. S. Ramsden, “Two dimensional measurement of magnetic field and core loss using a square specimen tester,” *IEEE Transactions on Magnetics*, vol. 29, no. 6, pp. 2995-2997, Nov. 1993.

[153] J. J. Zhong and J. G. Zhu, “Electromagnetic design of a 3D tester for magnetic properties of soft magnetic materials,” *ICEMS'2001. Proceedings of the Fifth International Conference on Electrical Machines and Systems (IEEE Cat. No.01EX501)*, Shenyang, China, 2001, pp. 392-395.

[154] Q. Yang, Y. Li, Z. Zhao, L. Zhu, Y. Luo, and J. Zhu, “Design of a 3-D rotational magnetic properties measurement structure for soft magnetic materials,” *IEEE Transactions on Applied Superconductivity*, vol. 24, no. 3, pp. 1-4, Jun. 2014.

[155] J. Li, Q. Yang, Y. Li, C. Zhang. and B. Qu, “Measurement and modelling of 3-D rotating anomalous loss considering harmonics and skin effect of soft magnetic materials,” *IEEE Transactions on Magnetics*, vol. 53, no. 6, pp. 1-4, Jun. 2017.

[156] Y. Li, Q. Yang, J. Zhu, and Y. Guo, “Magnetic properties measurement of soft magnetic composite materials over wide range of excitation frequency,” *IEEE Transactions on Industry Applications*, vol. 48, no. 1, pp. 88-97, Jan.-Feb. 2012.

[157] J. G. Zhu, J. J. Zhong, Z. W. Lin, and J. D. Sievert, “Measurement of magnetic properties under 3-D magnetic excitations,” *IEEE Transactions on Magnetics*, vol. 39, no. 5, pp. 3429-3431, Sep. 2003.

[158] Y. Li, Q. Yang, Y. Liu, Z. Zhao, C. Zhang, and D. Li, “A novel combined $B-H$ sensing coil in three-dimensional magnetic properties testing system,” *IEEE Transactions on Applied Superconductivity*, vol. 24, no. 3, pp. 1-4, Jun. 2014.

[159] C. Michelakis, D. Samaras, and G. Litsardakis, “A 3-D moving vectorial Preisach-type hysteresis model,” *Journal of Magnetism and Magnetic Materials*, vol. 207, no. 1-3, pp. 188-192, Dec. 1999.

[160] J. J. Zhong, J. G. Zhu, Y. Guo, and Z. W. Lin, “A 3-D vector magnetization model with interaction field,” *IEEE Transactions on Magnetics*, vol. 41, no. 5, pp. 1496-1499, May 2005.

[161] E. Cardelli, E. Della Torre, and A. Faba, “A general vector hysteresis operator: extension to the 3-D case,” *IEEE Transactions on Magnetics*, vol. 46, no. 12, pp. 3990-4000, Dec. 2010.

[162] D. Li, Z. Qiao, Y. Wu, Z. Li, Y. Song, and Y. Li, “Three-Dimensional Magnetic Hysteresis Modelling Based on Vector Hysteresis Operator,” *IEEE Access*, vol. 9, pp. 144624-144633, 2021.

[163] Y. Guo, J. Zhu, Z. Lin, J, Zhong, H. Lu, and S. Wang, "Determination of 3D magnetic reluctivity tensor of soft magnetic composite material," *Journal of Magnetism and Magnetic Materials*, vol. 312, no. 2, pp. 458-463, May 2007.

[164] Y. Li, Q. Yang, J. Zhu, Z. Lin, Y. Guo, and J. Sun, "Research of three-dimensional magnetic reluctivity tensor based on measurement of magnetic properties," *IEEE Transactions on Applied Superconductivity*, vol. 20, no. 3, pp. 1932-1935, Jun. 2010.

[165] J. Sun, Q. Yang, Y. Wang, W. Yan, and Y. Li, "A finite element formulation for tetrahedral elements based on reluctivity tensor," *IEEE Transactions on Applied Superconductivity*, vol. 20, no. 3, pp. 1852-1855, Jun. 2010.

[166] H. Qamar, H. Qamar, and R. Ayyanar, "Performance analysis and experimental validation of 240°-clamped space vector PWM to minimize common mode voltage and leakage current in EV/HEV traction drives," *IEEE Transactions on Transportation Electrification*, vol. 8, no. 1, pp. 196-208, Mar. 2022.

[167] D. G. Holmes and T. A. Lipo. *Pulse Width Modulation for Power Converters: Principles and Practice*. USA: Wiley & Sons, 2003.

[168] T. Y. Wang, F. Q. Wen, and F. G. Zhang, "Analysis of multi-field coupling strength for MW high-speed permanent magnet machine," *Transactions of China Electrotechnical Society*, vol. 33, no. 19, pp. 4508–4516, Oct. 2018.

[169] S. Zhu, J. Dong, Y. Li, and W. Hua, "Fast calculation of carrier harmonic iron losses caused by pulse width modulation in interior permanent magnet synchronous motors," *IET Electric Power Applications*, vol. 14, no. 7, pp. 1163-1176, May 2020.

[170] T. Sun, J. Wang, C. Jia, and L. Peng, "Integration of FOC with DFVC for interior permanent magnet synchronous machine drives," *IEEE Access*, vol. 8, pp. 97935-97945, May 2020.

[171] Y. Guo, J. Zhu, H. Lu, Z. Lin, and Y. Li, "Core loss calculation for soft magnetic composite electrical machines," *IEEE Transactions on Magnetics*, vol. 48, no. 11, pp. 3112-3115, Nov. 2012.

[172] K. Diao, X. Sun, *et al*., "System-level robust design optimization of a switched reluctance motor drive system considering multiple driving cycles," *IEEE Transactions on Energy Conversion*, vol. 36, no. 1, pp. 348-357, 2021.

[173] G. Lei, J. Zhu, and Y. Guo, *Multidisciplinary Design Optimization Methods for Electrical Machines and Drive Systems*, Berlin, Heidelberg: Springer Berlin / Heidelberg, 2016.

[174] Z. Tang and B. Akin, "A new LMS algorithm based deadtime compensation method for PMSM FOC drives," *IEEE Transactions on Industry Applications*, vol. 54, no. 6, pp. 6472-6484, Nov.-Dec. 2018.

[175] Z. Li, W. Han, Z. Xin, Q. Liu, J. Chen, and P. C. Loh, "A review of magnetic core materials, core loss modeling and measurements in high-power high-frequency transformers," *CPSS Transactions on Power Electronics and Applications*, vol. 7, no.

4, pp. 359-373, Dec. 2022.

[176] X. Chen, J. Wang, and B. Sen, "A high-fidelity and computationally efficient model for interior permanent-magnet machines considering the magnetic saturation, spatial harmonics, and iron loss effect," *IEEE Transactions on Industrial Electronics*, vol. 62, no. 7, pp. 4044-4055, Jul. 2015.

[177] G. Lei, W. Xu, and J. Hu, *et al*., "Multi-level design optimization of a FSPMM drive system by using sequential subspace optimization method," *IEEE Transactions on Magnetics*, vol. 50, no. 2, pp. 685-688, Feb. 2014.

[178] I. Suehiro, T. Mifune, and T. Matsuo, *et al*., "Ladder circuit modelling of dynamic hysteretic property representing excess eddy-current loss," *IEEE Transactions on Magnetics*, vol. 54, no. 3, pp. 1-4, Mar. 2018.

[179] A. Hemeida, A. Lehikoinen, and P. Rasilo, *et al*., "A simple and efficient quasi-3D magnetic equivalent circuit for surface axial flux permanent magnet synchronous machines," *IEEE Transactions on Industrial Electronics*, vol. 66, no. 11, pp. 8318-8333, Nov. 2019.

[180] A. R. Tariq, C. E. Nino-Baron, and E. G. Strangas, "Iron and magnet losses and torque calculation of interior permanent magnet synchronous machines using magnetic equivalent circuit," *IEEE Transactions on Magnetics*, vol. 46, no. 12, pp. 4073-4080, Dec. 2010.

[181] S. K. Kommuri, Y. Park, and S. B. Lee, "Online compensation of mechanical load defects with composite control in PMSM drives," *IEEE/ASME Transactions on Mechatronics*, vol. 26, no. 3, pp. 1392–1400, Jun. 2021.

[182] D. Hu, W. Xu, and R. Dian, *et al*., "Loss minimization control of linear induction motor drive for linear metros," *IEEE Transactions on Industrial Electronics*, vol. 65, no. 9, pp. 6870-6880, Sep. 2018.

[183] S. Ito, T. Mifune, and T. Matsuo, *et al*., "Equivalent circuit modelling of DC and AC ferrite magnetic properties using H-input and B-input play models," *IEEE Transactions on Magnetics*, vol. 49, no. 5, pp. 1985-1988, May 2013.

[184] Z. Qian, T. Huang, and W. Wang, *et al*., "Torque ripple reduction of PMSM based on modified DBN-DNN surrogate model," *IEEE Transactions on Transportation Electrification*, vol. 9, no. 2, pp. 2820-2829, Jun. 2023.

[185] C. Xia, J. Zhao, *et al*., "A novel direct torque control of matrix converter-fed PMSM drives using duty cycle control for torque ripple reduction," *IEEE Transactions on Industrial Electronics*, vol. 61, no. 6, pp. 2700-2713, Jun. 2014.

[186] M. Peña, M. Meyer, *et al*., "Model predictive direct self-control for six-step operation of permanent-magnet synchronous machines," *IEEE Transactions on Power Electronics*, vol. 38, no. 10, pp. 12416-12429, Oct. 2023.

[187] T. Sun, J. Wang and X. Chen, "Maximum torque per ampere (MTPA) control for interior permanent magnet synchronous machine drives based on virtual signal

injection," *IEEE Transactions on Power Electronics*, vol. 30, no. 9, pp. 5036-5045, Sept. 2015.

[188] C. Cavallaro, A. O. Di Tommaso, R. Miceli, A. Raciti, G. R. Galluzzo and M. Trapanese, "Efficiency enhancement of permanent-magnet synchronous motor drives by online loss minimization approaches," *IEEE Transactions on Industrial Electronics*, vol. 52, no. 4, pp. 1153-1160, Aug. 2005.

[189] S. Kim, Y. -D. Yoon, S. -K. Sul, and K. Ide, "Maximum torque per ampere (MTPA) control of an IPM machine based on signal injection considering inductance saturation," *IEEE Transactions on Power Electronics*, vol. 28, no. 1, pp. 488-497, Jan. 2013.

[190] R. Ni, D. Xu, and G. Wang, *et al*., "Maximum efficiency per ampere control of permanent-magnet synchronous machines," *IEEE Transactions on Industrial Electronics*, vol. 62, no. 4, pp. 2135–2143, Apr. 2015.

[191] L. Liu, X. Ba, Y. Guo, G. Lei, X. Sun and J. Zhu, "Improved iron loss prediction models for interior PMSMs considering coupling effects of multiphysics factors," *IEEE Transactions on Transportation Electrification*, vol. 9, no. 1, pp. 416-427, Mar. 2023.

[192] Ji-Young Lee, Sang-Ho Lee, Geun-Ho Lee, Jung-Pyo Hong, and Jin Hur, "Determination of parameters considering magnetic nonlinearity in an interior permanent magnet synchronous motor," *IEEE Transactions on Magnetics*, vol. 42, no. 4, pp. 1303-1306, Apr. 2006.

[193] X. Ba, Y. Guo, J. Zhu, and C. Zhang, "An equivalent circuit model for predicting the core loss in a claw-pole permanent magnet motor with soft magnetic composite core," *IEEE Transactions on Magnetics*, vol. 54, no. 11, pp. 1-6, Nov. 2018.

[194] D. Hu, W. Xu, and R. Dian, *et al*., "Loss minimization control of linear induction motor drive for linear metros," *IEEE Transactions on Industrial Electronics*, vol. 65, no. 9, pp. 6870-6880, Sep. 2018.

[195] G. Lei, J. Zhu, and Y. Guo, *Multidisciplinary design optimization methods for electrical machines and drive systems*, Berlin, Heidelberg: Springer Berlin / Heidelberg, 2016.

[196] X. Sun, Z. Shi, *et al*., "Driving cycle oriented design optimization of a permanent magnet hub motor drive system for a four-wheel-drive electric vehicle," *IEEE Transactions on Transportation Electrification*, vol. 6, no. 3, pp. 1115-1125, 2020.

[197] V. Ghorbanian and D. A. Lowther, "Magnetic and electrical design challenges of inverter-fed permanent magnet synchronous motors," *IEEE Transactions on Magnetics*, vol. 53, no. 6, pp. 1-4, Jun. 2017.

[198] M. E. Beniakar, A. G. Sarigiannidis, and P. E. Kakosimos *et al*., "Multi-objective evolutionary optimization of a surface mounted PM actuator with fractional slot winding for aerospace applications," *IEEE Transactions on Magnetics*, vol. 50, no. 2, pp. 665-668, Feb. 2014.

[199] D. K. Lim, D. K. Woo, and H. K. Yeo, *et al*., "A novel surrogate-assisted multi-objective optimization algorithm for an electromagnetic machine design," *IEEE Transactions on Magnetics*, vol. 51, no. 3, pp. 1-4, Mar. 2015.

[200] Y. Hua, H. Zhu, *et al*., "Multi-objective optimization design of permanent magnet assisted bearingless synchronous reluctance motor using NSGA-II," *IEEE Transactions on Industrial Electronics*, vol. 68, no. 11, pp. 10477-10487, 2021.

[201] J. Zhang, H. Wang, *et al*., "Multi-objective optimal design of bearingless switched reluctance motor based on multi-objective genetic particle swarm optimizer," *IEEE Transactions on Magnetics*, vol. 54, no. 1, pp. 1-13, Jan. 2018.

[202] G. Crevecoeur, L. Dupre, and R. Van de Walle, "Space mapping optimization of the magnetic circuit of electrical machines including local material degradation," *IEEE Transactions on Magnetics*, vol. 43, no. 6, pp. 2609-2611, Jun. 2007.

[203] J. Gong, F. Gillon, and J. T. Canh, *et al*., "Proposal of a Kriging output space mapping technique for electromagnetic design optimization," *IEEE Transactions on Magnetics*, vol. 53, no. 6, pp. 1-4, Jun. 2017.

[204] L. Lebensztajn, C. A. R. Marretto, and M. C. Costa, *et al*., "Kriging: a useful tool for electromagnetic device optimization," *IEEE Transactions on Magnetics*, vol. 40, no. 2, pp. 1196-1199, Mar. 2004.

[205] D. K. Lim, S. Y. Jung, and K. -P. Yi, *et al*., "A novel sequential-stage optimization strategy for an interior permanent magnet synchronous generator design," *IEEE Transactions on Industrial Electronics*, vol. 65, no. 2, pp. 1781-1790, Feb. 2018.

[206] G. Lei, C. Liu, and J. Zhu, *et al*., "Techniques for multilevel design optimization of permanent magnet motors," *IEEE Transactions on Energy Conversion*, vol. 30, no. 4, pp. 1574-1584, Dec. 2015.

[207] G. Lei, W. Xu, and J. Hu, *et al*., "Multilevel design optimization of a FSPMM drive system by using sequential subspace optimization method," *IEEE Transactions on Magnetics*, vol. 50, no. 2, pp. 685-688, Feb. 2014.

[208] G. Lei, C. Liu, and M. Jafari, *et al*., "Multilevel robust design optimization of a superconducting magnetic energy storage based on a benchmark study," *IEEE Transactions on Applied Superconductivity*, vol. 26, no. 7, pp. 1-5, Oct. 2016.

[209] K. Diao, X. Sun, *et al*., "System-level robust design optimization of a switched reluctance motor drive system considering multiple driving cycles," *IEEE Transactions on Energy Conversion*, vol. 36, no. 1, pp. 348-357, 2021.

[210] B. Ma, G. Lei, C. Liu, J. Zhu and Y. Guo, "Robust tolerance design optimization of a PM claw pole motor with soft magnetic composite cores," *IEEE Transactions on Magnetics*, vol. 54, no. 3, pp. 1-4, Mar. 2018.